



저작자표시-비영리-변경금지 2.0 대한민국

이용자는 아래의 조건을 따르는 경우에 한하여 자유롭게

- 이 저작물을 복제, 배포, 전송, 전시, 공연 및 방송할 수 있습니다.

다음과 같은 조건을 따라야 합니다:



저작자표시. 귀하는 원저작자를 표시하여야 합니다.



비영리. 귀하는 이 저작물을 영리 목적으로 이용할 수 없습니다.



변경금지. 귀하는 이 저작물을 개작, 변형 또는 가공할 수 없습니다.

- 귀하는, 이 저작물의 재이용이나 배포의 경우, 이 저작물에 적용된 이용허락조건을 명확하게 나타내어야 합니다.
- 저작권자로부터 별도의 허가를 받으면 이러한 조건들은 적용되지 않습니다.

저작권법에 따른 이용자의 권리는 위의 내용에 의하여 영향을 받지 않습니다.

이것은 [이용허락규약\(Legal Code\)](#)을 이해하기 쉽게 요약한 것입니다.

[Disclaimer](#)

A DOCTORAL DISSERTATION

**Development of the DC-RF Hybrid Plasma
Source and the Application to the Etching and
Texturing of the Silicon Surface**

**Department of Nuclear & Energy Engineering
Graduate School**

Jeju National University

Ji Hun Kim

February, 2011

Ph. D. DISSERTATION

**Development of the DC-RF Hybrid Plasma
Source and the Application to the Etching and
Texturing of the Silicon Surface**

Department of Nuclear & Energy Engineering
Graduate School
Jeju National University

Ji Hun Kim

February, 2011

博士學位論文

직류-고주파 복합 플라즈마 소스
개발 및 이를 응용한 실리콘 표면
식각 및 Texturing 연구

濟州大學校 大學院

에너지공학과

金 志 勳

2011 年 02 月

직류-고주파 복합 플라즈마 소스 개발 및 이를 응용한 실리콘 표면 식각 및 Texturing 연구

指導教授 李 憲 周

金 志 勳

이 論文을 工學博士學位論文으로 提出함

2010年 12月

金志勳의 工學 博士學位 論文을 認准함

審査委員長	최 치 규	(인)
委 員	노 승 정	(인)
委 員	유 석 재	(인)
委 員	이 윤 준	(인)
委 員	이 현 주	(인)

濟州大學校 大學院

2010年 12月

Development of the DC-RF Hybrid Plasma Source and the Application to the Etching and Texturing of the Silicon Surface

Ji-Hun Kim

(Supervised by professor Heon-Ju Lee)

A thesis submitted in partial fulfillment of the requirement for the degree
of Doctor of Nuclear and Energy Engineering.

2010. 12.

This thesis has been examined and approved.

Thesis director, Heon Ju Lee, Prof. of Nuclear & Energy Engineering

Chi Kyu Choi

Seung Jeong Noh

Suk Jae Yoo

Yun Jun Lee

Heon Ju Lee

(Name and signature)

2010. 12

Date

Department of Nuclear & Energy Engineering

GRADUATE SCHOOL

JEJU NATIONAL UNIVERSITY

CONTENTS

CONTENTS	i
LIST OF FIGURES	v
LIST OF TABLES	xi
SUMMARY	xii
I. Introduction	1
1. Atmospheric Pressure source	1
1.1 DC arc plasmatoms with hot rod cathode and cold nozzle anode	2
1.2 DC arc plasmatoms with cold thermo-chemical cathode (Hf, Zr) and cold nozzle anode	2
1.3 DC arc plasmatoms with cold tubular electrodes and arc revolving inside	3
1.4 AC three-phase arc plasmatoms	3
1.5 RF arc plasmatoms	4
1.6 Microwave Plasmatoms	4
1.7 Dielectric barrier discharge (DBD) plasma	4
2. Plasma etching	8
3. Plasma texturing for the solar cell	9
II. Theoretical Background	11
1. Atmospheric pressure plasma source	11
1.1 DC arc plasma source	11
1.2 ICP torches	13
1.3 Dielectric barrier discharge (DBD)	15

2. Plasma etching	17
2.1 Etching rate, uniformity and area	18
2.2 Isotropic etching and an-isotropic etching	19
2.3 Parameters of the etching condition	20
3. Plasma texturing for the solar cell	22
3.1 Silicon texturing processing in the solar cell	23
3.2 Features of the plasma texturing processing	23
3.3 Advantage of the plasma texturing	23
III. Development of DC Arc Plasmatron	26
1. Development of new DC arc plasma source	26
1.1 The origin of technical decision	26
1.2 Main features of the plasmatron design	26
1.3 Problem of the cathode	31
1.4 Measurement of characteristics	31
1) Evaluation of plasma temperature	31
2) Measurements of the anode erosion rate	32
3) Plasma temperature and density	33
2. Plasmatron arc sport	35
2.1 Cathode arc spot	35
2.2 Main features of the plasmatron design	35
3. Plasmatron characteristics	36
3.1 Current/voltage ripple for inverter power source	36
3.2 Experimental VACs for the DC arc discharge in the plasmatron	38
1) Variation of inter-electrode distance	38
2) Variation of the anode orifice diameter	40

3) Variation of the argon flow rate in the cathode channel	40
4) Variation of gas flow rate in the Technologic channel	43
3.3 Stability of arc working points for the new plasmatron	45
4. Discussion	45
IV. Development of the DC-RF Hybrid Plasma Source	47
1. DC-RF hybrid plasma system	48
1.1 Calculation of and electric fields	48
1.2 RF impedance matching	52
1.3 DC-RF hybrid plasma system	58
2. Characteristics of the DC-RF hybrid plasma	60
2.1 Measurement of the discharge characteristics by IR camera	61
2.2 Measurement of the plasma parameter by a Langmuir probe	64
1) Parts of the I-V curve	65
2) Electron temperature	66
3) Electron density	66
4) Experimental set-up	67
5) Measurements and results	68
2.3 Measurement of the optical emission spectroscopy	76
2.4 Measurement of the plasma gas temperature by IR camera	81
V. Plasma Etching	84
1. Plasma etching by DC arc plasmatron at a low pressure	86
1.1 Experimental set-up	86
1.2 Results & discussion	88
2. Plasma etching by DC arc plasmatron at an atmospheric pressure	97

2.1 Experimental set-up	97
2.2 Results & discussion	99
3. Plasma etching by DC-RF hybrid system	103
3.1 Experimental set-up	103
3.2 Results & discussion	104
VI. Plasma Texturing for the Solar Cell	105
1. Experimental set-up	107
1.1 Plasma textuing at a low pressure (5 Torr)	109
1.2 Plasma textuing at an atmospheric pressure	109
2. Results and discussion	112
2.1 Results	112
2.2 Discussion	121
VII. Conclusion	122
REFERENCE	124
ABSTRACT (Korean)	128
CURRICULUM VITA	131
ACKNOWLEDGEMENT	135

LIST OF FIGURE

Fig. 1 Principle of dielectric barrier discharge	5
Fig. 2 Principle of arc plasma torches(left: current-carrying arc, right: transferred arc) · 12	12
Fig. 3 High velocity Plazjet (Tafa, Praxair)	12
Fig. 4 Sultzter Metco Triplex II Plasma Spray Gun	13
Fig. 5 RF plasma torch(Teckna Plasma system Inc).	14
Fig. 6 Concept of the dielectric barrier discharge	15
Fig. 7 Isotropic Etching and An-isotropic Etching	19
Fig. 8 Efficiency and loss factor in solar cell	22
Fig. 9 Basic concept of the silicon texturing for the solar cell	25
Fig. 10 Textured Silicon Surface (wet process)	25
Fig. 11 Concept of the DC arc lasmatron (1- cathode, 2- anode, 3- technologic channel, 4- process gas supply, 5- Ar supply, 6- Ar injector, 7 - plasma flow, 8- presumable form of plasma vortex acting as a distributed anode spot, 9 - arc discharge column.)	28
Fig. 12 Diagram of the T-plasmatron (front view)	28
Fig. 13 Top view of the DC arc plasmatron	29
Fig. 14 Design of A-type DC arc plasmatron	29
Fig. 15 Inside structure of A-type DC arc plasmatron	30
Fig. 16 Photo of the used copper anode	33
Fig. 17 Current waveform of the DC arc plasmatron	37
Fig. 18 Voltage waveform of the DC arc plasmatron	37
Fig. 19 VACs for $L_{AC} = 2$ and 4 mm	39

Fig. 20 VACs for anode = 1.5, 2.3 and 3.5 mm	40
Fig. 21 VACs for different argon flow rates in the cathode channel	42
Fig. 22 VACs for different gas flow rates in the technologic channel	44
Fig. 23 Calculated electric fields according to the number of turns	51
Fig. 24 Distribution of electric fields	52
Fig. 25 Source impedance driving its complex conjugate and the resulting equivalent ..	53
Fig. 26 Schematic of a DC-RF hybrid plasma and a gas injection system ·	54
Fig. 27 Electric current of the RF matching circuit (C_T : 738.7 pF, C_R : 42.0 pF) ···	55
Fig. 28 Electric current of the RF matching circuit (C_T : 738.7 pF, C_R : 42.30 pF)55	
Fig. 29 Electric current of the RF matching circuit according to the reduced capacitance	56
Fig. 30 Picture of the variable capacitor	56
Fig. 31 Picture of the matching part	57
Fig. 32 Schematic of the experimental apparatus of DC-RF hybrid plasma	59
Fig. 33 Schematic of a DC-RF hybrid plasma and a gas injection system ·	59
Fig. 34 Photographs of the RF and DC-RF hybrid plasma discharge	61
Fig. 35 Characteristics of the RF plasma discharge according to the pressure ·	62
Fig. 36 Characteristics of the DC-RF plasma discharge according to the pressure	63
Fig. 37 Typical electrical circuit for single Langmuir probe	64
Fig. 38 An idealized I-V curve. The left curve is expanded 10X to show the ion current	65
Fig. 39 DC power supply for electric probe	66
Fig. 40 Installed electric probe in the reaction chamber	67
Fig. 41 Measurement points of the electric probe	68
Fig. 42 Electron temperature distribution (vertical axis) of the DC-RF hybrid	

plasma at $x=0$	69
Fig. 43 Electron temperature distribution (vertical axis) of the DC-RF hybrid plasma at $x=2$	69
Fig. 44 Electron temperature distribution (vertical axis) of the DC-RF hybrid plasma at $x=4$	70
Fig. 45 Electron temperature distribution (horizontal axis) of the DC-RF hybrid plasma at $y=1.5$	70
Fig. 46 Electron temperature distribution (horizontal axis) of the DC-RF hybrid plasma at $y=0$	71
Fig. 47 Electron temperature distribution (horizontal axis) of the DC-RF hybrid plasma at $y=-1.5$	71
Fig. 48 Plasma density distribution (horizontal axis) of the DC-RF hybrid plasma at $y=0$	72
Fig. 49 Plasma density distribution (horizontal axis) of the DC-RF hybrid plasma at $y=1.5$	73
Fig. 50 Plasma density distribution (horizontal axis) of the DC-RF hybrid plasma at $y= -1.5$	73
Fig. 51 Plasma density distribution (vertical axis) of the DC-RF hybrid plasma at $x=0$	74
Fig. 52 Plasma density distribution (vertical axis) of the DC-RF hybrid plasma at $x=2$	74
Fig. 53 Plasma density distribution (vertical axis) of the DC-RF hybrid plasma at $x=-2$	75
Fig. 54 Argon plasma spectrum	78
Fig. 55 Optical emission spectrum of argon RF plasma	79
Fig. 56 Optical emission spectrum of argon DC-RF hybrid plasma	80

Fig. 57 IR camera measurement of DC-RF plasma (RF: 1 kW)	82
Fig. 58 IR camera measurement of DC-RF plasma (RF: 1 kW, DC: 1 kW)	82
Fig. 59 Plasma etching and texturing system (low pressure)	87
Fig. 60 SEM images (Ar: 2,000 sccm, O ₂ : 300 sccm, CF ₄ : 50 sccm, Voltage: 15V, Current: 100 A, P: 5 Torr)	89
Fig. 61 SEM images (Ar: 2,000 sccm, O ₂ : 200 sccm, CF ₄ : 50 sccm, V: 15V, Current: 100 A, P: 5 Torr)	89
Fig. 62 SEM images (Ar: 2,000 sccm, O ₂ : 100 sccm, CF ₄ : 50 sccm, V: 15V, Current: 100 A, P: 5 Torr)	90
Fig. 63 SEM images (Ar: 2,000 sccm, O ₂ : 300 sccm, CF ₄ : 30 sccm, V: 15V, Current: 100 A, P: 5 Torr)	90
Fig. 64 SEM images (Ar: 2,000 sccm, O ₂ : 200 sccm, CF ₄ : 30 sccm, V: 15V, Current: 100 A, P: 5 Torr)	91
Fig. 65 SEM images (Ar: 2,000 sccm, O ₂ : 100 sccm, CF ₄ : 30 sccm, V: 15V, Current: 100 A, P: 5 Torr)	91
Fig. 66 SEM images (Ar: 2,000 sccm, O ₂ : 300 sccm, CF ₄ : 50 sccm, V: 15V, Current: 50 A, P: 5 Torr)	92
Fig. 67 SEM images (Ar: 2,000 sccm, O ₂ : 200 sccm, CF ₄ : 50 sccm, V: 15V, Current: 50 A, P: 5 Torr)	92
Fig. 68 SEM images (Ar: 2,000 sccm, O ₂ : 300 sccm, CF ₄ : 30 sccm, V: 15V, Current: 50 A, P: 5 Torr)	93
Fig. 69 SEM images (Ar: 2,000 sccm, O ₂ : 200 sccm, CF ₄ : 30 sccm, V: 15V, Current: 50 A, P: 5 Torr)	93
Fig. 70 Distribution of the Etching rates; (a) Ar: 2,000 sccm, O ₂ : 300 sccm, CF ₄ : 50 sccm, Current: 100 A: (b) Ar: 2,000 sccm, O ₂ : 100 sccm, CF ₄ : 50 sccm, Current: 100 A: (c) Ar: 2,000 sccm, O ₂ : 300 sccm, CF ₄ : 50 sccm, Current: 100 A	94

Fig. 71 Results of the etching rates according to the oxygen flow rates	95
Fig. 72 Results of the etching rates according to the CF ₄ flow rates	95
Fig. 73 Results of the etching rates according to the DC arc plasmatron current	96
Fig. 74 Plasma etching and texturing system (atmospheric pressure)	98
Fig. 75 A SEM image of atmospheric pressure etching (Ar: 2,000 sccm, SF ₆ : 100 sccm, O ₂ : 200 sccm, D: 5 mm, Current: 70A)	100
Fig. 76 A SEM image of atmospheric pressure etching (Ar: 2,000 sccm, SF ₆ : 70 sccm, O ₂ : 200 sccm, D: 5 mm, Current: 70A)	100
Fig. 77 A SEM image of atmospheric pressure etching (Ar: 2,000 sccm, SF ₆ : 50 sccm, O ₂ : 200 sccm, D: 5 mm, Current: 70A)	101
Fig. 78 A SEM image of atmospheric pressure etching (Ar: 2,000 sccm, SF ₆ : 100 sccm, O ₂ : 200 sccm, D: 10 mm, Current: 70A)	101
Fig. 79 A SEM image of atmospheric pressure etching (Ar: 2,000 sccm, SF ₆ : 50 sccm, O ₂ : 200 sccm, D: 10 mm, Current: 70A)	102
Fig. 80 A SEM image of atmospheric pressure etching (Ar: 2,000 sccm, SF ₆ : 100 sccm, O ₂ : 200 sccm, D: 15 mm, Current: 70A)	102
Fig. 81 DC-RF hybrid plasma experimental set-up	103
Fig. 82 A SEM image by the DC-RF hybrid plasma	104
Fig. 83 A SEM image by the RF plasma	104
Fig. 84 A schematic diagram of the A-type plasmatron: (1) cathode, (2) anode, (3) argon supply, (4) technologic channel; (5, 6) technologic gas supply, (7) resulting plasma flow	108
Fig. 85 A diagram of the DC arc plasmatron processing system: (a) low pressure, (b) atmospheric pressure	110
Fig. 86 A picture of the DC arc plasmatron operation at low pressure (3-5mbar)	111
Fig. 87 Images of the DC arc plasmatron operating at atmospheric pressure	105

Fig. 88 SEM image of the single crystalline silicon surface textured at low pressure (3-5mbar, V=14V, D=72mm, CF4=100 sccm, Ar=2,000 sccm, O2=500sccm, V=14V, D=72mm, CF4=100 sccm, Ar=2,000 sccm, O2=500 sccm): (a) I=100 A, (b) I=70 A, (c) 50 A 113

Fig. 89 SEM image of the single crystalline silicon surface textured with a DC arc plasmatron current (Ar: 3000 sccm, SF₆:100 sccm, O₂:500 sccm, Pressure: 760torr): (a) 70A, (b) 100A 114

Fig. 90 SEM image of the mc-silicon surface textured at different processing times (Ar : 3000 sccm, SF₆:100sccm, O₂: 500sccm, Current: 100A, Pressure: 760torr): (a) 10 sec. (b) 30 sec. (c) 60 sec. 115

Fig. 91 SEM image of the single crystalline silicon surface textured with a oxygen concentrations (Ar : 3000 sccm, SF₆: 100 sccm, Current: 100A, Pressue: 760torr): (a) 5%, (b) 10%, (c) 15% 116

Fig. 92 SEM image of the textured amorphous silicon surface: (a) Bare silicon, (b) textured silicon by DC arc plasmatron (Ar: 3000 sccm, SF₆: 100 sccm, O₂: 500 sccm, Current: 100A, Pressue: 760 torr) 117

Fig. 93 SEM image of the pyramid angle to compare low and atmospheric pressure : (a) low pressure (5 torr), (b) atmospheric pressure (760 torr) 118

Fig. 94 Reflectance profile according to the plasmatron current: (t: 2min, P: 5 Torr, Ar: 3000 sccm, CF₄: 90 sccm, O₂: 500 sccm) 119

Fig. 65 Reflectance of the textured silicon surfaces according to the DC arc plasmatron current. (t: 30 sec., P: 760 Torr, Ar: 3000 sccm, SF₆: 100 sccm, O₂:500sccm) 120

Fig. 96 Reflectance of the textured silicon surfaces according to the O₂ concentration. (t: 30 sec., P: 760 Torr, Ar: 3000 sccm, SF₆: 100 sccm, Current: 100 A) 120

LIST OF TABLES

Table. 1 Characteristics of atmospheric plasma source(industrialized source)	6
Table. 2 Characteristics of atmospheric plasma source(still in laboratory source)	7
Table. 3 RF torches characteristics with a 6,000K Ar plasma	15
Table. 4 Persistent Lines of Neutral Argon (Ar I)	78
Table. 5 Experimental condition of the etching process at a low pressure	89
Table. 6 Experimental condition of the etching process at an atmospheric pressure	100

SUMMARY

Plasma used in dry etching, thin film deposition and surface treatment for display or semiconductor industries are operating at low pressures in general. However, low pressure processing is very costly due to the use of vacuum equipment and vacuum components. Subsequent wet processing is environmentally undesirable due to the use of a large amount of chemicals. Also, the usage of vacuum processing increases fabrication cost and decreases productivity. If stable atmospheric plasmas can be used, not only the decrease in processing costs but also the increase in productivity could be obtained.

New DC arc plasmatron with a hot rod cathode and cold nozzle anode was developed and its V-A (Volt-Ampere) characteristics were investigated. Outlook of the measured V-A characteristics cleared the question of the stability of arc burning in the new DC arc plasmatron. The plasmatron that has a stable operations with distributed anode spot could possibly be applied to plasma chemical processing. And measured value of the erosion rate for copper anode is $m_{Cu} \gg 3.6 \times 10^{-10} \text{ g/C}$ which is better than corresponding data for thermo-ionic emission cathodes made of tungsten $m_w \sim 10^{-9} \text{ g/C}$. These facts mean that plasmatron durability reaches $\sim 10^3 \text{ h}$. The low anode erosion rate is related to the large surface of arc-anode contact due to distributed anode arc spot, which reduces the current density. Unique characteristics of the new plasma source concerning its durability and plasma purity at rather low temperatures make it an interesting tool for technical applications, such as etching/deposition and chemical reaction.

To apply a plasma processing, the T-type plasmatron was modified to A-type. The A-type plasmatron was used to activate the CF_4 and SF_6 gases in etching experiments at atmospheric and low pressure. To reduce the recombination rate of

the activated gas particles inside a plasmatron and let them preserve their activated state outside, the whole device was installed outside of the vacuum chamber for vacuum processing. The experiment was provided on the mono-crystalline silicon wafer. The etching was carried out with plasma consisting of SF₆ (50 sccm) as a reactive etching gas with O₂ (300 sccm) as a supporting gas and Argon (2000 ~ 3000 sccm) as a cathode protecting gas. Etching rates were 60 μm/min at low pressure (3-5 torr) and 300 μm/min at a atmospheric pressure. The sample was positioned in such as way that the plasma flow axis would coincide with the side facet of the silicon crystal.

A texturing process was performed on a crystalline silicon (c-Si) wafer to increase the efficiency of a solar cell by using a high durability DC arc plasma source at atmospheric pressure and low pressure. CF₄ and SF₆ were used as the reactive etching gases at flow rates < 100 sccm, with O₂ as the supporting gas in the range of the 5 – 15 %. To survey the characteristics of the pyramid formation process, plasma texturing experiments were performed by varying the working time. The optimal operating conditions of the gas flow (Ar, O₂, CF₄, SF₆), plasmatron current and processing time were determined. The pyramid angle was approximately 50° to 60° when a single-crystalline silicon surface was textured in a vacuum whereas it was approximately 75° to 90° when textured at atmospheric pressure. The reflectance decreases with decreasing pyramid angle. The reflectance of the bare silicon ranged from 40 % to the 60 % but that of the textured silicon was approximately 5 % to 20 %. This reflectance is quite low, approximately half that reported by other studies using wet and reactive ion etching (RIE) texturing.

Even though DC arc plasmatron has many advantages, it is difficult to apply an industry due to the small applied area. To increase an effective processing area, we suggest a DC-RF hybrid plasma system. The DC-RF hybrid plasma system was designed and made. This system consists of a DC arc plasmatron, RF parts, reaction chamber, power feeder, gas control system and vacuum system. To investigate a DC-RF hybrid plasma, we used a Langmuir probe, OES (Optical

emission spectroscopy), infrared (IR) light camera. For RF matching, PSIM software was used to simulate a current of an impedance coil. The results of Langmuir probe measurements, we obtain a homogeneous plasma density and electron temperature those are about 1×10^{10} #/cm³ and 1 - 4 eV. The DC-RF hybrid plasma source is applied for plasma etching experimental, and we obtain an etching rate of 10 μ m/min. through a 90 mm of reaction chamber diameter.



I. INTRODUCTION

Plasmas are chemically active media. Depending on the way they are activated and their working power, they can generate low or very high "temperature" and are referred correspondingly as cold or thermal plasmas. This wide temperature range enables various applications for plasma technologies: surface coatings, waste destruction, gas treatments, chemical synthesis, machining.

Thermal plasmas (especially arc plasma) were extensively industrialized, principally by aeronautic sectors. Cold plasma technologies have been developed in the micro-electronics but their vacuum equipment limits their implantation.

Plasma used in dry etching, thin film deposition and surface treatment for display or semiconductor industries are operating at low pressures in general. However, low pressure processing is very costly due to the use of vacuum equipment and vacuum components. Subsequent wet processing is environmentally undesirable due to the use of a large amount of chemicals. Also, the usage of vacuum processing increases fabrication cost and decreases productivity. If stable atmospheric plasmas can be used, not only the decrease in processing costs but also the increase in productivity could be obtained.

1. Atmospheric Pressure plasma source

Depending on their design, the DC and low frequency discharges can work

either with a continuous or pulsed mode [1, 2, 3]. A pulsed working mode enables the injection of large energy amounts in the discharge while the system warming up is limited. On the other hand, a pulsed power supply is technically more complex a DC source and compromises the reproducibility of the process.

To understand clearly the place for this new device among numerous conventional DC arc plasma sources, it seems reasonable to review this field of technical equipment by comparing main features of different plasmatrons as below.

1.1 DC arc plasmatrons with hot rod cathode and cold nozzle anode

These devices are relatively simple and cheap, reliable and reaching high energy efficiency of about 90% [4]. Their hot cathode operating in thermo-ionic emission mode loses its mass only due to the evaporation that contaminates plasma negligibly. Usually it is made of tungsten and hot tungsten is chemically very active so such cathodes have to be protected with neutral gas flow, for instance, argon or nitrogen. Investigations showed that the mean erosion rate, mass of a W cathode is $m_w \sim 10^{-9}$ g/C with the protection [2, 3, 4]. Cold anode usually made of copper is destroyed much more intensively than cathode. Its mean erosion rate is 4 orders of magnitude higher: $m_{Cu} \sim 10^{-5}$ g/C (coulomb). So vapors of copper anode contaminate plasma badly and rapidly while asymmetrically eroding anode limit durability of such a plasmatron to some ~ 10 hours. Besides plasma thermodynamic state here is very close to equilibrium with a lower temperature limit of about 5,000 - 6,000 °K [5]. In this plasmatron, its chemical activity is quite moderate and can be used for processing of ceramic or refractory metal layers only because of elevated temperature.

1.2 DC arc plasmatrons with a cold thermo-chemical cathode (Hf, Zr) and cold nozzle anode

Such plasmatrons are also simple, inexpensive and reliable and hafnium or zirconium (Hf/Zr) is chosen as material for their cathodes. Such cathodes can work in direct contact with chemically active technical gases and consume them very economically [6]. Economic use of gas and energy helps to make these plasmatrons portable, suitable for hospitals, small shops, etc. Investigations showed that the erosion of thermo-chemical cathodes in stationary mode is rather slow: $m_{\text{Hf,La}} \sim 10^{-8} \text{g/C}$ [7, 8]. The thermo-chemical cathodes are destroyed gravely at the start-up moments. Then durability of plasmatron is determined not only by cathode erosion. As in any other DC plasmatrons here average plasma temperature is not less than some 3000-6000K and its state is close to thermal equilibrium, which means a quite moderate degree of plasma-chemical activity.

1.3 DC arc plasmatrons with cold tubular electrodes and arc revolving inside

Here both electrodes are destroyed quite noticeably. However, there exist designs of such a plasmatrons with practical durability more than for models described previously. In case of uniformly distributed electrode erosion of both electrodes, durability of this device with thick electrode walls can reach some $\sim 10^2$ hours [9]. The result is achieved under the combined action of gas vortex and complicated electromagnetic forces that cause revolving arc [10]. In these devices general erosion rate of electrode and plasma contamination are higher because erosion rate for a cold copper cathode is usually about three times more than for an anode. Note that gas consumption here is high enough, which is necessary for internal vortex formation.

1.4 AC three-phase arc plasmatron

They feature high energy effectiveness and simplicity of power sources reduced in this case into a conventional power network of industrial frequency. On the other hand, the drawbacks of the previous point remained here unchanged. Besides the

power level of such a plasmatrons is relatively high limiting their use in electronic industry as well as in another high-tech industrial branches.

1.5 RF arc plasmatron

Such plasmatrons are very good from at standpoint of plasma contamination because they can easily be made electrodeness or one-electrode (pilot) type with very low erosion rate. Besides chemical activity of plasmas here is high due to its thermally non-equilibrium state: $T_e \gg T_G$. On the other hand, thermal efficiency of such as plasmatron is limited to some 60-65%; power level, plasma temperature and gas flow rates here are not small; power sources are complicated, unreliable and difficult to adjust; these plasmatrons are dangerous for attending personnel and generate radio noise trouble some to suppress.

1.6 Microwave Plasmatrons

Nearly the same applies to microwave atmospheric plasmatrons except that their thermal efficiency is nearly 50% higher reaching about 95% and danger to people around is much more severe.

Concerning to development of plasmatron with high durability, new technical means that slows down the erosion process of anode material is described in order to reduce contamination of generated plasma flow. The essence of the concept is cleared out in schematic diagrams given in Fig. 1. Engineering decisions are disclosed in the designing-assembly draft of the latest modification of the plasmatron and in the description of experimental solutions of the main design problems.

1.7 Dielectric Barrier Discharge (DBD) plasma

DBD is a typical non-equilibrium high pressure ac gas discharge. It is known that the DBD can be occurred between two electrodes, at least one of which should be covered with dielectric, when an ac high voltage is applied on the electrodes.

The dielectric is the key for the proper functioning of the discharge, i.e. limits the current flow to the system, and distributes the discharge almost uniformly over the entire electrode area.

The DBD device (see fig. 1) consists of two plane-parallel metal electrode: at least one of these electrodes is covered by a dielectric layer. To ensure stable plasma operation, the gap which separates the electrodes is limited to a few millimeters wide. Plasma gas flows in the gap. The discharge is ignited by means of a sinusoidal or pulsed power source. Depending on the working gas composition, the voltage and frequency excitation, the discharge can be either filamentary or glow. A filamentary discharge is formed by micro-discharges or streamers that develop statistically on the dielectric layer surface.

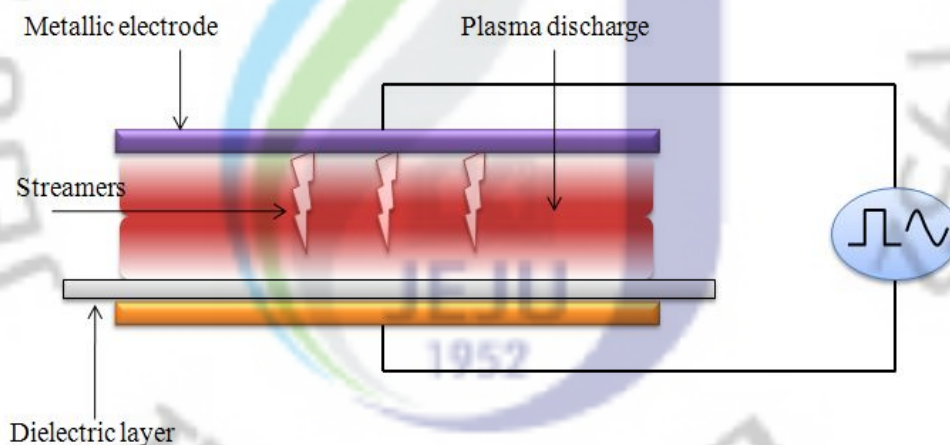


Fig. 1 Principle of dielectric barrier discharge.

Table 1. Characteristics of atmospheric plasma source(industrialized source)[11]

Excitation	Source	Plasma properties	Operating conditions
DC/Low frequency	Arc torch	$T_e = T_h \approx 8,000 \sim 14,000 K^s$ $n_e = 10^{21} \sim 10^{26} m^{-3}$	Gas: Ar/He Gas flow: 10~150 slm Power: 10~100kW
	Plasmatreat	$T_h < 700 K$	Gas: air Gas flow: 117 slm
Pulsed DC/Low frequency	Corona	$T_e = 40,000 \sim 60,000 K$ $T_h < 400 K$ $n_e = 10^{15} - 10^{19} m^{-3}$	Gas: air
	DBD	$T_e = 10,000 \sim 100,000 K$ $T_h < 700 K$ $n_e = 10^{18} - 10^{21} m^{-3}$	Some 100 W Plasma gas: 5 - 40 slm
Radio frequency	ICP	$T_e = 6,000 \sim 11,000 K$ $n_e = 10^{21} \sim 10^{26} m^{-3}$	Gas: Ar/He Gas flow: 10~200 slm Power: 50~70kW
Pulsed radio frequency	IST	$T_h < 400 K$	Gas: surrounding air No gas flow Power: 20 kW
Microwave	Cyrannus	$T_h < 700 K$	Gas: Ar/O ₂ Power: 6 kW

Table 2. Characteristics of atmospheric plasma source(still in laboratory source)[11]

Excitation	Source	Plasma properties	Operating conditions
DC	Microplasma	-	Power: 500 V, 250 μ A
	Atmospheric Pressure Plasma Jet	$T_e = 10,000 \sim 20,000 \text{ K}^s, m, 1$ $T_h < 600 \text{ K}$ $n_e = 10^{17} - 10^{18} \text{ m}^{-3}$	Gas: O ₂ /He Gas flow: 50~90 slm Power: some 100 W
Radio frequency	Cold plasma torch	$T_e = 10,000 \sim 20,000 \text{ K}^s, 1$ $T_h < 700 \text{ K}$ $n_e = 10^{17} - 10^{18} \text{ m}^{-3}$	Gas: Ar Gas flow < 1 slm Power: 100 W
	Hollow cathode	$T_e = 3,000 \sim 11,000 \text{ K}^s$ $T_h < 800 \text{ K}$ $n_e = 10^{17} - 10^{18} \text{ m}^{-3}$	Gas: Ar, He Gas flow < 2 slm Power: 100 W
	Micro-plasma CCuP	$T_e = 1,850 \sim 2,300 \text{ K}$	Gas: Ar Gas flow < 0.2 slm Power: 5~25 W
	Torch a Injection Axiale	$T_e = 13,000 \sim 14,000 \text{ K}^s$ $T_h = 2,400 \sim 2900 \text{ K}^s$ $n_e = 10^{21} \text{ m}^{-3}$	Gas: He Gas flow: 2~6 slm Power: 0.1~2 kW
Microwave	Microwave Torch Discharge	$T_e = 17,000 \sim 20,000 \text{ K}^s$ $T_h = 1,500 \sim 4,000 \text{ K}^s$ $n_e = 10^{22} \text{ m}^{-3}$	Gas: N ₂ Gas flow: 1~3 slm Power: 100~400 W
	Microwave Plasma Jet	$T_e = 16,000 \sim 18,000 \text{ K}^s$ $T_h = 5,000 \sim 10,000 \text{ K}^s$ $n_e \approx 10^{20} - 10^{21} \text{ m}^{-3}$	Gas: Ar Gas flow: 2~7 slm Power: 2~5 kW
	Microwave Plasma Torch	$T_e \approx 3,000 \sim 11,000 \text{ K}^s$ $T_h \approx 800 \text{ K}$ $n_e \approx 10^{19} \text{ m}^{-3}$	Gas: Ar Gas flow < 1 slm Power: some 100 W

2. Plasma Etching

Up until the late 1960's chemical etching, also called wet solvent etching, was the key technology to integrated circuit manufacturing. Indeed, from the standpoint of manufacturing, wet etching provides low etching preclude the use of this technique for micron and submicron pattern sizes. The most serious limitation is that of isotropic etching, which results in undercutting of the mask material and hence limits the minimum size of the pattern. To obtain high-density packing of micro-electronic circuits, anisotropic etching is essential. By the early 1970's CF_4/O_2 dry etching was widely adopted for patterning. It was widely recognized that dry etching offered the possibility of a vertical etch rate that greatly exceeded the horizontal etch rate (namely anisotropic etching). As a result, these dry etching techniques, which can generate anisotropic etch profiles, came into prominence.

Dry etching soon began to appear in IC fabrication. However, these dry etching technologies, like wet process, had their resolution limited by undercutting, and other, even more anisotropic etching techniques appeared. Among this was reactive ion etching (RIE). The RIE technique which has been widely adopted for IC fabrication until now provides moderate selectivity, etch rate and high anisotropy. In the mid-to-late 1970's research began on a dry etch technique which would combine the positive features of RIE with directional bombardment of the surface by ion accelerated through electrostatic sheaths.

Plasma etching processes are qualified by the etching rate, uniformity of etching over the surface as well as among substrates, directionality of the etched pattern, and selectivity of the materials to be etched.

One reads that there is cost saving associated with the process with higher etching rates, but it should be emphasized that high etching rates do not necessarily result in lower cost. Equipment size and yield are major cost considerations because the capital and operational costs of a clean room are a large fraction of total

expense. Factors controlling the high etching rate are, of course, RF input power (or sheath drop in physical terms), operating gas pressure and addition of gas to it, and gas flow rate.

3. Plasma Texturing for the Solar Cell

The PV industry is searching for new techniques to reduce chemical consumption in industrial solar cell processing. Crystalline silicon (c-Si) wafers are the foundation of today's rapidly growing photovoltaic (PV) industry. Module sales have increased 30-40% yearly for the last decade, with steadily increasing energy conversion efficiencies that now range from 14% to 20%. With the purpose to increase the light collection and efficiency of silicon solar cell, the reflection of the front surface needs to be minimized. This surface pattern can be changed by different techniques: plasma etching, and chemical etching. Silicon appears to be the near-ideal PV material - it is abundant, non-toxic, and industrially effective [12].

Silicon solar cells require a surface texturing to attain improved conversion efficiencies. Surface textures diminish reflection losses and cause an oblique coupling of light into silicon. The number of generated minority charge carrier increases, less of them recombine a route th the PN-junction and hence the cells current are enhanced. High-efficiency silicon solar cells need a textured front surface to reduce reflectance. Texturing of mono-crystalline silicon is usually done in alkaline solutions of wet-etching method [13].

The development of the effective and simple source of plasma for the technologic processes of surface treatment remains one of the important issues especially in the electronic industry. Use of DC arc plasmatrons in welding, soldering, and cutting of metals is well known. Among them, arc plasmatrons with cold thermo-chemical cathodes made of the hafnium or zirconium and cold nozzle anode (usually made of

copper) seem to be the most suitable and well-recognized devices. We applied a high durability DC arc plasma source to etch silicon mono-crystalline wafers at low pressures. Due to very low plasmatron anode erosion rate (about 10^{-10} g/C), the obtained plasma was nearly spectrally clean, that make it possible to use in electronic industry [14-17].

The second aim is testing of the plasmatron technique for decreasing of silicon substrates reflectivity index. It is the important task to develop a cheap new-age silicon based solar cells.



II. Theoretical Background

1. Atmospheric Pressure Plasma Source

1.1 DC arc Plasma Source

The arc plasma torches are fed by a DC power supply. They can be divided into categories: current-carrying arc and transferred arc [18]. They both consist of:

- ☞ A cathode where electrons are emitted
- ☞ A plasma gas injection system
- ☞ A nozzle which confines the plasma

In a current-carrying arc torch, the nozzle which is positively polarized is the anode. In the case of a transferred arc torch, the treated material is the anode whereas the nozzle is at a floating potential.

The arc is ignited between the cathode and the anode and ionizes the plasma gas. The plasma temperature varies from 8000 °K (plasma envelop) to 15000 °K (plasma core) which enables high temperature applications (use of the thermal effect of the plasma). An arc plasma is a very conductive media ($I = 50A \sim 600A$). The gas is highly ionized and the electronic density is about $3 \times 10^{23} \text{ m}^{-3}$.

Through the years, the arc plasma torches have been improved and are strongly implanted in industries:

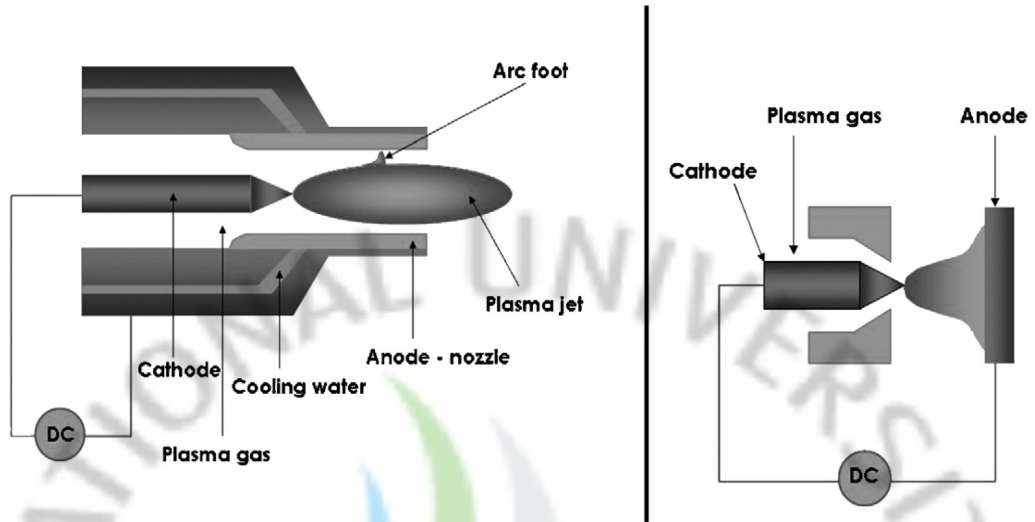


Fig. 2. Principle of arc plasma torches (left: current-carrying arc, right: transferred arc).



Fig. 3. High velocity Plazjet [19] (Tafa, Praxair).



Fig. 4. Sultzer Metco Triplex II Plasma Spray Gun [20].

1.2 ICP torches

The inductive coupled radio frequency thermal plasma produced in a high pressure gas with power of the order of 100 kW is now gradually becoming an important source with high temperature and high reactivity, either for processing of new functional materials or destruction of circumstance depleting substances.

The inductive discharges have been known for a long while. The RF torch is simply designed (see Fig. 5) The plasma is initiated and maintained by an RF fed helical coil. The current that flows in the RF coil induces a time-varying magnetic field nearby the plasma zone. The resulting electric ring field accelerates the electrons and thus maintains the discharge. The frequency of the generated plasma is higher than 1 MHz. This frequency level implies that electrons can reach the torch wall. This lack of contact between the plasma and the wall reduces the

pollution of plasma and torch walls which enables to work with different gases: inert, reductive, oxidant, nitriding gas [21].

The plasma is a ceramic tube (quartz, silicon nitride) that is cooled by air or water, depending on the working power. The inductive torches work in a wide power range: 20 kW ~ 1000 kW, with a gas flow rate of 10 ~ 20 slm. A higher working power is accompanied with lower torch diameter and lower plasma frequency (see Table 3).

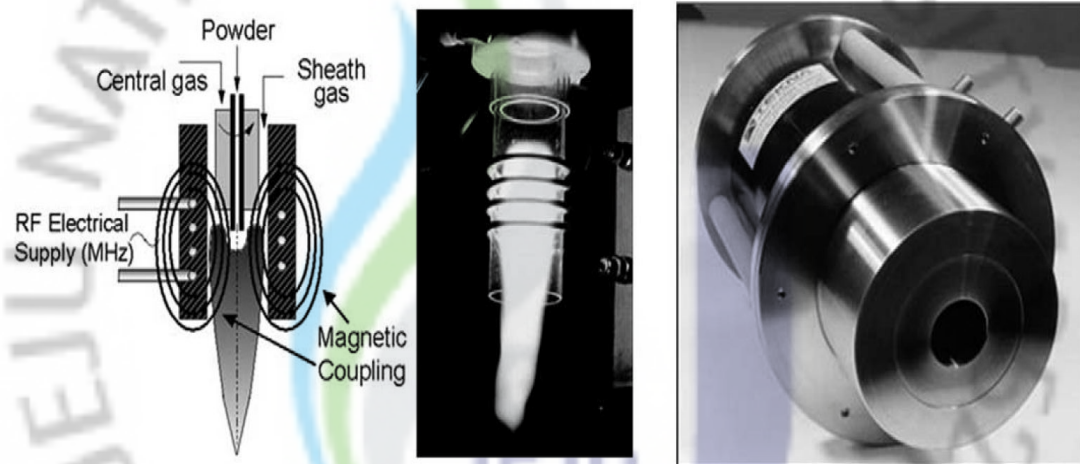


Fig. 5 RF plasma torch (Teckna Plasma system Inc) [22].

Table 3. RF torches characteristics with a 6,000K Ar plasma [23].

Working Power (kW)	Torch Diameter (mm)	Working Frequency (kHz)
50	42	1020
80	54	630
300	104	166
700	159	72

1.3 Dielectric Barrier Discharge (DBD)

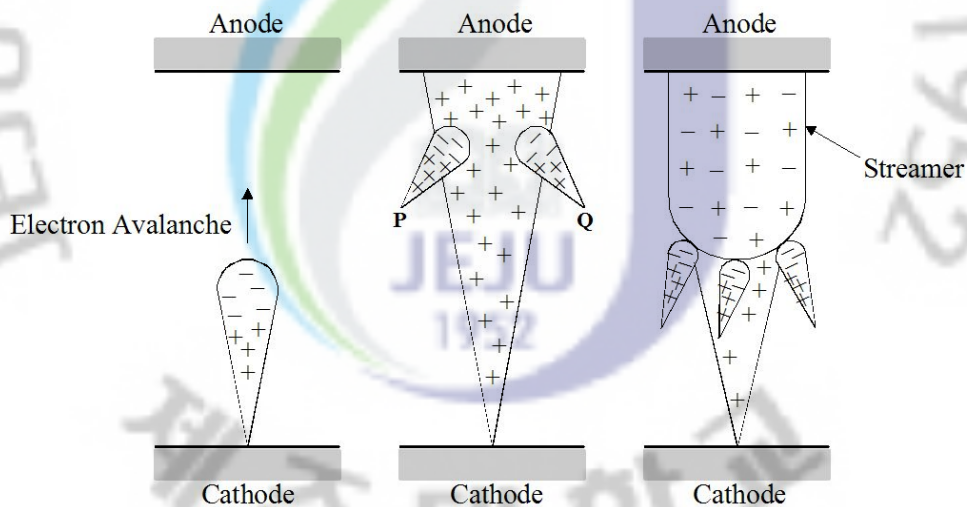


Fig. 6 Concept of the dielectric barrier discharge.

The DBD device (see Fig. 6) consists of two plane-parallel metal electrodes: at least one of these electrodes is covered by a dielectric layer. To ensure stable

plasma operation, the gap which separates the electrodes is limited to a few millimeters wide. Plasma gas flows in the gap. The discharge is ignited by means of a sinusoidal or pulsed [24] power source. Depending on the working gas composition, the voltage and frequency excitation, the discharge can be either filamentary or glow. A filamentary discharge is formed by micro-discharges or streamers [25] that develop statistically on the dielectric layer surface. The use of helium as plasma gas seems to favor a glow discharge (high energetic He metastable species, Penning effect).



2. Plasma Etching

Plasma etching has essentially replaced wet etching as a preferential method for accomplishing fine-line control and selective etching. The ability of plasma etching to provide anisotropy etching with close control of the fine dimensions and selectivity has made this transition possible. Plasma etching processes are qualified by the etching rate, uniformity of the etching over the material surface as well as among substrates, directionality of the etching, and selectivity of materials to be etched.

Consider the role of different chemical compounds applied in etching. Gases used for plasma etching can have, in general, quite complex compositions, because they essentially affect the balance between etch rate, etching selectivity, and anisotropy. The gas-phase compounds participating in the etching can be classified into the following six groups.

- **Saturates like CF_4 , CCl_4 , CF_3Cl , COF_4 , SF_6 , and NF_3 .** The saturates are chemically not very active and unable themselves either to etch or to form a surface film. They dissociate in plasma through collisions with electrons, producing chemically aggressive etchants and un-saturates.
- **Un-saturates like radicals CF_3 , CF_2 , and CCl_3 , and molecules such as C_2F_4 , and C_3F_8 .** The un-saturates can react with substrates, forming surface films. Sometimes, however, the un-saturates are able to etch a substrate, producing volatile products.

- **Etcants like atoms F, Cl, Br, and O and molecules such as F₂, Cl₂, and Br₂.**

Etchants are obviously the major players in etching processes; they are very aggressive, reacting with substrates and producing volatile products.

- **Oxidants like O, O₂, and so forth.** The Oxidants added to feed gas are able to react with unsaturates, converting them into etchants and volatile products.
- **Reductants like H, H₂, and others.** The reductants added to the feed gas are able to react with etchants and neutralize those producing passive volatile products.
- **Non-reactive gases like N₂, Ar, He, and so forth.** The non-reactive additives are some times used to control electrical properties of etching discharge and thermal properties of a substrate.

2.1 Etching rate, etching uniformity and area

Plasma etching processes are qualified by the etching rate, uniformity of etching over the surface as well as among substrates, directionality of the etched pattern, and selectivity of the materials to be etched.

One reads that there are cost saving associated with the process with higher etching rates, but it should be emphasized that high etching rates do not necessarily result in lower cost. Equipment size and yield are major cost considerations because the capital and operational costs of a clean room are large fraction of total expenses. Factors controlling the high etching rate are, of course, RF input power (or sheath drop in physical terms), operating gas pressure and addition of gas to it, and gas flow rate. The etching rate depends mainly on the plasma density and the densities of reactive radicals.

2.2 Isotropic Etching and An-isotropic Etching

Figure 7 shows a patterned resist on an oxide layer. The term "isotropic etching" means that etching proceeds at the same rate in all directions, resulting in the characteristic linear-circular profile shown in figure 7(b). By definition, anything that is not isotropic is anisotropic. However, in the directional process that can result in vertical wall profile (fig. 7(a)). Therefore, anisotropic, directional, and vertical etching are all used synonymously.

The directionality of etching is governed by the isotropic and anisotropic etching process. The principal motivation for the adoption of plasma etching is the ability to produce fine resolution in small ($\sim 1 \mu\text{m}$) devices, achieved by etching in a directional manner. Anisotropic ion-assisted straight-wall etching and isotropic profiles are the two extremes of directionality. Between these limits lie mixed combinations of these profiles. Anisotropic etching is necessary to attain small feature size ($\leq 3 \mu\text{m}$).

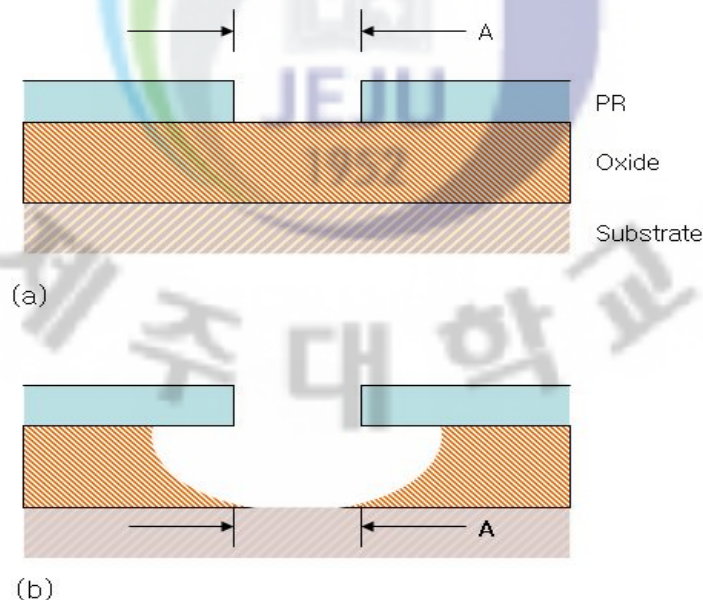


Fig. 7 Isotropic Etching and An-isotropic Etching.

2.3 Parameters of the etching condition

The surface kinetics of etching is controlled by concentrations of ions and active neutrals near the surface. Determination of these parameters requires a detailed consideration of etching discharges. Some useful relations, however, can be derived from general kinetics of the low-pressure discharges applied for etching. Concentration and flux of neutral chemically active etchant is also important parameter. A balance of charged particles in plasma between electrodes with area A (characteristic radius R) and narrow gap l between them ($l \ll R$), controlled by ionization and losses to the electrodes, can be estimated as

$$2n_i u_B A \approx k_{ion}(T_e) n_0 n_e l A, \quad (1)$$

where n_e , n_i , and n_g are the number densities of bulk plasma, ions at the plasma-sheath edge, and neutrals; $u_B = \sqrt{T_e/M_i}$ is the Bohm velocity; T_e is the electron temperature; M_i is an ion mass; and $k_{ion}(T_e)$ is the rate coefficient of ionization by direct electron impact, which strongly depends on electron temperature. The relation between the ion density n_i near the surface at the plasma-sheath edge and the bulk plasma density n_e can be expressed in the low-pressure case as

$$n_i = h_l \cdot n_e, \quad h_l = 0.86 \cdot \left(3 + \frac{1}{2\lambda_i}\right)^{-1/2} \quad (2)$$

where $\lambda_i = 1/n_0 \sigma_{i0}$ is the ion-neutral mean free path; $\sigma_{i0} = 10^{-14} \text{ cm}^2$ is a typical value of the ion-neutral collision cross section in the system. Thus, based on (8-5), electron temperature in the discharge can be determined as a function of

$n_0 l$:

$$k_{ion}(T_e) \approx \frac{2u_B h_l}{n_0 l} \approx 1.72 \cdot \frac{\sqrt{T_e/M_i}}{\sqrt{3 + (n_0 I)\sigma_{i0}/2}} \cdot \frac{1}{n_0 l} \quad (3)$$

The total discharge power can be expressed through the generation rate of charged particles and total discharge energy cost corresponding to the creation of a single electron-ion pair, E_{ei} (which depends on electron temperature, and numerically is about 100–300 eV):

$$P \approx 2AE_{ei}n_i u_B \quad (4)$$

Based on equation (8–8), we obtain a formula for calculating the near-surface ion density at the plasma-sheath edge, which, in surface kinetics, is given by

$$n_i = \frac{P}{2AE_{ei}u_B} = \frac{P}{2AE_{ei}} \sqrt{M_i/T_e} \quad (5)$$

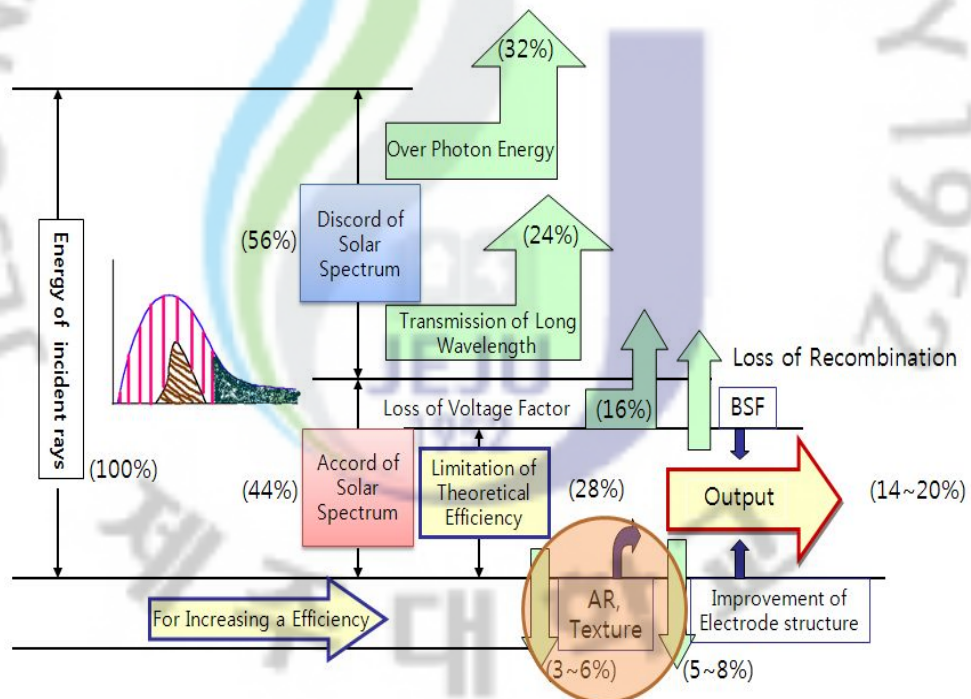
Finally, the ion flux at the etching surface, which is also required for etching surface kinetics calculations, can also be expressed as a function of the total power of the nonequilibrium low-pressure discharge:

$$\Gamma_i = n_i u_B = \frac{P}{2AE_{ei}} \quad (6)$$

As an example of applying expressions (8–9) and (8–0), we can derive a formula based on (8–3) for maximum anisotropy of the ion energy-driven etching as a function of the total discharge power:

3. Plasma Texturing for the Solar Cell

Bulk crystalline Si is presently the dominating photovoltaic technology and will probably remain so for the next two decades. The present solar cell processes make extensive use of Si etching steps. It is expected that these types of processes will gain in importance in the next few years, but also that they will face more stringent requirements in terms of Si consumption and surface morphology as the wafers used in the industry become thinner and more fragile.



Hideyuki Takakura, 太陽光發電, CMC, 2000. 9.

Fig. 8 Efficiency and loss factor in solar cell.

3.1 Silicon Texturing Processing in the Solar Cell

There are three steps in which Si etch is involved.

- Removal of the region near the surface of the wafers with many defects induced by the wire sawing process (saw damage)
- Texturing the front surface
- Removing the parasitic junctions formed at unwanted locations on the cell during the diffusion process

In the standard solar substrate cell processing process, texturing process becomes an essential process to improve the light trapping of the cell substrate. A new plasma texturing method is developed for decreasing the front surface reflection while limiting the amount of silicon removal during the texturing process.

3.2 Features of the Plasma Texturing Processing

- Improvement of efficiency of solar cell especially for multi-crystalline (mc-Si) substrate
- Single (front-) side process only
- Capable of handling thin substrate ($< 180 \mu\text{m}$)
- Proven in the thin film poly-silicon (c-Si) substrate

3.3 Advantage of plasma texturing

- The texturization can be executed independently from the shape of silicon surface.

- The cell performance is much more enhanced by the microscopic scale of the texture. Since the macroscopic feature of the surface texture, as obtained either wet chemical texturing, leads to an increased depletion area per cell area. This lowers the open circuit voltage (V_{oc}). The texture obtained by plasma etching has much lower feature size, giving a relatively lower depletion area after the diffusion of standard emitters as used in the PV industry. This leads to a relatively higher V_{oc} for plasma-textured cell.
- Better reliability & reproduction, easy to control.
- Less chemistry required (closer to correct stoichiometry)
- Does not require D.I. water
- Disposal of reaction products is standard (gas scrubber and abatement system). It is safer and less expensive.
- No dependence on parameters like wafer surface cleanliness, surface "reactivity" or "pyramid nucleation density", temperature and content of texturing bathes.

From an industrial point of view, it presents a strong potential for reduction of process cost. It is suitable for large, high throughput manufacturing. Results on cell level, using substrates with the conventional thickness, show that the cell efficiency of plasma-textured surfaces is superior compared to wet textured surfaces.

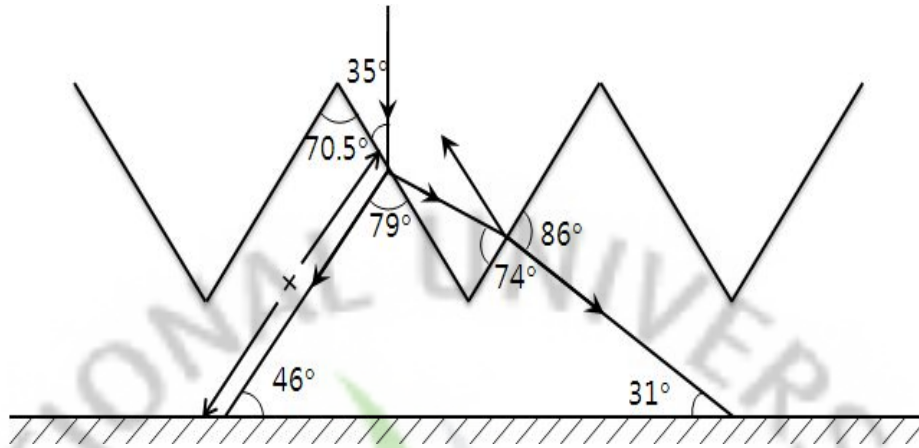


Fig. 9 Basic concept of the silicon texturing for the solar cell.

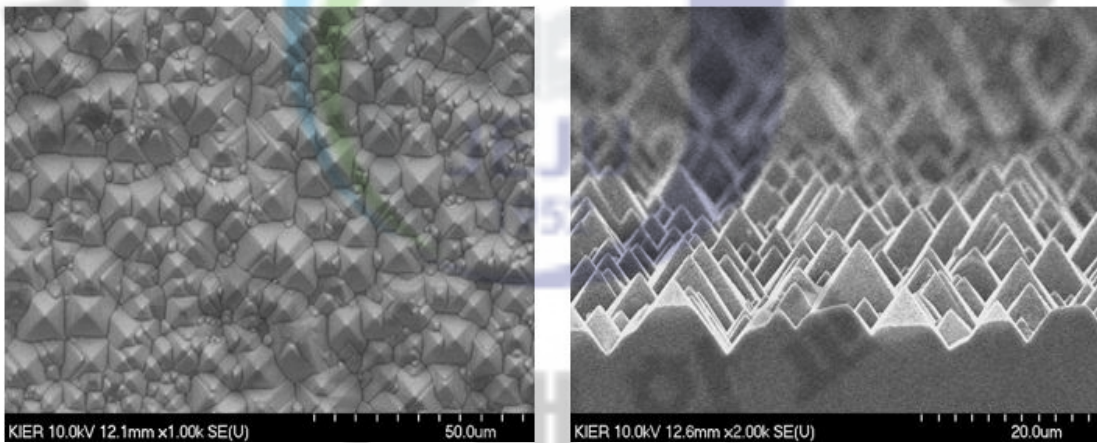


Fig. 10 Textured Silicon Surface (wet process).

III. Development of DC Arc Plasmatron

1. Development of a new DC arc plasmatron

1.1 The origin of technical decision.

The task of the present research was to reduce erosion process for a cold anode to the level of a hot cathode operating in thermo-ionic emission mode. The main idea was to arrange some intermediate formation like local vortex in discharge plasmas to connect arc with a cold anode. This intention was based on the phenomena discovered by the end of the 1960s: introduction of an abrupt expansion step on the internal surface of a tubular anode led to the formation of a local circular vortex on this step that fixed position of the spot. Vortex location appeared so stable that previously falling Volt-Ampere characteristics of such as plasmatrons changed into rising ones. In a conventional plasmatron with hot tungsten cathode, cold nozzle anode was connected to a sidewall of a tubular technologic channel forming a T-junction and the anode erosion rate slightly decreases.

To enhance the intensity of the vortex and its influence on the anode arc spot, we made technologic channel flat with height not more than $3d_A$ (d_A : anode orifice diameter). Pursuant of this change, the device could work continuously for several days and after cleaning anode surfaces from some dark deposit (presumably some copper and tungsten oxides) no traces of arc burning on its surfaces could be seen.

1.2 Main features of the plasmatron design.

Three projections of the plasmatron schematic diagram is presented in Figs 11 -

13. As it can be seen in the front view (Fig. 9) the device comprises a rod cathode 1 (tungsten) and a nozzle type, water-cooled anode 2 (copper). Its orifice is connected to the technologic channel 3 thus forming a T-junction of the two openings. Technical gas (fuel-air mixture, CF_4 , etc.) is supplied in the direction of the arrow 4, cathode protecting gas (Ar) comes along the arrow 5 into the sleeve of the Ar injector 6. Arrow 7 shows resulting plasma flow, 8 – presumable form of plasma vortex that is located beside the orifice of the anode 2 and seems to function as a distributed anode spot, 9 – arc discharge column. Rectifier pulse inverter TIG MICRO 350X was used as a power source operating in the mode of a direct current source for $I \leq 350A$. It is consolidated with an HF (high frequency) high voltage startup oscillator shown as a separate unit in Fig. 12. The oscillator's start button is united with normally short-circuit contacts connected to a voltmeter that monitors arc voltage to protect voltmeter against breakdown with high voltage from the oscillator at this point of arc excitation (usually oscillator's voltage reaches ~ 11 kV).

Left side view of this device (Fig. 13) discloses form and sizes of the technologic channel's cross-section: $H = (1 \dots 3)A$; $B = (3 \dots 5)A$ where A is diameter of the anode's orifice.

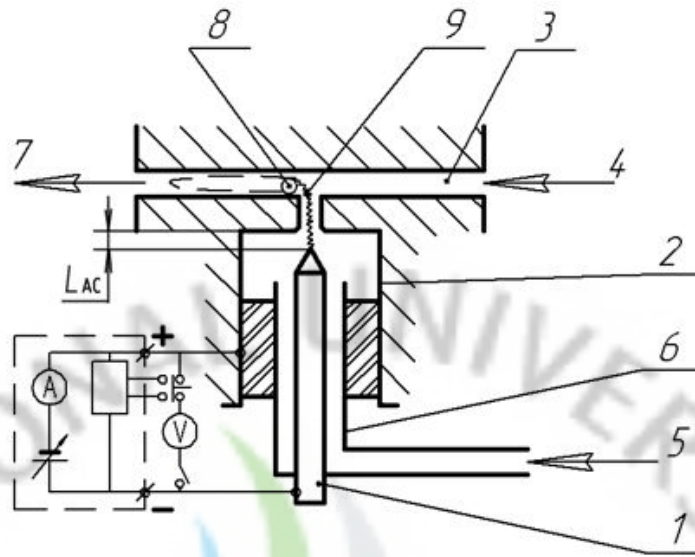


Fig. 11 Concept of the DC arc Plasmatron
 (1- cathode, 2- anode, 3- technologic channel, 4- process gas supply, 5- Ar supply, 6- Ar injector, 7 – plasma flow, 8 - presumable form of plasma vortex acting as a distributed anode spot, 9 - arc discharge column.)

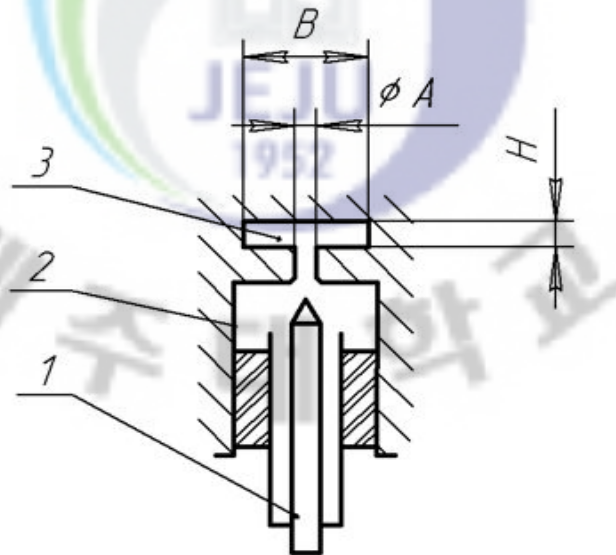


Fig. 12. Diagram of the T-plasmatron (front view).

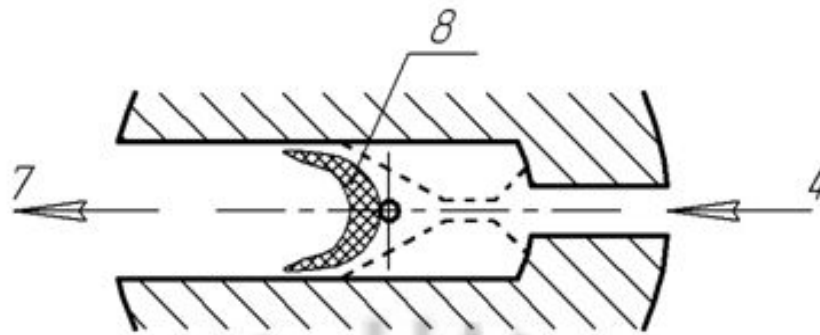


Fig. 13. Top view of the DC arc plasmatron.

Upper view of the device (Fig. 13) reveals a longitudinal form of the technologic channel: for subsonic flow mode, it was made straight (solid lines), for sonic and supersonic flow it had a form of the Laval nozzle (broken lines). Here the drawing of arc-shaped formation gives a tentative idea of the plasma vortex outlook operating as a large, distributed anode spot providing low arc current density. In the process of our experiments four essential modifications of plasmatron design were developed. Arc input power reached 2000 W. All tested plasmatrons were quite compact: they measured about $\text{Ø}40$ (160-200) mm. These designing efforts were directed mainly to work out an optimal way to cold electrodes.

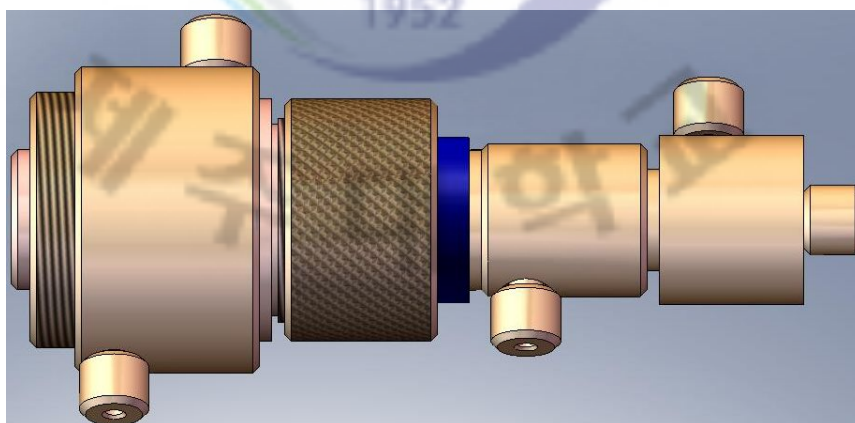


Fig. 14 Design of A-type DC arc plasmatron.

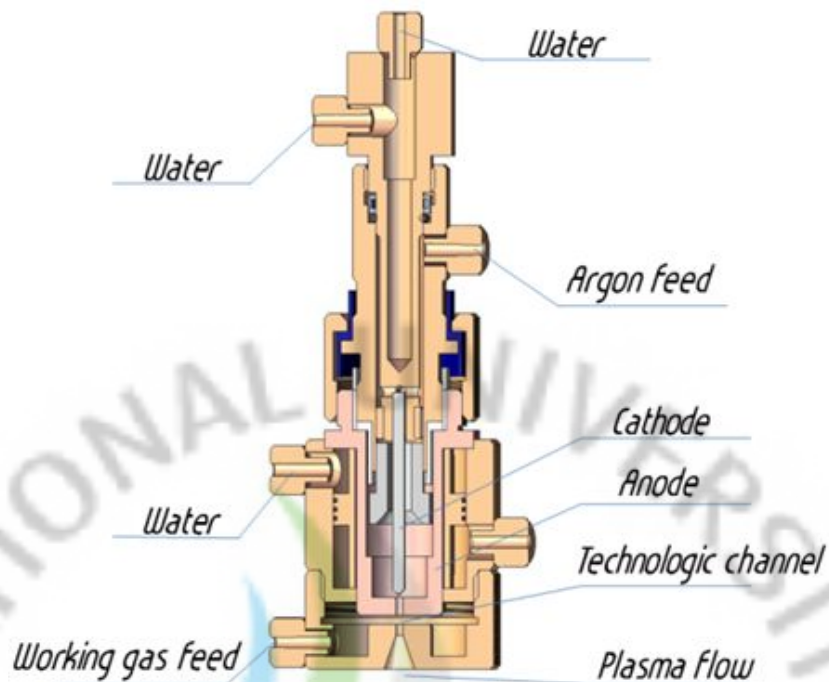


Fig. 15 Inside structure of A-type DC arc plasmatron.

Anode of this device is made as a water-cooled copper monolith integrated with sidewalls of the technologic channel. The last technical decision is acceptable in case of straight and wide channel; otherwise the technologic channel can be formed using two separate sidewalls to make a Laval nozzle for supersonic flow of process gas. Cathode rod was supposed to be made of tungsten operating in thermo-ionic emission mode.

Note that new plasmatron is reliably protected against a parasite electrical breakdown from HF HV oscillator responsible for contact-less arc startup: in the housing of the Ar injector, special grooves are provided under both inter-electrode insulators 11 and 12 increasing their electrical strength. Besides here housing 06 is made immovable regarding the anode and housing of the plasmatron: only cathode unit can be moved inside housing preserving optimal positions for both insulators. In this way stability of arc start-up is achieved.

1.3 Problem of the cathode

For cathode made of pure tungsten of 3.2 mm in diameter after steady operation at arc power ~ 1 kW, local melting on the cathode tip was observed due to arc heating at current $I=100$ A (melting point $\gg 3410^\circ\text{C}$). Local melting of the cathode material meant that cathode spot mode partially included liquid-metal mechanism with erosion rate $\sim 10^{-8}\dots 10^{-7}$ g/C, which consumed tungsten rather swiftly [26, 27].

According to a well known “minimum energy principle” arc discharges are automatically sustained at the possible minimum of energy input. In case of the pure tungsten cathode, this principle meant that at the considered power thermo-ionic current was not enough to reach 100 A; as a result energy input into the cathode increased: by-cathode potential drop had enhanced melting of the cathode tips to provide arc current of 100 A under joint operation of thermal-ionic emission and liquid-metal mechanisms.

Emission mechanism could be boosted by lowering work function of the cathode surface, for example, using thorium/lanthanum-doped tungsten (its work function is about 1.5 eV lower than for pure tungsten for which $j \gg 5$ eV). Experiments with Th-W cathodes confirmed the correctness of this step: at $I=100$ A nearly no traces of melting could be seen on the cathode surface.

From literature, it is known that by-cathode potential drop in case of the liquid-metal cathode mechanisms are $DU_C \sim 10^0\text{V}$ [26, 27] while for the thermo-ionic mechanism it is lower by one order of magnitude : $DU_C \sim 10^{-1}$ V. If in the first case cathode surface temperature reached 3410°C (exact checkpoint) than in the second one it could be $2800 - 3000^\circ\text{C}$.

1.4 Measurement of characteristics

1) Evaluation of the plasma temperature.

External plasma temperature was evaluated at the nozzle exit using a standard

thermocouples. At arc power up to 2000 W mean-mass temperature of plasmas was well within 100°C. Visual observations of plasma flow inside the technologic channel and tests with pure metal samples (gold – melting point 1064°C and copper – melting point 1083°C) showed that in the plasma flow at the anode orifice temperature was much higher than 1000°C because external view of this flow was similar to arc welding using free arc where temperatures usually are in the range 3000-6000°C. Accurate measurements of the inside plasma temperature are the further task of investigation work with the new plasmatron but definitely low exit temperature of the new device seems very unusual and interesting.

2) Measurements of the anode erosion rate.

After successful solution of the cathode problem accurate anode erosion measurements became possible. First of all, we made sure that for arc current, $I=100$ A numerous repeated arc start-up became easy. Then special experiment was carried out to determine anode mass ablation at one contact less. By 20 cycles of repeated start-up, specific anode mass ablation, $m_{ab-start}$ was measured as 0.14 mg/startup.

Working parameters of the plasmatron were as follows: d_A (anode orifice diameter) = 2.5 mm; d_C (cathode diameter) = 4 mm (W-Th); L_{AC} (anode-cathode distance) $\gg 2$ mm; Q_{Ar} (Ar flow rate) $\gg 2$ nl/min; Q_{air} (air flow rate) $\gg 20$ nl/min; $I=100$ A; $U \gg 12 - 13$ V; time of operation $t = 2 \times 9$ hours $\gg 6.48 \times 10^4$ s (with two start-ups).

After 18 hours of operation, anode mass reduction DM was determined to be 2.6 mg. Taking into account mass loss due to HF start-ups $2 \times 0.14 = 0.28$ mg we have

$$DM = 2.60 - 0.28 = 2.32 \text{ mg.}$$

Then for anode erosion rate we have

$$m_A = \frac{2.32 \cdot 10^{-3}}{10^2 \cdot 6.48 \cdot 10^4} \approx 3.6 \cdot 10^{-10} \text{ g/C}$$

Note that absence of arc traces on the anode surface after cleaning could be used as an express method for the anode spot mode evaluation. Similar results on the anode erosion rate were obtained for technologic channels of different forms tested so far: straight of different widths, diffuser and the Laval nozzle providing different values of working gas flow speed, subsonic and supersonic. According to the current level of our experience technologic channel must remain flat with height $H=(1\cdots3)\times d_A$ and width that least in the area just after the anode orifice $B=(3\cdots5)\times d_A$ at the Anode orifice diameter $d_A= 1.5\cdots3.5$ mm and plasmatron power up to 3kW.

3) Indirect evidence for the essence of the anode spot.

Long-lasting experiment ($t= 9$ hours) with wide and straight technologic channel (13.5x3 mm) left interesting traces on both external anode and internal anti-anode surfaces disclosing the essence and form of the anode spot in the plasmatron. The traces of discharge in anode and anti-anode surfaces after operation looked like in Fig. 15.



Fig. 16 Photo of the used copper anode.

The pictures show that whirl motion initiated by interaction of argon plasma flow from anode orifice and flat wind flow in the technologic channel has a transverse (crosswise) direction. This is the only reasonable way to explain side branches of traces left by plasma on both surfaces [28].

The whirl propagates to both sides from central part continuing interaction with the wind flow that bends them in its own direction. In such a way arc-like vortex is formed resembling “moustache”. Its central portion with the highest temperature heats air wind leaving to central trace on the anode surface. Side branches of the “moustache” can more or less effectively heat the anode surface when they turn enough in the direction of wind flow providing convective heat transfer from still hot revolving gas to the anode surface. In such a way, traces of these interactions appeared on the “floor” and “ceiling” of the technologic channel. As a result we believe that anode “spot” area of the new plasmatron fills all the cross-section of the technologic channel not leaving streamlines of the technical gas. This situation differs greatly from arc in a circular gap through which process gas flows continuously or high voltage breakdown discharges across the working gas flow in which only small portion of the working gas flow interacts with plasma streamlines.

Thus formed anode “spot” has a large surface of contact with the walls of the technologic channel significantly reducing arc current density, which explains the low level of anode erosion rate in the new plasmatron.

The anode erosion rate for new plasmatron fell down by not less than four orders of magnitude as in compared to the conventional apparatus: $\sim 10^{-10}$ g/C against $10^{-6}\dots 10^{-5}$ g/C respectively. This is a record figure for arc plasmatrons exceeding everything known in the field. The level of plasma flow contamination reached ~ 0.1 ppm, which allowed to consider thus generated plasmas as spectrally clean substance. At arc power up to 2 kW mean-mass temperature of plasmas leaving technologic channel’s nozzle was well within 100°C . At the anode orifice’s exit plasma temperature seemed much higher according to visual observations. Due to the presence of fast vortex in this area it can be supposed that here plasma is

not in thermal equilibrium ($T_e/T_{gas} \gg 1$). But this is a guess still to be confirmed experimentally either by direct temperature measurements or with the technical test of plasma-chemical activity.

2. Plasmatron arc spot

2.1 Cathode arc spot

In previously carried out experiments, it was found out that rod cathode made of pure tungsten for arc current up to 100 A does not work only at thermo-ionic emission mode: its tip melts supplementing emission electron current with charged particles from the liquid-metal cathode spot. It seems that pure Tungsten cannot provide to full discharge current operating only in thermo-ionic emission mode due to relatively high work function of the material. When thorium-doped tungsten was used at current 100 A cathode tip did not reach the melting point. Therefore, in this case necessity in liquid-metal mechanism to sustain the arc disappeared and the only electron emission phenomenon was responsible for arc current at which by-cathode voltage drop is much less than for liquid-metal mode. This fact means that at low and moderate currents W-Th cathode must work at a lower temperatures generating less stuff that can contaminate anode surface. However, at higher currents local liquid-metal cathode spot can appear to increase cathode voltage drop and uplifting general VAC. In this way ascending branch of VAC can be formed.

2.2 Anode arc spot

Experiments with wide technologic channel showed “petals” of arc traces on both anode and anti-anode surfaces. These traces revealed that vortex arising just

after anode orifice as a result of interaction between arc argon plasma and axis gas flow in the technologic channel revolves around an axis across the technologic channel forming two continuations on both sides that are bent with technologic wind flow. According to arc traces, total length of the vortex exceeds a width of the technologic channel filling its full cross-section.

On the other hand, low anode erosion rate prompts that anode spot must feature low current density, which can easily be achieved in the vortex of large contact surface if it plays a part of the anode spot. We can check this consideration experimentally because the area in question is located on the external anode surface subject to gas-dynamic interaction with wind flow in the technologic channel. So if the vortex is really an anode spot than experimental VAC outlook must show dependence on technologic gas speed. Experimental VACs confirmed these considerations – see discussion below.

3. Plasmatron characteristics

3.1 Current/voltage ripple for inverter power source

Experimental power source is of the inverter type with current ripple up to 50%. In figure 15 oscillograph trace for current in the model load resistor $R=0.7$ Ohm is presented. Ripple frequencies span the range $f = \sim 10^3 \dots 10^6$ Hz (high frequency peaks can be seen at another resolution of the instrument's display). Voltage ripple is shown for the arc discharge burning at current $I = 40A$ (Fig.15). Here ripple amplitude remains the same but the upper boundary of its frequencies is shifted up ($f \leq 10^7$ Hz). So we can consider our plasmatron to be a DC arc plasma source only conditionally.



Fig. 17 Current waveform of the DC arc plasmatron.

Fig. 18 Voltage waveform of the DC arc plasmatron.

3.2 Experimental VACs for the DC arc discharge in the plasmatron

VACs were measured using instruments with point-to-point method for current $I \leq 140$ A. Some of them were obtained when cathode had been made of pure Tungsten (in this case arc voltage usually was rather unstable) and others were measured when Cathode had been made of thorium-doped tungsten, which provided more stable behavior of arc voltage.

1) Variation of inter-electrode distance

VACs for $L_{AC} = 2$ and 4 mm are presented in Fig. 17. It can be seen that the curve for $L_{AC} = 4$ mm is shifted up by 2 V nearly equip distantly from another curve. This means that electric field in the positive column of the free burning arc $E = DU/DL_{AC}$ is independent of arc current and equal to $E = 2V / 0.2\text{cm} = 10\text{V/cm}$. Another arc portion is located in the anode orifice $\varnothing 2.5\text{mm}$. Here arc may not be stabilized at current $I \leq 60$ A judging by the form of VAC. In other words, in this channel it has nearly the same electric field strength $E \sim 10$ V/cm. The second side ratios allows to evaluate the anode voltage drop for say $I = 50$ A, $L_{AC} = 2$ mm, $U \gg 12.5$ V: for thermo-ionic emission Cathode $DU_C \sim 0.2$ V (typical literature data) and $DU_{\text{PosCol}} \sim 0.6 \times 10 = 6$ V (for the experimental device length of the anode orifice is 4 mm, which made a total length of the positive column equal to 6 mm). Then $DU_A \sim (12.5 - 6.2) = 6.3$ V. This result means that the value of anode voltage drop can constitute half of input arc voltage or half of applied electric power that is consumed in the distributed (vortex) anode spot. This result seems highly inspiring because it shows that as much as half of arc power can be used in the new plasmatron for direct plasma activation of process gas supplied into the technologic channel. The other part of plasma activation energy is delivered by Argon plasma ionized in the Cathode layer and positive column of the arc which is not very small. So working process of the new plasmatron is arranged in a way when the best part of arc power is used to activate process gas [29].

Let us evaluate the relative portions of power applied to anode sheath of the longer arc at $L_{AC} = 4$ mm and $I = 50$ A: $DU_C \sim 0.2$ V, $DU_{PosCol} \sim 0.8 \times 10 = 8$ V, $DU_A \sim (12.5 - 8.2) = 4.3$ V, i.e. about 30% of total arc power. In this case relative power applied to the Anode layer directly decreases and contribution of other arc parts increases, i.e. total arc power can be redistributed by variation of arc inter-electrode distance. So this approach to process parameter control can become useful for some technologies because different portions of input arc power can activate working gas differences.

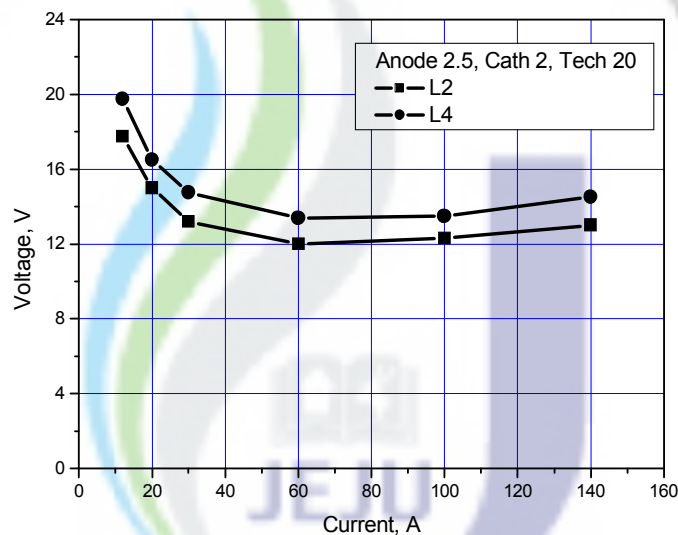


Fig. 19 VACs for $L_{AC} = 2$ and 4 mm.

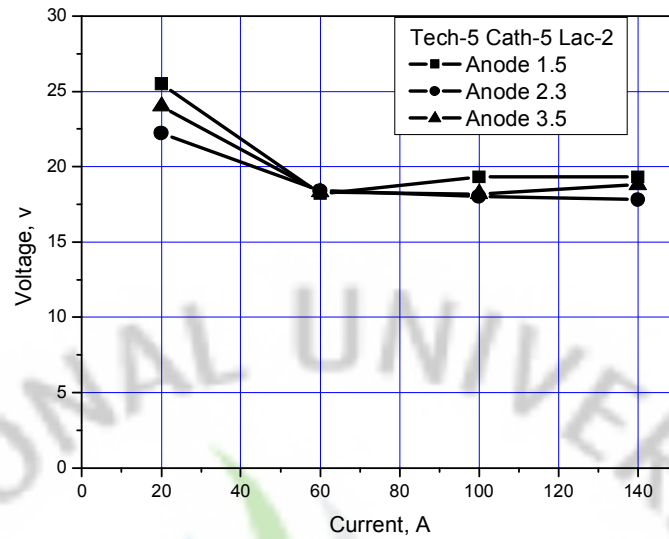


Fig. 20 VACs for anode = 1.5, 2.3 and 3.5 mm.

2) Variation of the Anode orifice diameter

In this case stabilizing influence of the anode orifice should begin at fewer currents for less d_A because for free arcs their cross-section grows with rising current. VACs for $d_A = 1.5 \dots 3.5$ mm are performed. It can be seen here that for $d_A = 1.5$ mm beginning of VAC growing portion can be indicated as $I \sim 60$ A while for $d_A = 3.5$ mm this value seems to be shifted to $I \sim 100$ A in accordance with preliminary considerations. As for the curve for $d_A = 2.3$ mm its behavior is not as definite, which is not surprising for cathode of pure Tungsten – material featuring unstable behavior of arc voltage.

3) Variation of the Argon flow rate in the Cathode channel

VACs for different argon flow rates in the cathode channel is presented in Figs 19a and 19b. All curves are separated from each other: the bigger flow rate the higher arc voltage. This effect quite clearly seems to be connected with the stabilizing action of the longitudinal gas flow: the higher argon flow rates the

higher gas velocity along the positive column of the arc discharge and the higher convective heat transfer from plasma to cold Argon. This fact means higher electric field strength in the arc positive column, i.e. higher voltage at the same arc current. In figure 19a anode orifice is rather narrow so the trend to the growing character of VAC with a increase of gas flow rate seems natural (note that here argon was used in both cathode and technologic channels). The other graph corresponds to nearly 3 times bigger Anode orifice cross-section so here this trend should not be seen (growing VAC for the low limit of Argon flow rate seems casual due to measurement errors; note that here Argon was supplied only into cathode channel; in the technologic channel air was supplied).



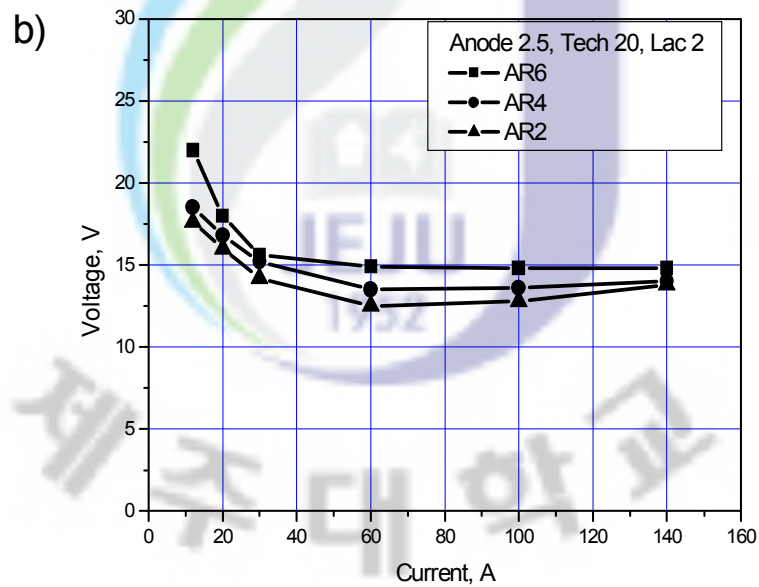
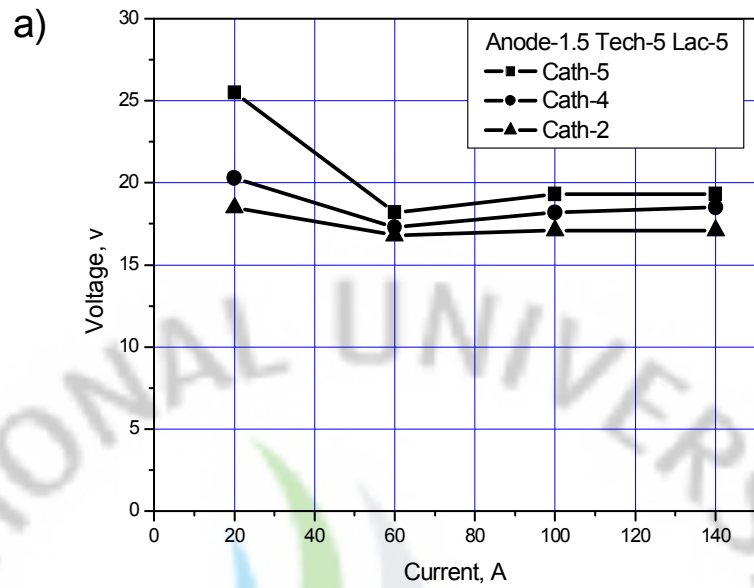


Fig. 21 VACs for different argon flow rates in the cathode channel.

4) Variation of gas flow rate in the Technologic channel

VACs for different gas flow rates in the technologic channel is presented in Figs 20a, 20b and 20c. Besides usual parameters here pressure in rotameters and channel cross-sections are given (one figure for a straight channel and two figures for the Laval nozzle channel: critical cross-section S_{CR} and channel width S_A beside Anode orifice where the central portion of the vortex should be located). The last parameter allow evaluation of gas flow speed in case of interest. These results show that when technologic gas flows slowly, at subsonic velocities, VACs do not vary with gas speed (Figs 20a and 20b; note that in Fig. 20a argon was used in both cathode and technologic channels; the rest data of figure 20 correspond to argon supply into the cathode channel only and air was supplied into the technologic channel). However, in case of supersonic air speed arc voltage decreases. This reaction means: 1) anode spot really does not hide inside anode orifice; it comes out and therefore, interacts with wind flow in the technologic channel; 2) this interaction does not change by-anode voltage drop DU_A for subsonic gas velocities; but in case of supersonic velocity DU_A decreases lowering energy input into anode. The first consequence confirms the idea of vortex anode spot realization and the second one is interesting to the standpoint of process parameter control. The last possibility needs separate check in future because a decrease of DU_A is accompanied by a increase of energy input into the other parts of the arc that returns into the technologic channel with argon plasma flow.

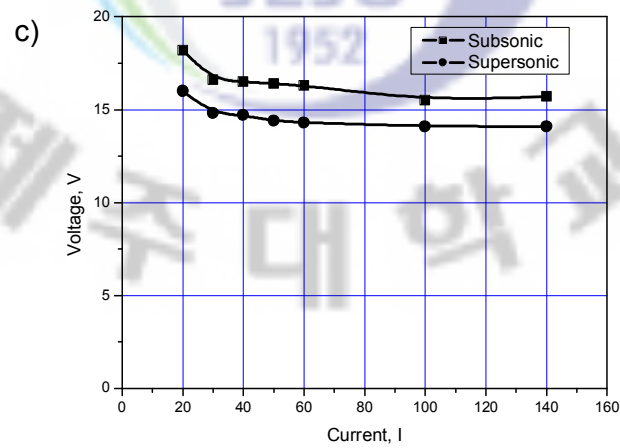
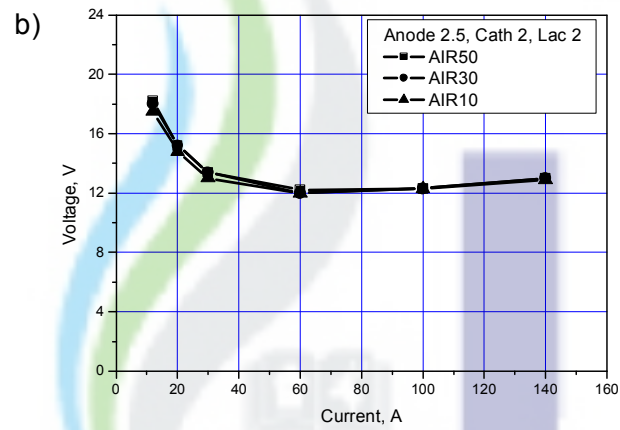
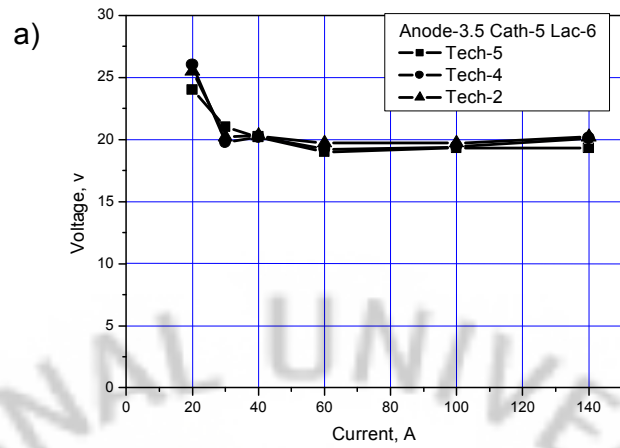


Fig. 22 VACs for different gas flow rates in the technologic channel.

3.3 Stability of arc working points for the new plasmatron

Note that all above given VA-characteristics $U_{ARC}(I)$ looks like falling curves that sometimes grow slowly a highest arc currents. The last character of the curves is interesting by itself, but it does not influence stability of arc burning or stability of its working points because the characteristic of power source working as current source $U_{PS}(I)$ falls steeply fulfilling the condition of stable burning of arc discharge

$$\frac{\partial U_{ARC}}{\partial I} > \frac{\partial U_{PS}}{\partial I}$$

for $I \geq I_{min}$. Four experiments after the start of the plasmatron at the zero position of the current regulator in the power source arc burned stably beginning from currents, $I \geq 10A$. So it seems this value of arc current was the lower current boundary I_{min} for stable work of our system plasmatron-power source.

4. Discussion

New DC arc plasmatron with a hot rod cathode and cold nozzle anode was fabricated and its V-A characteristics were investigated. Outlook of the measured VA-characteristics cleared the question of the stability of arc burning in the new plasmatron. Arc voltage reacts noticeably on arc length, stabilizing influence of the anode orifice wall and longitudinal gas velocity and also on subsonic/supersonic change of gas flow velocity in the technologic channel. Sensitivity of VA-characteristics to gas flow velocity in the technologic channel confirmed the notion of the external vortex nature of the anode arc spot that does not hide inside the anode orifice but comes out and interacts with gas flow. The plasmatron that

has a stable operations with distributed anode spot could possibly be applied to plasma chemical processing. Thorium/Lanthanum-doped tungsten was found to be the most suitable material for Cathode working in thermal-ionic emission mode.

Measured value of the erosion rate for copper anode is $m_{Cu} \gg 3.6 \times 10^{-10} \text{g/C}$ which is better than corresponding data for thermo-ionic emission cathodes made of tungsten $m_w \sim 10^{-9} \text{g/C}$. These facts mean that plasmatron durability reaches $\sim 10^3 \text{ h}$ and the level of plasma flow contamination with electrode material vapour about $\sim 10^{-1} \text{ ppm}$. Such working durability meets requirements for the toxicity reduction systems presented in reference . The low anode erosion rate is related to the large surface of arc-anode contact due to distributed anode arc spot, which reduces the current density. Unique characteristics of the new plasma source concerning its durability and plasma purity at rather low temperatures make it an interesting tool for technical applications, such as etching/deposition and chemical reaction.

IV. Development of the DC-RF hybrid plasma source

A radio frequency induction coupled plasma (RF-ICP) flow has many advantages such as large plasma volume, pure plasma and low gas velocity. Then, an DC-RF flow has been investigated intensively [30-33]. Then, an DC-RF flow is applied to the material processing such as spraying, fine particles synthesis. On the other hand, an DC-RF flow has some disadvantages such as a difficult ignition and an easy extinction under some operating condition. A typical argon ICP torch consists of an assembly of three concentric quartz tubes surrounded by the load coil of an RF generator. The ignition of the discharge can be achieved by using a graphite rod inserted into the torch and then removed or, for small torches, by a high frequency Tesla coil. Therefore, a direct current (DC)-radio frequency (RF) hybrid plasma flow has been expected to overcome these disadvantages of an RF-ICP flow [34].

A DC-RF hybrid plasma flow is composed of an DC-RF flow, which is used as a main plasma, and a DC plasma jet mounted on the DC-RF torch, which is used as a supplement. Its applications have been investigated by Yoshida intensively so far. In a DC-RF hybrid plasma flow, a DC plasma jet is used to ignite an RF-ICP flow and maintain it stably [35-37]. However, a DC-RF hybrid plasma flow has a complicated flow structure due to the strong interaction between a DC plasma jet and a RF-ICP flow [38]. Then an RF-ICP flow becomes unstable easily and is extinguished in a DC-RF hybrid plasma flow [39-40]. Therefore, it is very important to clarify the interaction between the flow structure and the characteristics of a DC-RF hybrid plasma flow. In the present study, we clarify the characteristics of a DC-RF hybrid plasma flow in terms of plasma stability, excited temperature, downstream gas temperature and upper limit of the injected reactive gas flow

quantity for the various operating conditions. Then we optimized the operating condition to enhance the plasma functionalities, which can be utilized for surface and coatings technology.

1. DC-RF hybrid plasma system

1.1 The electric fields calculation

The electric field profile in the plasma sheath of an argon RF plasma has been determined by measuring the equilibrium height and the resonance frequency of plasma-confined micro-particles. In order to determine the electric field structure at any position in the plasma sheath without the discharge being changed or disturbed an additional, non-electric, force is introduced which does not alter the plasma conditions, but which does allow for manipulation of the particle position, induced by a centrifuge. Consequently, the electric field and the particle charge can be determined as function of the position in the plasma, using one and the same particle for calculation at several positions throughout the reaction chamber. Current of the induction coil (A) is shown as below;

$$A = \frac{U_{amp}}{(R^2 + (\omega_L - \omega_{red})^2)^{1/2}}$$

Here, R is a resistance of the induction coil, we assumed that R is 1Ω.

$$\omega_L = \omega_f \times L_{coil} \times 10^{-6}$$

$$w_f = \omega_f \times C_{red}$$

$$U_{amp} = (U_{power}^2 + \frac{I_{power}^2}{(\omega_f + C_{tune})})^{1/2}$$

```

Nm = Cells(3, 2).Value
R = Cells(4, 2).Value/200
L = Cells(5, 2).Value/100
Curr = Cells(6, 2).Value
H= Cells(7, 2).Value/100
Pt = Cells(8, 2).Value/100
w = 2*3.1415925*Cells(9, 2).Value*1000*1000

Etot = 0
For n = 1 To Nm
  z = L/(Nm-1)*n
  E = 0
  For x = 1/1000 To Pt Step 1/ 1000
    Bz = 0
    For i = 1 To 360
      f = 2 * 3.1415925 / 360 * i
      Bz = Bz + (R * R - R * x * Cos(f)) / _
        (x * x + R * R + z * z - 2 * x * R * Cos(f)) ^ 1.5 * _
        2 * 3.1415925 / 360
    Next i
    Bz = Bz * Cur / 10000 / 1000
    E = E + Bz * x * 1 / 1000

  Next x
  E = E * w / Pt
  Etot = Etot + E

Next n

```

```

Cells(12, 2).Value = Etot

End Sub
Sub integralb()

Nm = Cells(3, 2).Value
R = Cells(4, 2).Value / 200
L = Cells(5, 2).Value / 100
Cur = Cells(6, 2).Value
H = Cells(7, 2).Value / 100

Pt = Cells(8, 2).Value / 100
w = 2 * 3.1415925 * Cells(9, 2).Value * 1000 * 1000

Etot = 0
'For n = 1 To Nm
' Z = L / (Nm - 1) * n
'E = 0
'For x = 1 / 1000 To Pt Step 1 / 1000
  Bz = 0
    z = 0
    x = 0
  For i = 1 To 360
    f = 2 * 3.1415925 / 360 * i
    Bz = Bz + (R * R - R * x * Cos(f)) / _
      (x * x + R * R + z * z - 2 * x * R * Cos(f)) ^ 1.5 * _
      2 * 3.1415925 / 360
  Next i
  Bz = Bz * Cur / 10000 / 1000
  Cells(12, 4).Value = Bz
  Cells(12, 6).Value = Cos(3.1415926)

'E = E + Bz * x * 1 / 1000

'Next x
'E = E * w / Pt
'Etot = Etot + E

```

```
'Next n  
Cells(12, 2).Value = Etot  
End Sub
```



Fig. 23 Calculated electric fields according to the number of turns.

Fig. 24 Distribution of electric fields.

1.2 RF impedance matching

Impedance matching is necessary in the design of RF circuit to provide the maximum transfer of power between a electric power and load. Probably the most vivid example of the need for such a transfer of power occurs in the front end of any sensitive receiver. Obviously, any unnecessary loss in a circuit that is already carrying extremely small signal levels simply can not be tolerated. Therefore, in most instances, extreme care is taken during the initial design of such a front end to make sure that each device in th chin is matched to its load.

There is a well-known theorem which states that, for DC circuits, maximum power will be transferred from a source to its load if the load resistance equals the source resistance. A simple proof of this theorem is given by the calculations and the sketches shown in Fig. 25. In the calculation, for convenience, the source is normalized for a resistance of one ohm and a source voltage of one volt.

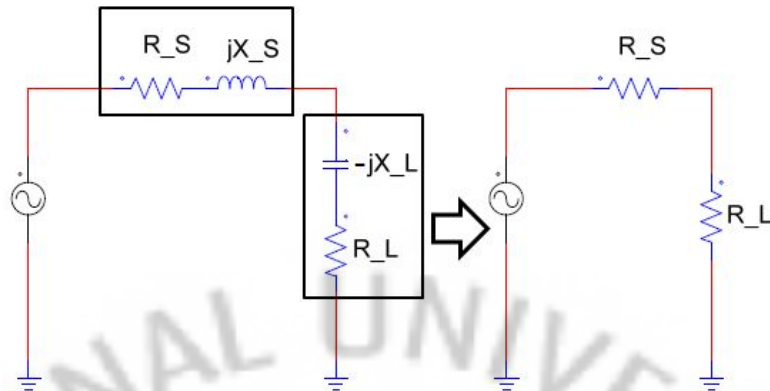


Fig. 25 Source impedance driving its complex conjugate and the resulting equivalent.

In dealing with AC or time-varying wave-forms, however, that same theorem states that the maximum transfer of power, from a source to its load, occurs when the load impedance (Z_L) is equal to the complex conjugate of the source impedance. Complex conjugate simply refers to a complex impedance having the same real part with an opposite reactance. Thus if the source impedance were $Z_s = R + jX$, then complex conjugate would be $Z_s = R - jX$.

The primary objective in any impedance matching scheme, then, is to force a load impedance to "look like" the complex conjugate of the source impedance so that maximum power may be transferred to the load. This is shown in Fig. 25.

Knowing the electrode plasma load impedance Z_L , the output voltage V_L and, most important, the load current I_L , a suitable matching circuit can be designed. Goals of the matching circuit design are:

- Wide matchable load impedance range for all process conditions.
- A stable range of operation covering rf power, all rf voltages and all rf currents occurring in the circuit for all load impedance conditions including the non-ignited case as well as all possible mismatch conditions.
- High efficiency (low losses).

- Smooth tuning characteristic.
- Automatic tuning, achieving less than 1% reflected power for all load impedances, stable and fast tuning from all possible start positions, ability to handle the non-ignited state and the ignition step.

Most RF generators are designed to operate into a $50\ \Omega$ load because that is the standard the industry has settled on for measuring and transferring high-frequency electrical power. The function of an impedance matching network, then, is to transform the resistive and capacitive characteristics of the plasma $50\ \Omega$, thus matching the load impedance to the AC generator's impedance.

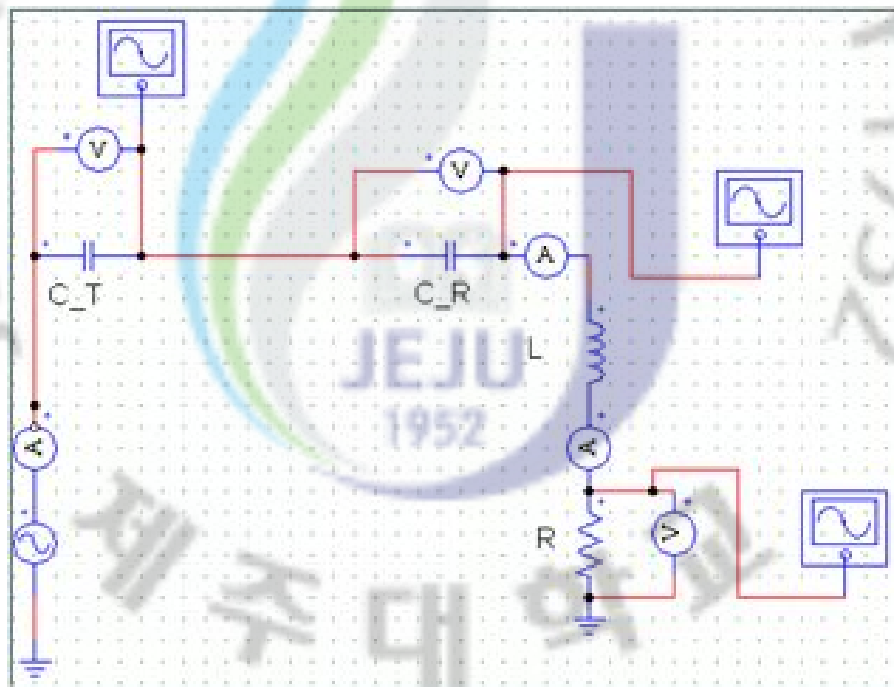


Fig. 26 RF impedance matching circuit.



Fig. 27 Electric current of the RF matching circuit
(C_T: 738.7 pF, C_R: 42.0 pF)

Fig. 28 Electric current of the RF matching circuit
(C_T: 738.7 pF, C_R: 42.30 pF)

Fig. 29 Electric current of the RF matching circuit according to the reduced capacitance.



Fig. 30 Picture of the variable capacitor.



Fig. 31 Picture of the matching part.

Figure 30 shows a vacuum variable capacitor. The range of the capacitor is from 1 to 1500 pF. Figure 31 shows a composed RF matching circuit. When dealing with the practical implementation of RF applications, there are always some nightmarish tasks. One is the need to match the different impedances of the interconnected blocks. Typically these include the antenna to the low-noise amplifier (LNA), power-amplifier output (RFOUT) to the antenna, and LNA/VCO output to mixer inputs. The matching task is required for a proper transfer of signal and energy from a "source" to a "load."

At high radio frequencies, the spurious elements (like wire inductances, interlayer capacitances, and conductor resistances) have a significant yet unpredictable impact on the matching network. Above a few tens of megahertz, theoretical calculations and simulations are often insufficient.

1.3 DC-RF hybrid plasma system design

Figure 32 shows a schematic of the experimental apparatus of DC-RF hybrid plasma. They are consisted of DC arc plasmatron, reaction chamber, vacuum chamber, matching parts and gas injection parts. DC arc plasmatron is set on the reaction chamber and

Figure 32 shows the schematic of the experimental apparatus. This system consists of DC-RF plasmatron, reaction chamber, power feeder, gas control system and vacuum system. Figure 33 shows the schematic of a DC-RF hybrid plasma and gas injection system. This plasma system consists of 3-turn RF induction coil, DC arc plasmatron which is mounted on an RF system and quartz tube of 100 mm outside diameter. There are three gas injection modes to control a plasma flow. The argon gas is injected through the nozzle of the DC arc plasmatron. The argon gas is discharged to produce a DC arc plasmatron and protect a cathode. The swirl gas is injected to add centrifugal force.

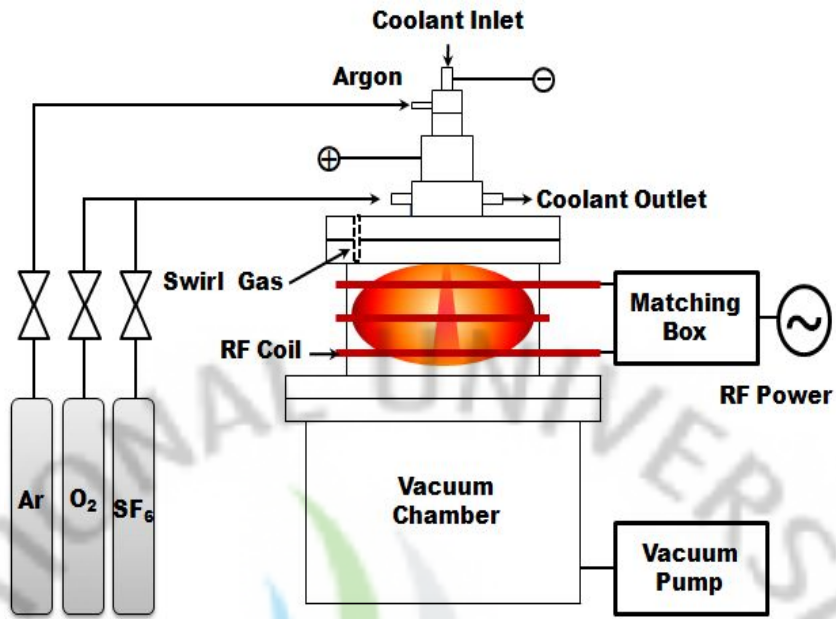


Fig. 32 Schematic of the experimental apparatus of DC-RF hybrid plasma.

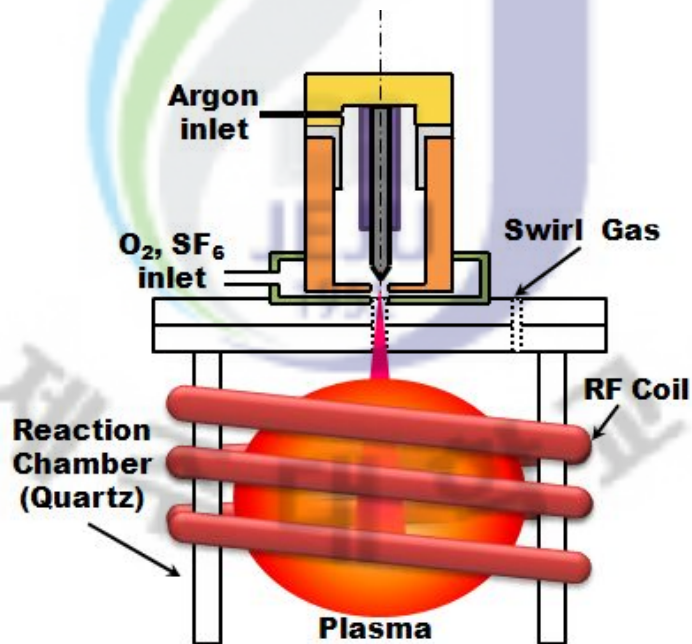


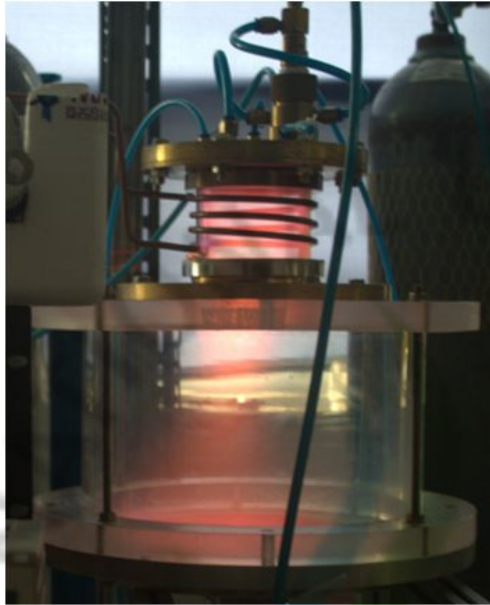
Fig. 33 Schematic of a DC-RF hybrid plasma and a gas injection system.

2. Characteristics of the DC-RF hybrid plasma

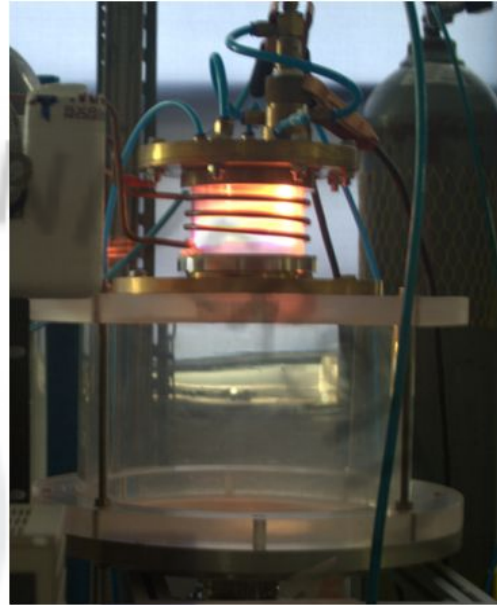
To investigate a DC-RF hybrid plasma, we used a Langmuir probe, OES (Optical emission spectroscopy), infrared (IR) light camera. A Langmuir probe is used for understanding a electron temperature and density. To understand a optical characteristics DC-RF hybrid plasma, we used a optical emission spectrometer. Infrared camera is used for measuring a plasma gas temperature distribution.



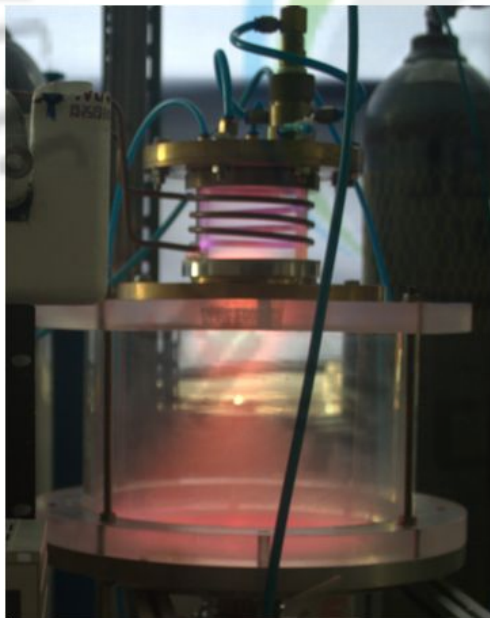
2.1 DC-RF hybrid plasma discharge



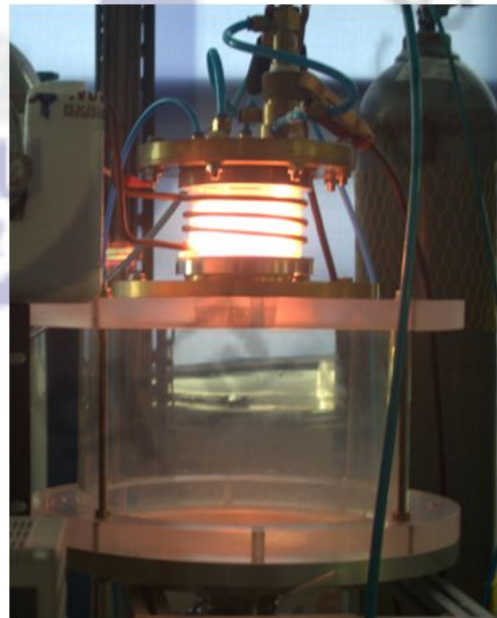
(a) RF: 0.5 kW, 3 Torr



(b) RF: 0.5 kW, DC: 1 kW, P: 3 Torr

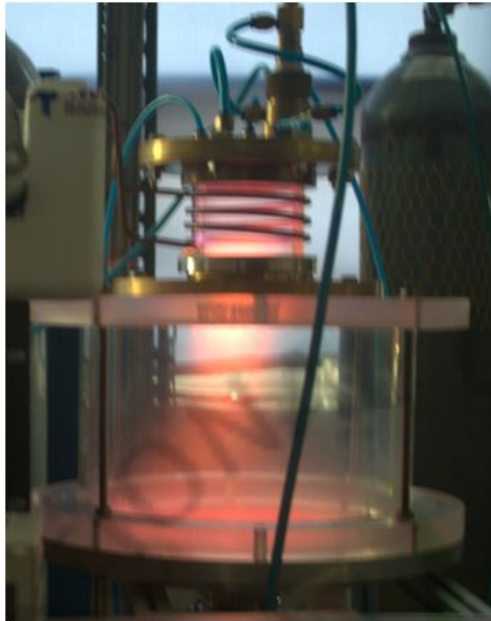


(c) RF: 1 kW, P: 3 Torr

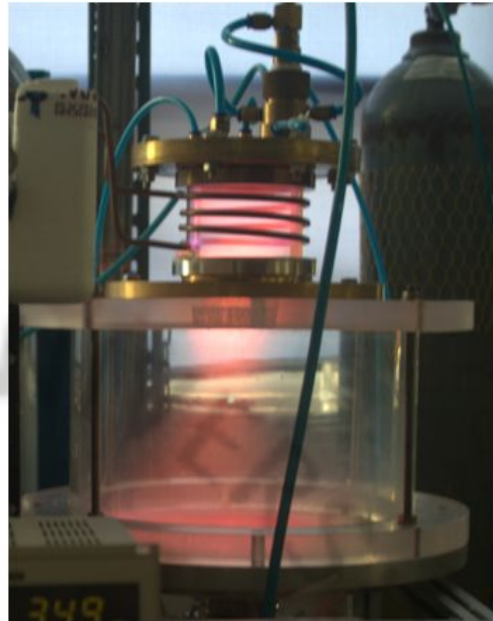


(d) RF: 1 kW, DC: 1 kW, P: 3 Torr

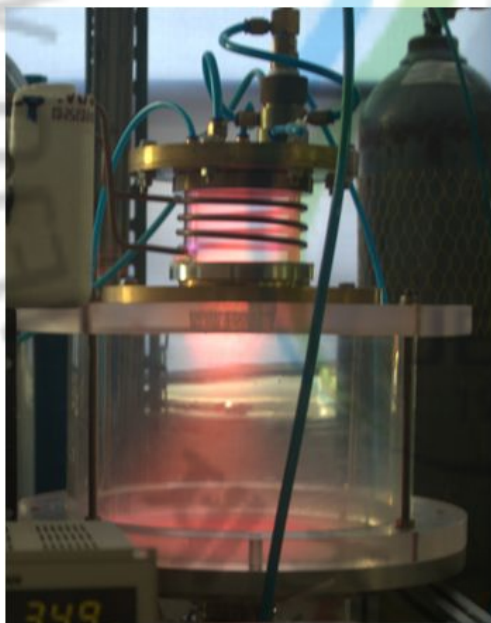
Fig. 34 Photographs of the RF and DC-RF hybrid plasma discharge.



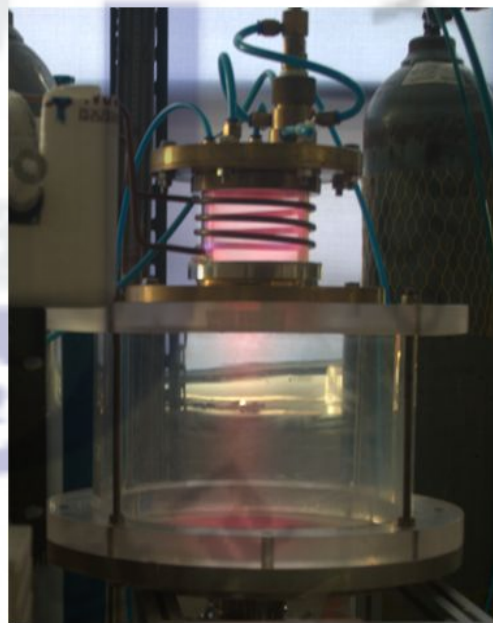
(a) RF: 800W, 2.5 Torr



(b) RF: 800W, 3.5 Torr



(c) RF: 800W, 4.9 Torr

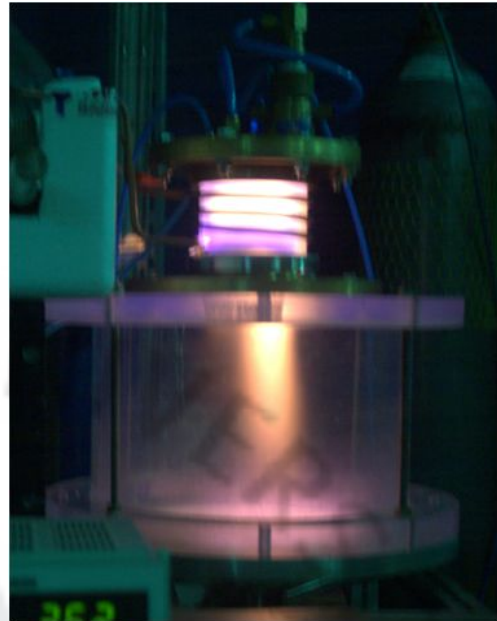


(d) RF: 800W, 7.3 Torr

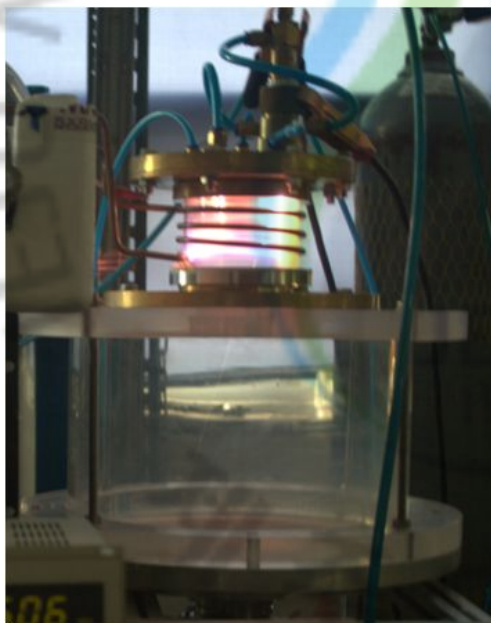
Fig. 35 Characteristics of the RF plasma discharge according to the pressure.



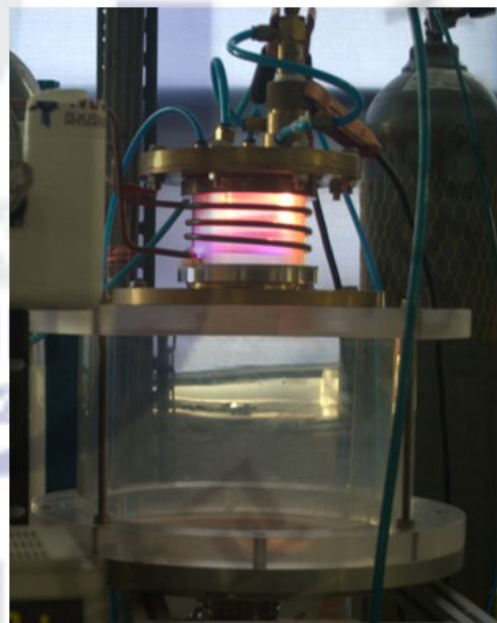
(a) RF: 800W, DC: 1 kW, P: 3.1 Torr



(b) RF: 800W, DC: 1 kW, P: 3.6 Torr



(c) RF: 800W, DC: 1 kW, P: 5.1 Torr



(d) RF: 800W, DC: 1 kW, P: 10.8 Torr

Fig. 36 Characteristics of the DC-RF plasma discharge according to the pressure.

2.2 Measurement of Plasma Parameter by Langmuir probe

Of all the ways to measure a plasma, the Langmuir probe is probably the simplest, since it consists of striking a wire into the plasma and measuring the current to it at various applied voltages. However, it is an intrusive, not remote, technique; and the "wire" must be carefully designed so as not to interfere with the plasma nor be destroyed by it.

The experimental arrangement is simple, requiring in addition to the probe, a scanning DC power supply(usually ± 100 V) and an X-Y recorder. A typical circuit diagram for the probe is shown in Fig. 37. X-Y recorder is possible to the oscilloscope and computer.

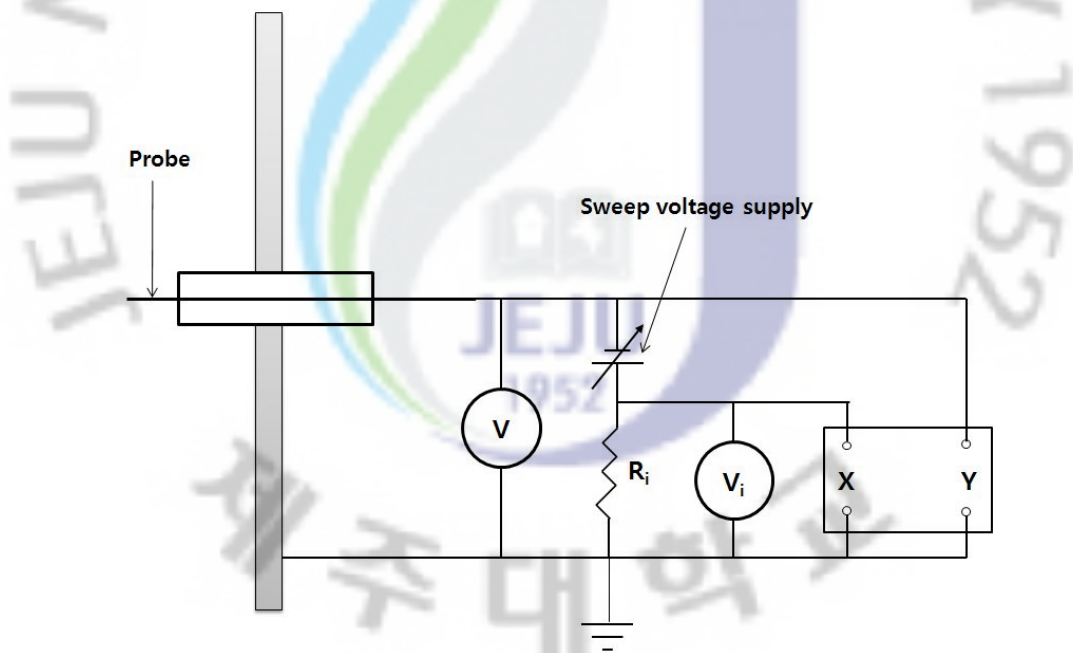


Fig. 37 Typical electrical circuit for single Langmuir probe.

1) Parts of the I-V curve

Let the plasma potential (space potential) be V_s , and the potential applied to the probe be V_p . If the chamber walls are metal and grounded, V_s is normally of the order of $5kTe$. When $V_p \gg V_s$, an electron current I_e is collected; the probe current is negative. When $V_p \ll V_s$, an ion current I_i is collected. It is customary to plot I-V curves with I_e positive and I_i negative. Such a plot is shown in Fig. 38. There are five main parts.

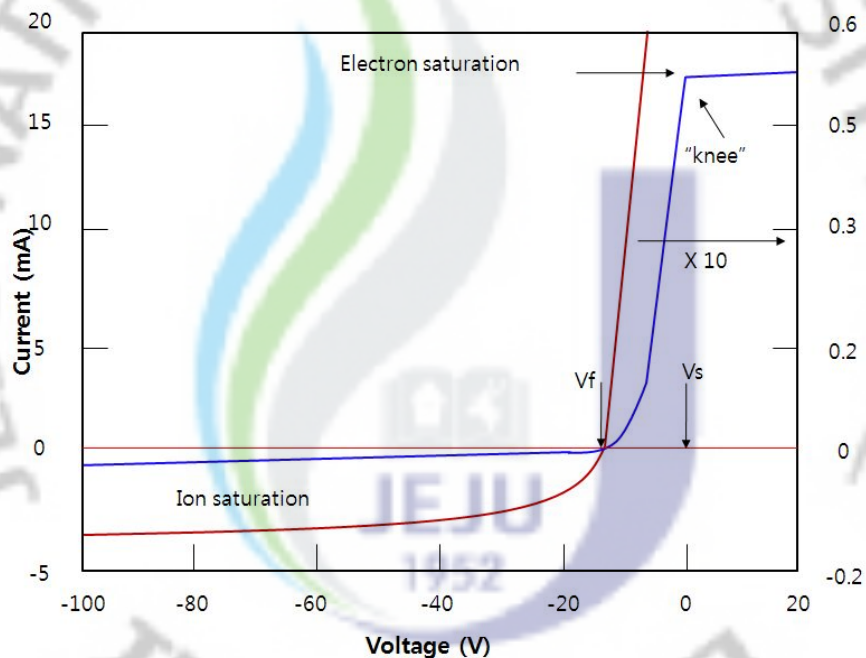


Fig. 38 An idealized I-V curve. The left curve is expanded 10 X to show the ion current.

The space potential V_s is near the "knee" of the curve. At the far left, where all the electrons have been repelled, we have the Ion saturation current, I_{sat} . The floating potential V_f , is where the ion and electron currents are equal, and the net current is zero.

2) Electron temperature

Electron energy distribution function (EEDF) is induced by a electron current. EEDF equation is expressed as following

$$f_e(E) = \frac{-4}{A_p e^2} \left(\frac{m_e (V_{plasma} - V)}{2e} \right)^{1/2} \frac{d^2 I_e(V)}{dV^2}$$

Here, unit of E is a eV and $f_e(E)$ is a $m^{-3}eV^{-1}$. If we assume that EEDF is a Maxwellian, Equation will be double integration. Such as potential function of a probe, electron current is found by plasma potential voltage.

$$I_e(V_{probe}) = I_{e,sat} \exp\left(\frac{-e(V_{plasma} - V_{probe})}{kT_e}\right)$$

$$\therefore T_e = -\frac{V_{plasma} - V_{probe}}{\ln I_{e,sat} - \ln I_e(V_{probe})} = -\frac{du}{d \ln I}$$

3) Plasma density

At the point of the ion saturation, plasma density can be measured exactly. Electron density is obtained by measuring a saturation current.

$$n_e = \left(\frac{4 I_{e,sat}}{e \pi dl} \right) \cdot \sqrt{\pi m_e / 8 k T_e} = 4 \times [10^{15} I_{e,sat} / (\pi dl \sqrt{T_e})] (m^{-3})$$

Here, $I_{e,sat}$ is a saturation current, dl is a diameter of probe.

4) Experimental set-up

To measure plasma parameters, wise probe system developed by "P&A Solutions" company was used. This is possible to measure electron temperature, density, ion flux. In these experiments, probe is modified suitable for DC-RF hybrid plasma system. Figure 39 shows a DC power supply for electric probe in the wise probe system. Figure 40 shows a modified Langmuir probe in the reaction chamber.



Fig. 39 DC power supply for electric probe.

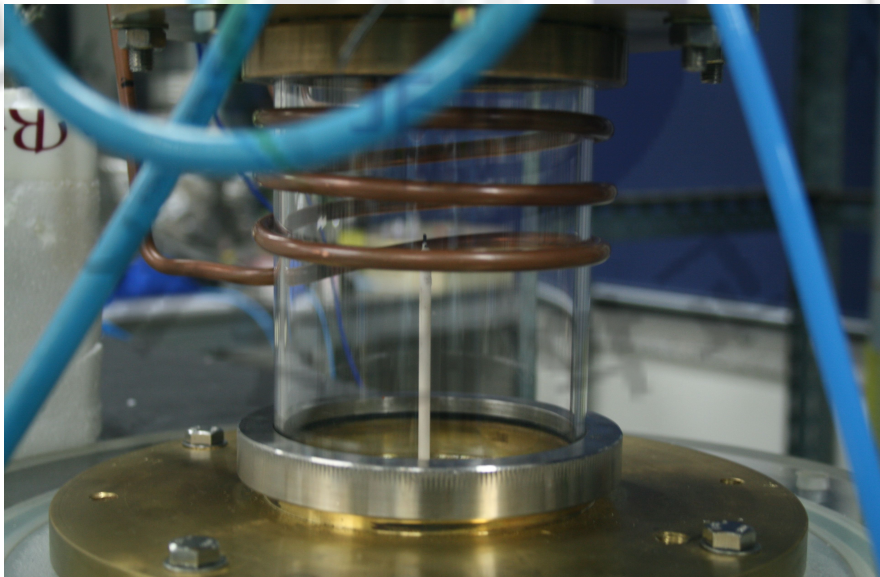


Fig. 40 Installed electric probe in the reaction chamber.

5) Measurements and Results

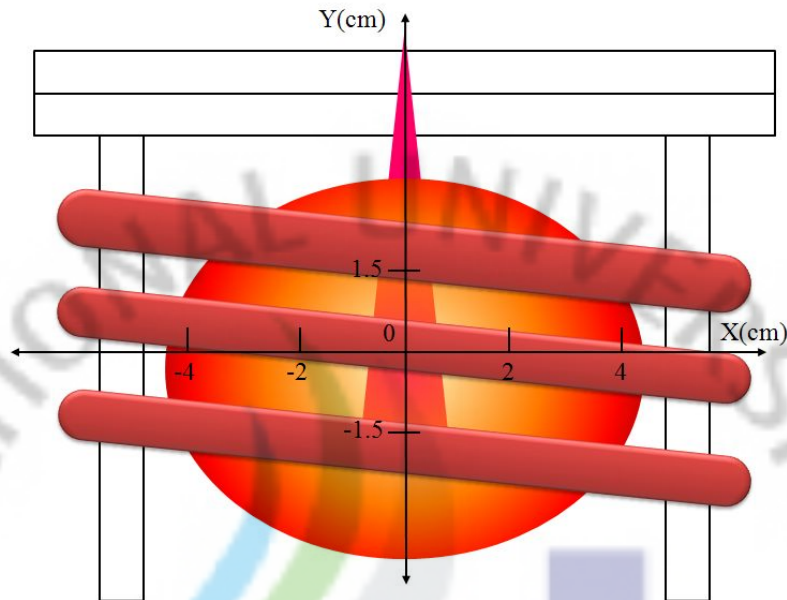


Fig. 41 Measurement points of the electric probe.

In these works, the electron temperature of DC-RF hybrid plasma was obtained by the Langmuir probe and compared to the electron temperature of the RF plasma. The measurement points were shown in fig. 41. The results of electron temperature were shown in Figs. 42-47, the electron temperature values were typically in the range 1–4 eV.



Fig. 42 Electron temperature distribution (vertical axis) of the DC-RF hybrid plasma at $x=0$.

Fig. 43 Electron temperature distribution (vertical axis) of the DC-RF hybrid plasma at $x=2$.



Fig. 44 Electron temperature distribution (vertical axis) of the DC-RF hybrid plasma at $x=4$.

Fig. 45 Electron temperature distribution (horizontal axis) of the DC-RF hybrid plasma at $y=1.5$.



Fig. 46 Electron temperature distribution (horizontal axis) of the DC-RF hybrid plasma at $y=0$.

Fig. 47 Electron temperature distribution (horizontal axis) of the DC-RF hybrid plasma at $y=-1.5$.

The results of plasma density were shown in Figs. 48 - 53. The plasma density was measured to compare RF plasma and DC-RF hybrid plasma. In case of RF plasma, plasma density is high at near the chamber wall more than center of the chamber, but plasma density is similar the center and wall of the chamber. Figure 48 shows plasma densities measured at only RF and DC-RF hybrid applied. The horizontal spatial distributions of the plasma density were shown in figs. 48 - 50, figures 51 - 52 shows vertical spatial distributions of the plasma density. The results of Langmuir probe measurement, we obtain a homogeneous plasma density is about 1×10^{10} #/cm³.




Fig. 48 Plasma density distribution (horizontal axis) of the DC-RF hybrid plasma at $y=0$.



Fig. 49 Plasma density distribution (horizontal axis) of the DC-RF hybrid plasma at $y=1.5$.

Fig. 50 Plasma density distribution (horizontal axis) of the DC-RF hybrid plasma at $y=-1.5$.



Fig. 51 Plasma density distribution (vertical axis) of the DC-RF hybrid plasma at $x=0$.

Fig. 52 Plasma density distribution (vertical axis) of the DC-RF hybrid plasma at $x=2$.



Fig. 53 Plasma density distribution (vertical axis) of the DC-RF hybrid plasma at $x=-2$.

2.3 Measurement of Optical Emission Spectroscopy

The most widely used methods for determining the plasma parameters are based on the optically thin emission of spectral lines. The determination of the electron density by the Stark broadening effect, as well as the measurement of temperature using the Boltzmann and Saha-Boltzmann equations require that the spectral lines used are optically thin. If this condition is not satisfied, that is, if the lines used for characterization suffer from self-absorption, their line profiles are saturated, showing distorted widths and areas that lead to wrong values of electron density and temperature. In this section, we will focus on the methods used to verify that the spectral lines are emitted in optically thin conditions.

Glow discharges (GD) are used in a large number of applications, ranging from the microelectronics industry, to the laser and light industry, the plasma display panel technology, and analytical chemistry. In the latter application, the material to be analyzed is used as the cathode of the glow discharge, which is sputter-bombarded by plasma species. The sputtered cathode atoms enter the plasma and can be ionized or excited, making the glow discharge useful in analytical chemistry as source for mass spectrometry and optical emission spectrometry. In practice, the coupling of a glow discharge with an optical spectrometer for GD-OES gives rise to optical emission spectra, i.e., intensities of spectral lines in a certain wavelength range.

In this measurement, we used a spectrometer of TM-VIS/NIR-CCD made by HAMAMATSU company. Its response range is from 340 to 1000 nm and wavelength reproducibility is ± 0.2 nm.

Table 4 Persistent Lines of Neutral Argon (Ar I)

Intensity	Wavelength(\AA)	$A_{ki}(10^8\text{s}^{-1})$	configuration	Term	J	Level(cm^{-1})
180	866.79997	3.14	$3p^6$ $3p^5(^2P^0_{1/2})3d$	1S $^2[3/2]^0$	0 1	0.000 115366.871
150	869.75411	0.35	$3p^6$ $3p^5(^2P^0_{1/2})5s$	1S $^2[1/2]^0$	0 1	0.000 114975.024
180	876.05767	2.69	$3p^6$ $3p^5(^2P^0_{1/2})3d$	1S $^2[3/2]^0$	0 1	0.000 114147.737
180	879.94656	0.77	$3p^6$ $3p^5(^2P^0_{1/2})5s$	1S $^2[3/2]^0$	0 1	0.000 113643.265
150	894.31013		$3p^6$ $3p^5(^2P^0_{3/2})3d$	1S $^2[1/2]^0$	0 1	0.000 111818.033
1000	1048.21987	5.32	$3p^6$ $3p^5(^2P^0_{1/2})4s$	1S $^2[1/2]^0$	0 1	0.000 95399.8329
500	1066.65980	1.32	$3p^6$ $3p^5(^2P^0_{3/2})4s$	1S $^2[3/2]^0$	0 1	0.000 93750.6031
300	6965.431	0.067	$3p^5(^2P^0_{3/2})4s$ $3p^5(^2P^0_{1/2})4p$	$^2[3/2]^0$ $^2[1/2]$	2 1	93143.7653 107496.4219
300	7067.218	0.0395	$3p^5(^2P^0_{3/2})4s$ $3p^5(^2P^0_{1/2})4p$	$^2[3/2]^0$ $^2[3/2]$	2 2	93143.7653 107289.7054
600	7503.869	0.472	$3p^5(^2P^0_{1/2})4s$ $3p^5(^2P^0_{1/2})4p$	$^2[1/2]^0$ $^2[1/2]$	1 0	95399.8329 108722.6247
700	7635.106	0.274	$3p^5(^2P^0_{3/2})4s$ $3p^5(^2P^0_{3/2})4p$	$^2[3/2]^0$ $^2[3/2]$	2 2	93143.7653 106237.5571
600	7948.176	0.196	$3p^5(^2P^0_{1/2})4s$ $3p^5(^2P^0_{1/2})4p$	$^2[1/2]^0$ $^2[3/2]$	0 1	94553.6705 106237.5571
600	8006.157	0.0490	$3p^5(^2P^0_{3/2})4s$ $3p^5(^2P^0_{3/2})4p$	$^2[3/2]^0$ $^2[3/2]$	1 2	93750.6031 106237.5571
700	8014.786	0.0928	$3p^5(^2P^0_{3/2})4s$ $3p^5(^2P^0_{3/2})4p$	$^2[3/2]^0$ $^2[5/2]$	2 2	93143.7653 105617.2753

Fig. 54 Argon plasma spectrum.

Spectra observations are an important step in the discharge investigation. Argon emission spectra are recorded over wavelength range (400 – 820) nm from the DC-RF hybrid plasma reaction chambers of the plasma source. The observations cover the whole experimental conditions, explored in the study (13.56 MHz; P=900, 1400 W; DC 1000 W; pressure=3 torr; plasma column radius R=45 mm). Line-of-sight integrated optical emission from the plasma is collected.

The spectra are clearly dominated by atomic Ar lines in the red/near-infrared spectral region (690 – 820) nm due to 4s – 4p transitions, as it is shown in Fig. 54. From 400 to 690 nm pronounced spectral lines are not detected. According to the observations, the contribution of the highly excited states from $3p^56s$, $3p^55p$ and $3p^54d$ configurations in the spectra is negligible. Ion lines are not detected in the

spectra. The contribution to the total emission power of the spectra corresponding to $4p - 5s$, $3d$ transition arrays (above 1000 nm) is not very important in our opinion, since their small energies and transition probabilities [41].

Spectra emitted from the driver and the plasma expansion regions of the source, in the spectral range (690 – 820) nm, are shown in Fig. 55 - first column and Fig. 56 - second column, respectively, obtained at applied power $P=(\text{RF only, RF and DC power})$ and at gas pressure values $p=3.2$ torr. The presented experimental data of argon spectra are shown for the spectrometer instrumental response. The observations indicate sensitivity of the emission spectra to the changes of the discharge operating conditions of the applying power.



Fig. 55 Optical emission spectrum of argon RF plasma.



Fig. 56 Optical emission spectrum of argon DC-RF hybrid plasma.

The shape of the spectral line profile is formed by several mechanisms which cause its broadening: apparatus effects, motion of the emitters, interactions between the emitting atoms and the other species in the plasma. Light intensity of plasma are shown in Fig. 55 and Fig. 56. Especially, Figure 56 data is spectrum of the DC-RF hybrid plasma.

2.4 Measurement of the Plasma gas temperature by IR Camera

Conventional infrared (IR) imaging might be a good choice for non-contact measurement and imaging of temperature. These cameras are used extensively in the petrochemical, chemical and power-generating sectors to protect personnel, reduce waste, contain costs and help operations to comply with environmental regulations. In this experiment, we used an IR camera to measure a plasma gas temperature. It is easy to find a gas temperature distribution visually. Clearly, the temperature of the DC-RF plasma is of importance for the performance of both system designs. On the one hand, the temperature of the wall should be as high as possible, resulting in less dissipation of energy from the plasma to the DC-RF plasma and in the end, leading to increased analyze signals. On the other hand, the lifetime of the DC-RF plasma system is limited by the quartz temperature during continuous operation. In addition, factors such as the composition of the analyzed sample, the matrix, and the type of solvent clearly influence the DC-RF plasma system.

Temperatures in plasma spectrochemistry are used mainly to describe the energies of the various species in the ICP and determined, e.g., via UV emission line intensities and laser scattering techniques. Other approaches to measure temperatures are based on thermocouples, pyrometers and Langmuir probes. Thermal imaging of analytical plasmas was employed, e.g., for the investigation of microwave fields inside a surfatron and a microwave plasma torch by means of thermally sensitive paper.

In this temperature measurement by IR camera, we used a T-20 IR camera made by FLIR company. A measurement range of the IR camera is from $-20\text{ }^{\circ}\text{C}$ to $360\text{ }^{\circ}\text{C}$, resolution is 240×180 pixel and accuracy is $\pm 2\text{ }^{\circ}\text{C}$.

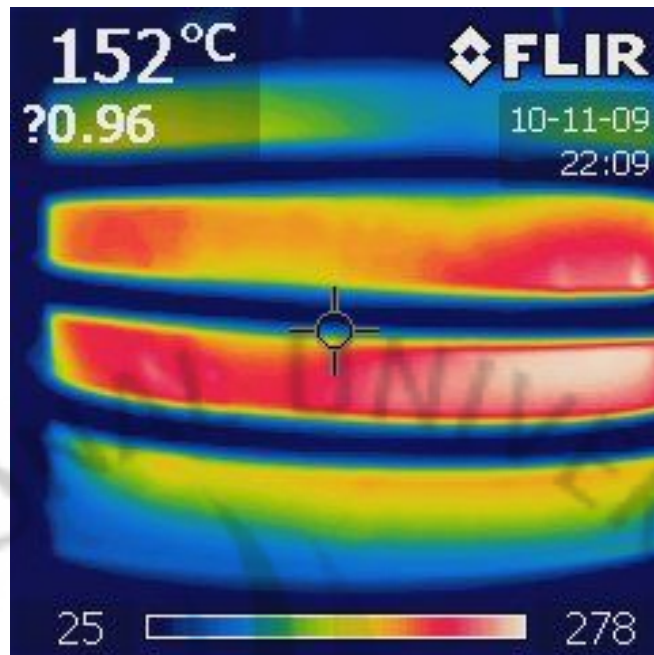


Fig. 57 IR camera measurement of DC-RF plasma (RF: 1 kW, DC: 0 kW).

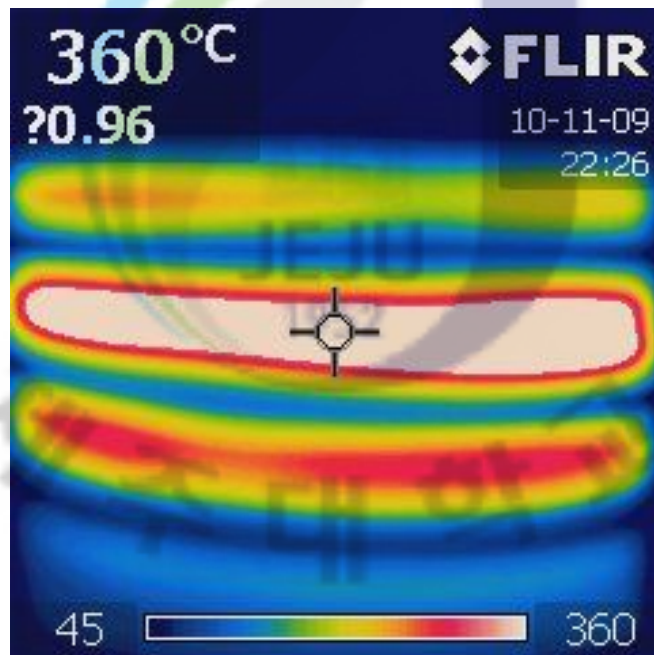


Fig. 58 IR camera measurement of DC-RF plasma (RF: 1 kW, DC: 1 kW).

Figure 57 and 58 show results of the IR measurements of DC-RF hybrid and RF plasma. In this experiments, plasma gas is used a argon that is easy to discharge and is necessary for protecting a cathode in the DC arc plasmatron.

Figure 57 shows a plasma gas temperature of RF plasma without DC power. Maximum temperature of the reaction chamber wall is about 280 °C and minium is about 150 °C in the plasma region. A temperature distribution of DC-RF hybrid plasma is shown in figure 58.



IV. Plasma Etching

Single-wafer plasma etching (PE) is an important process used in semiconductor manufacturing to selectively remove areas of thin films of compounds (e.g. amorphous silicon, silicon nitride, etc.) which are placed on substrates. In a PE process, the activation of the gases is achieved through impact with electrons and leads to the reacting species. The main advantages of plasma-assisted etching include directional selectivity of the reactions that take place on the surface of the wafer (etch anisotropy), reduced processing time and elimination of wet chemicals used in traditional etching processes. Even though the advantages of plasma etching are well known, a major issue which limits the widespread use of the PE process is the significant spatial non-uniformity of the etching rate. Such wet treatments are environmentally undesirable due to the large amount of chemicals used. So, dry cleaning such as plasma treatments becomes an alternative to solve those problems. However, low pressure plasma requires the use of a vacuum system, making it very expensive. The atmospheric pressure plasma without a vacuum system has a similar effect to low pressure plasma for the application of surface cleaning. Thus, the use of atmospheric pressure plasma not only decreases the processing cost but also increases the possibility of applying plasma system to electronic industries. Many types of atmospheric pressure plasma have been developed such as microwave, radio frequency (RF) plasma torch, dielectric barrier discharge, arc plasma torch, capacitively coupled atmospheric pressure plasma. Atmospheric pressure plasma operates with a high flow (\sim several m^3/h) of feed gas and a small amount of an additive, such as O_2 , Ar, or CF_4 .

Thermal plasmas (especially arc plasma) were extensively industrialized,

principally by aeronautic sector. Cold plasma technologies have been developed in the micro-electronics but their vacuum equipment limits their implantation.

Plasmas used in dry etching, thin film deposition and surface treatment for display or semiconductor industries are operating at low pressures in very costly due to the use of vacuum equipment and vacuum components. Subsequent wet processing is environmentally undesirable due to the use of the large amount of chemicals. Also, the usage of vacuum processing increases fabrication cost and decreases productivity. If stable atmospheric plasmas can be used, not only the decrease in processing costs but also the increase in productivity could be obtained. The development of the effective and simple source of plasma for the technologic processes of surface treatment remains one of the important issues, especially in the electronic industry.

With the purpose to increase the light collection and efficiency of silicon solar cell, the reflection of the front surface needs to be minimized. High-efficiency silicon solar cells need a textured front surface to reduce reflectance. Texturing of mono-crystalline silicon is usually done in alkaline solutions of wet-etching method.

Use of DC arc plasmatrons in welding, soldering, and cutting of metals is well known. A DC-arc plasmatron with high durability was reported to be a suitable device for etching silicon and photo-resist surfaces. A plasmatron can produce quite a dense plasma jet. It compared to other types of plasma source. However, it has some drawbacks, such as limited jet width and a small effective treatment area, because Plasmatron is known as point sources of plasma. The treating of large surfaces is coupling with technical difficulties. Clusters of electrode material evaporated by the arc may affect the processed surface, even though the contamination level of our plasmatron was only $\sim 10^{-10}$ g/C.

Recently, we obtained an etch rate as high as 30-60 $\mu\text{m}/\text{min}$ in silicon, although the etching was not uniform and had dimensions of only a few millimeters. Therefore, to address the two drawbacks mentioned above, we decided to use our plasmatron to construct a plasma source with a reactive region that was stretched in

one direction. In the previous work, we performed a plasma etching and texturing at a low pressure but to apply the industry, we have to develop an atmospheric and large area plasma processing. Plasma etching processes are qualified by the etching rate, uniformity of etching over the surface as well as among substrates, directionality of the etched pattern, and selectivity of the materials to be etched.

1. Plasma Etching by DC arc plasmatron at a low pressure

1.1 Experimental set-up

DC arc plasmatrons with cold thermo-chemical cathodes made of the hafnium or zirconium and cold nozzle anode (usually made of copper) seem to be the most suitable and well-recognized devices.

The A-plasmatron was used to activate the SF₆ gas. The A-plasmatron has low erosion rate of electrodes ensuring purity of the generated plasma necessary for technologic applications. To reduce the recombination rate of the activated gas particles inside a plasmatron and let them preserve their activated state outside, the whole device was installed outside of the vacuum chamber for vacuum processing. The experiment was provided on the mono-crystalline silicon wafer. The etching was carried out with plasma consisting of SF₆ (50 sccm) as a reactive etching gas with O₂ (3000 sccm) as a supporting gas and Argon (3000 sccm) as a cathode protecting gas. The sample was positioned in such a way that the plasma flow axis would coincide with the side facet of the silicon crystal.

An inert gas, argon, is supplied in a channel to protect the cathode. High-voltage, high-frequency AC is initially applied across the cathode and the anode to break the inter-electrode gap, and then a continuous DC voltage maintains the ignited arc. The technologic channel supplies the reactive gas to the argon-arc

region, where it interacts with the plasma and activates. The plasma then flows through the exit cap orifice and forms a jet.

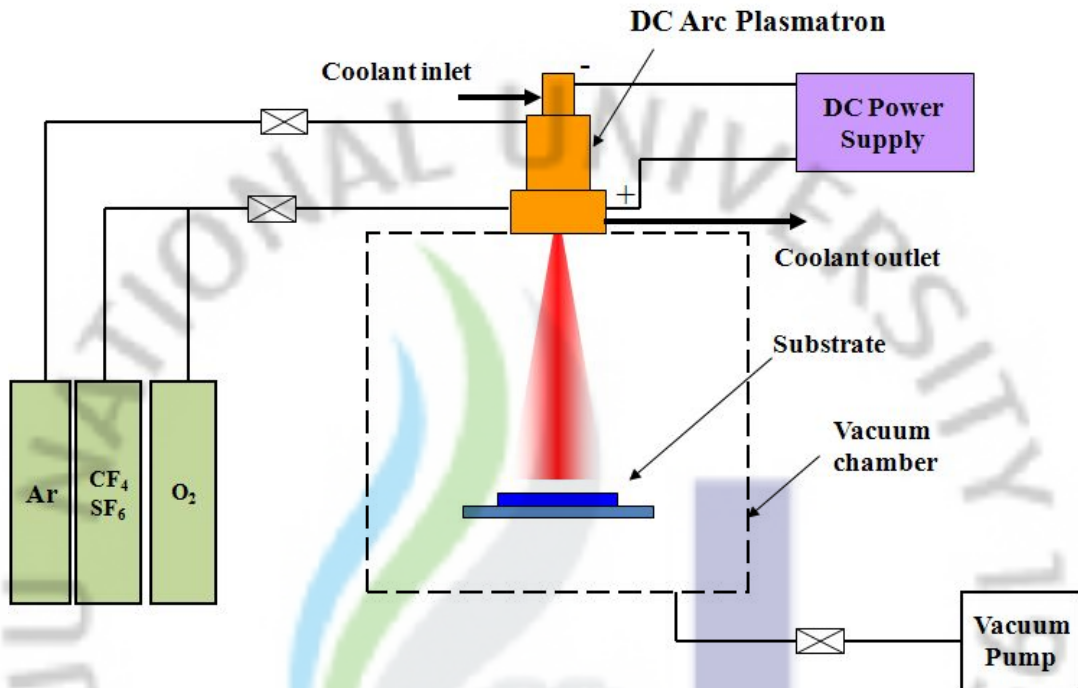


Fig. 59 Plasma etching and texturing system (low pressure)

Figure 59 shows the etching system of a silicon wafer at an atmospheric pressure. The distance from the plasmatron to the substrate was from 5 mm to 15 mm. The diameter of the clean silicon window was 14 mm, and the diameter of the cap was 32 mm.

Atmospheric pressure experiment, the substrate was laid at a distance of about 5 – 15 mm from the plasmatron exit; etching of mono-crystal silicon was carried out in SF₆ plasma and etch of the surface was measured. A TIG MICRO 350X rectifier pulse inverter was used as the DC power source operating in current mode for $I \leq 350A$. It is consolidated with a high frequency high voltage start-up Oscillator of

HF. The start button of the oscillator is united with normal close contacts connected to a voltmeter that monitors the arc voltage. This way of connection is necessary to protect the voltmeter against breakdown with high voltage from the oscillator at this point of arc excitation (usually the oscillator voltage reaches ~11 kV).

1.2 Results and discussion

Regarding drawback of surface processing by a plasmatron, we can mention the small size of treatment area, which is comparable to plasmatron exit cap orifice.

To obtain high efficiency and large area of the silicon substrate etching and texturing were one of the main aims of our experiment. In the previous work, we achieved etch rate of 30 – 50 $\mu\text{m}/\text{min}$ and area are about 10 mm at the plasmatron power of 1000 W and 10 tor pressure.

Table 5 Experimental condition of the etching process at low pressure.

Sample #	Ar (sccm)	O2 (sccm)	CF4 (sccm)	Voltage (V)	Current (A)	Pressure (Torr)
1	2,000	300	50	15	100	5
2		200				
3		100				
4		300				
5		200	30		50	
6		100				
7		300	50		50	
8		200				
9		300	30			
10		200				

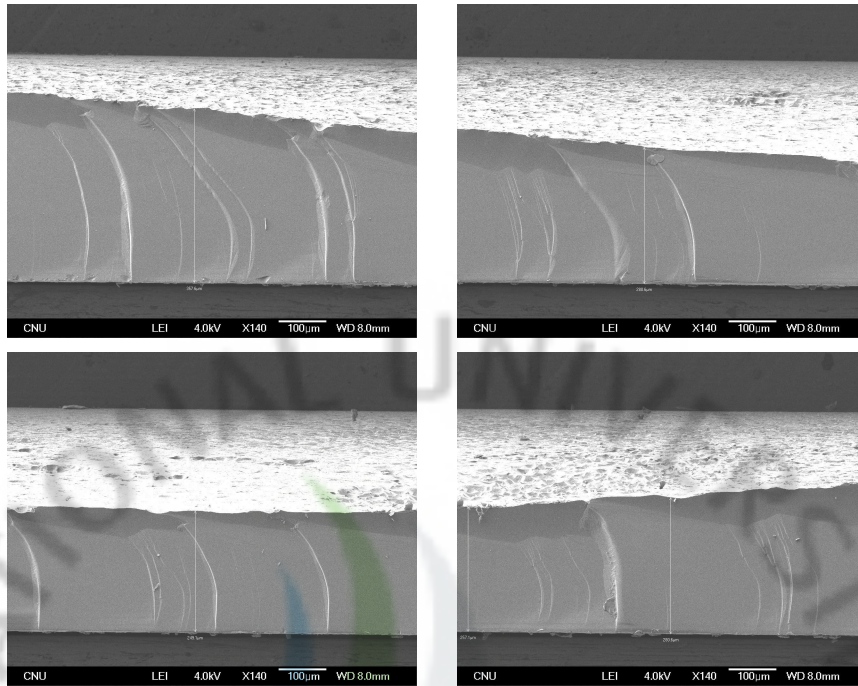


Fig. 60 SEM images (Ar: 2,000 sccm, O₂, 300 sccm, CF₄: 50 sccm, Voltage: 15V, Current: 100 A, P: 5 Torr).

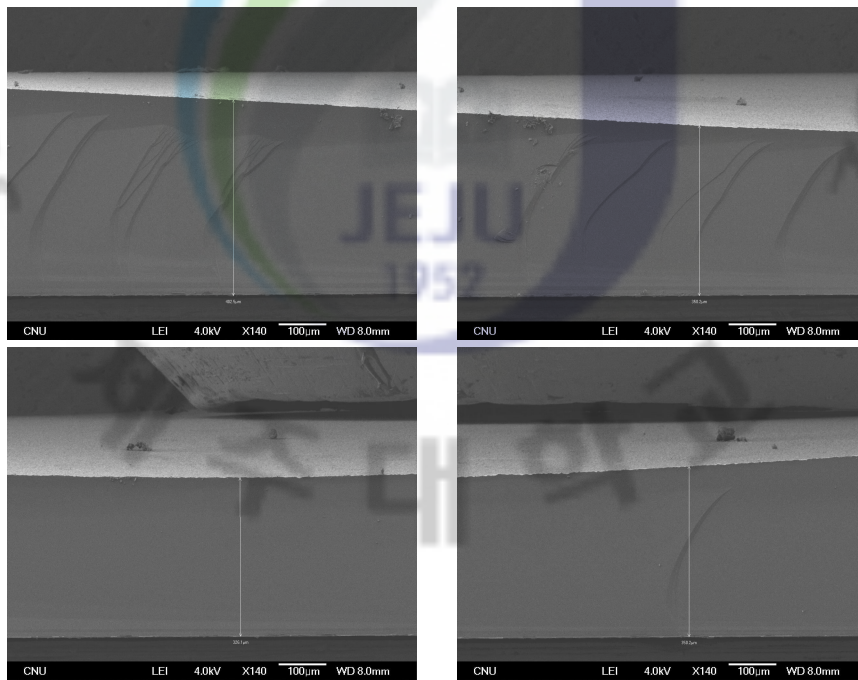


Fig. 61 SEM images (Ar: 2,000 sccm, O₂, 200 sccm, CF₄: 50 sccm, V: 15V, Current: 100 A, P: 5 Torr)

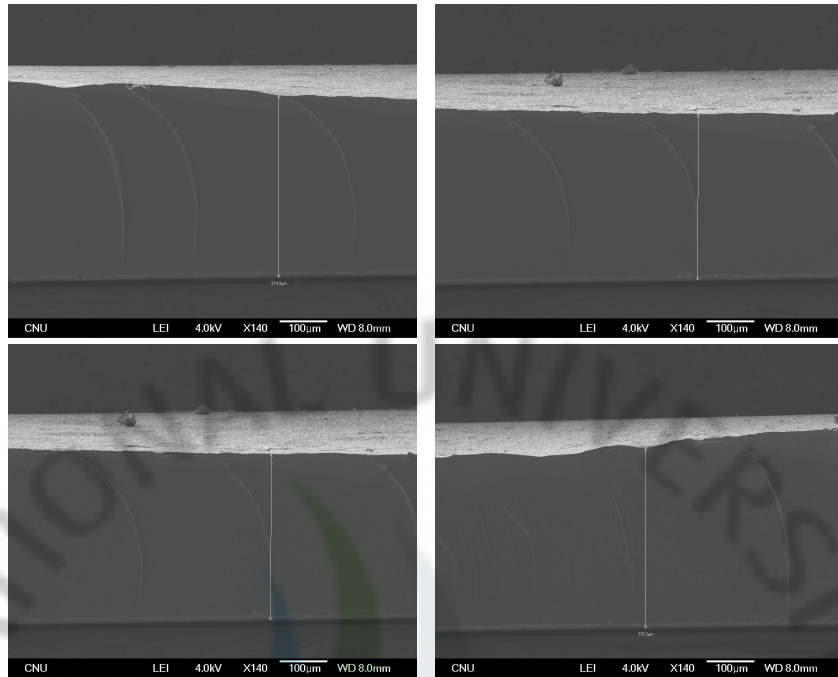


Fig. 62 SEM images (Ar: 2,000 sccm, O₂, 100 sccm, CF₄: 50 sccm, V: 15V, Current: 100 A, P: 5 Torr).

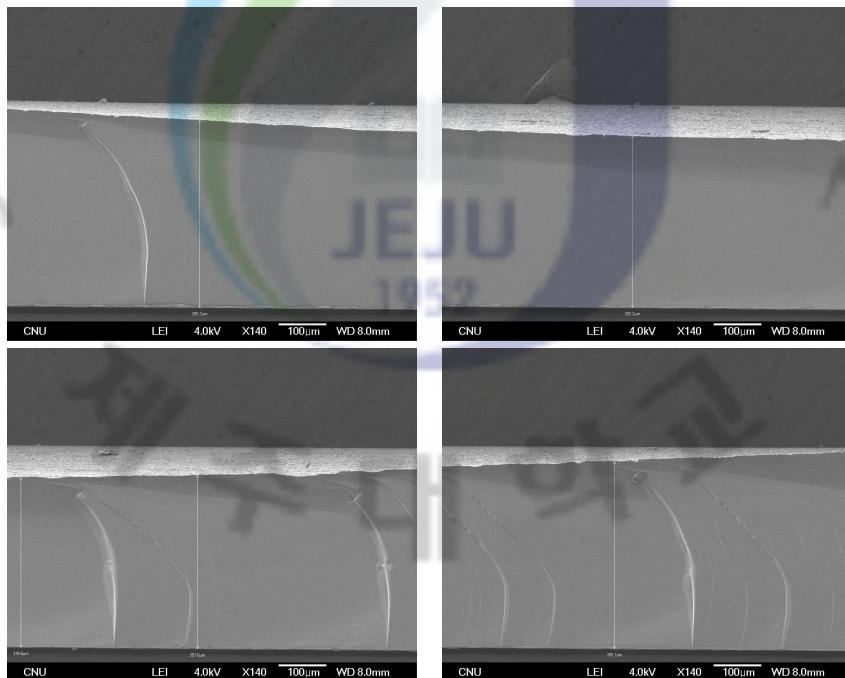


Fig. 63 SEM images (Ar: 2,000 sccm, O₂, 300 sccm, CF₄: 30 sccm, V: 15V, Current: 100 A, P: 5 Torr).

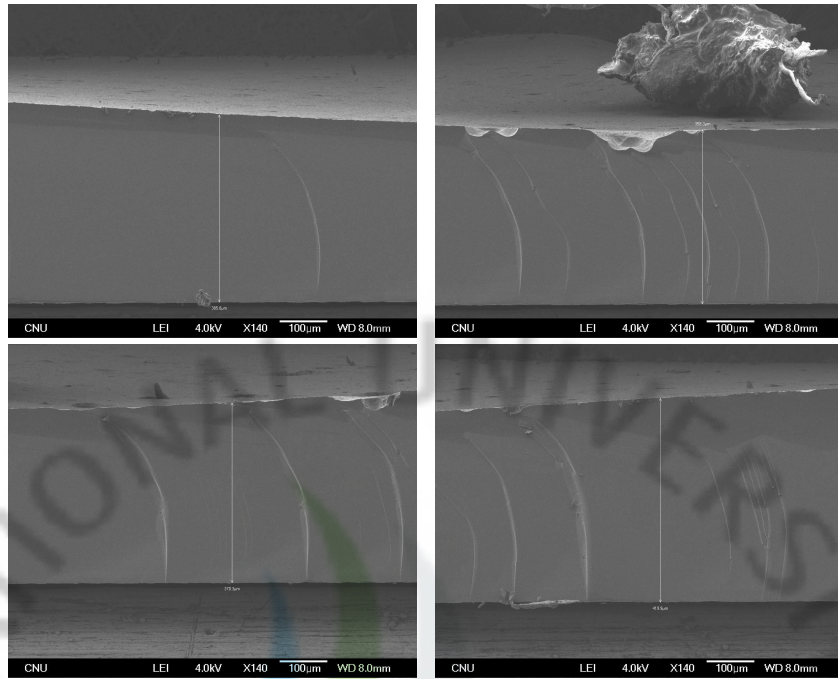


Fig. 64 SEM images (Ar: 2,000 sccm, O₂, 200 sccm, CF₄: 30 sccm, V: 15V, Current: 100 A, P: 5 Torr).

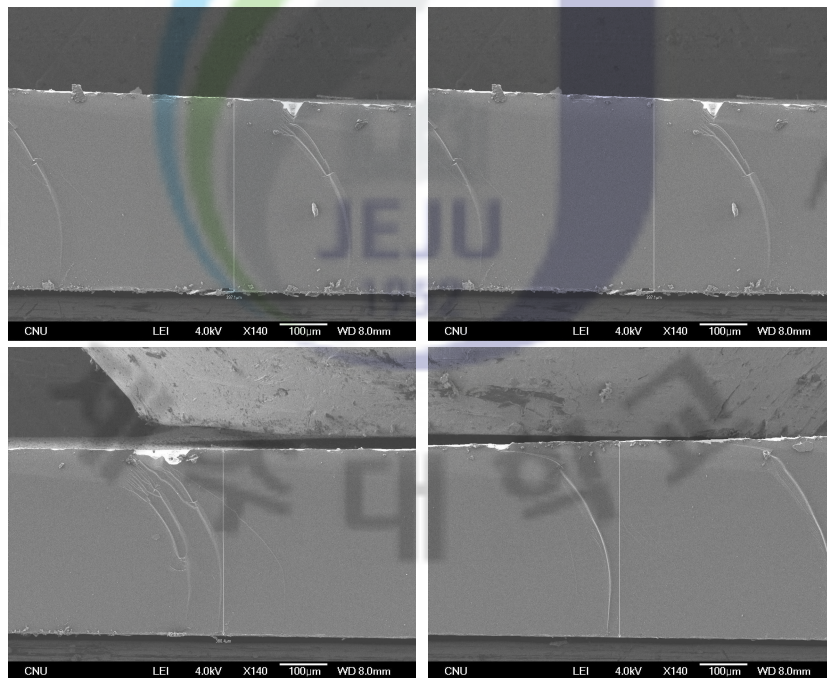


Fig. 65 SEM images (Ar: 2,000 sccm, O₂, 100 sccm, CF₄: 30 sccm, V: 15V, Current: 100 A, P: 5 Torr).

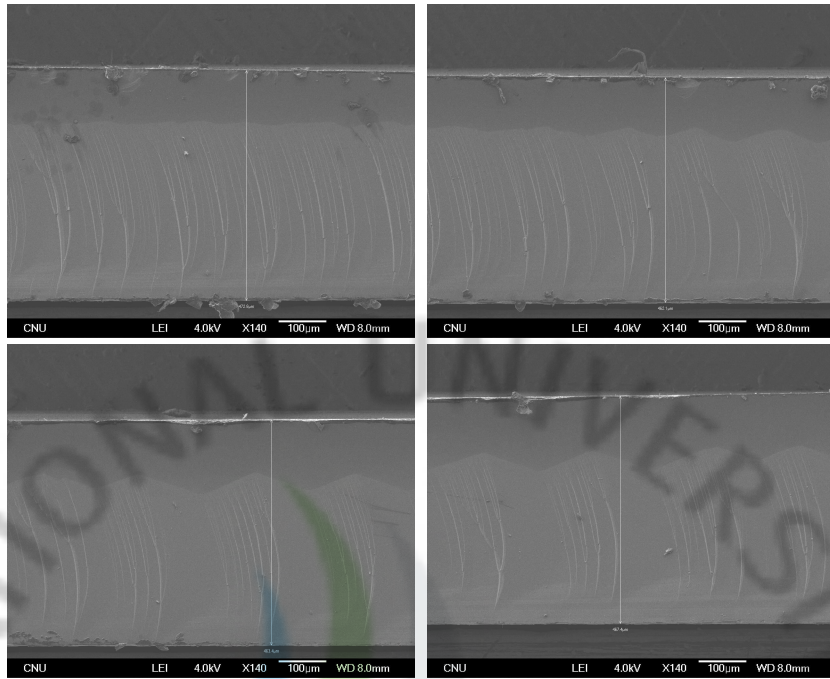


Fig. 66 SEM images (Ar: 2,000 sccm, O₂, 300 sccm, CF₄: 50 sccm, V: 15V, Current: 50 A, P: 5 Torr).



Fig. 67 SEM images (Ar: 2,000 sccm, O₂, 200 sccm, CF₄: 50 sccm, V: 15V, Current: 50 A, P: 5 Torr).

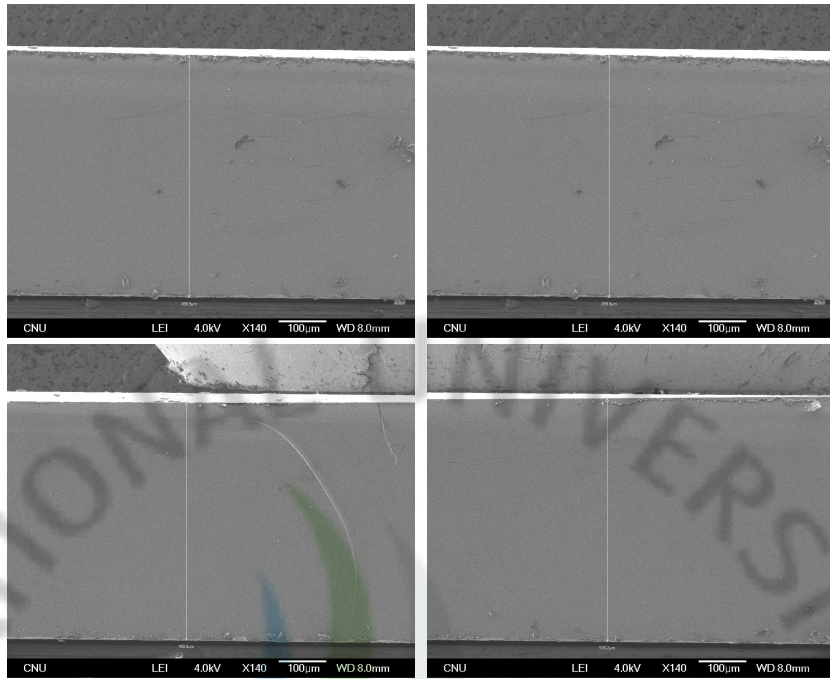


Fig. 68 SEM images (Ar: 2,000 sccm, O₂, 300 sccm, CF₄: 30 sccm, V: 15V, Current: 50 A, P: 5 Torr).

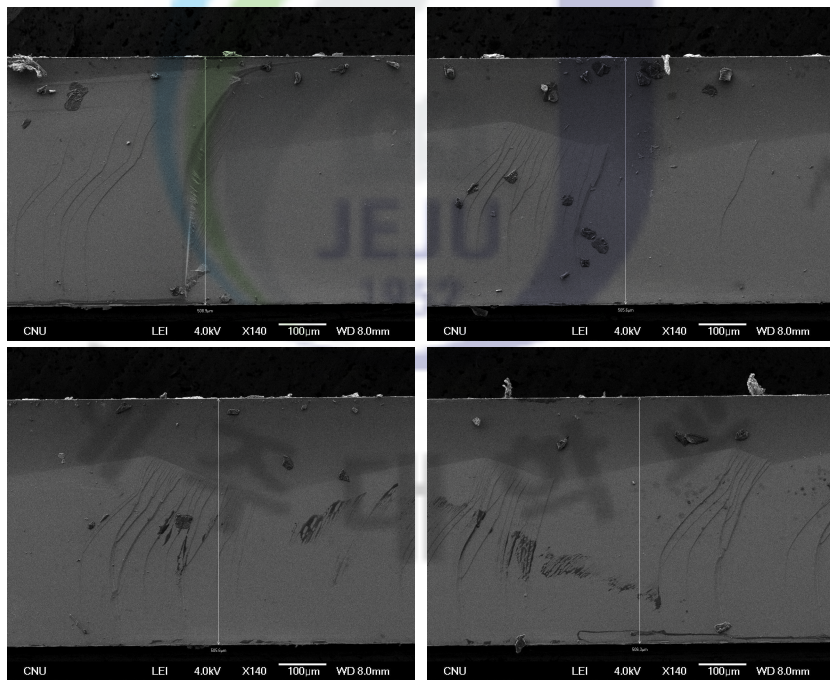


Fig. 69 SEM images (Ar: 2,000 sccm, O₂, 200 sccm, CF₄: 30 sccm, V: 15V, Current: 50 A, P: 5 Torr).

Fig. 70 Distribution of the Etching rates.

- (a) Ar: 2,000 sccm, O₂: 300 sccm, CF₄: 50 sccm, Current: 100 A
- (b) Ar: 2,000 sccm, O₂: 100 sccm, CF₄: 50 sccm, Current: 100 A
- (c) Ar: 2,000 sccm, O₂: 200 sccm, CF₄: 50 sccm, Current: 100 A

Figure 71 shows a distribution of the etching rates. In this results, effective etching area quite small about 8 ~ 10 mm. The optimal condition regarding oxygen flow rate is shown in fig. 72. The addition of oxygen to a fluorine-containing gas in a plasma significantly affects the etch rates of SiO₂ and Si, and the selectivity of the etching. A mechanism for this behavior is proposed, based on simultaneous etching and oxidation of the silicon surface by atomic F and O, respectively. When CF₄ or C₂F₆ is the source of F, the selective deposition of a fluorocarbon polymer on Si strongly affects the etching behavior. Figure 72 shows a result of etching rates according to DC arc plasmatron current.



Fig. 71 Results of the etching rates according to the oxygen flow rates.

Fig. 72 Results of the etching rates according to the CF_4 flow rates.



Fig. 73 Results of the etching rates according to the DC arc plasmatron current.

2. Plasma Etching by DC arc plasmatron at an atmospheric pressure

DC arc plasmatrons with cold thermo-chemical cathodes made of the hafnium or zirconium and cold nozzle anode (usually made of copper) seem to be the most suitable and well-recognized devices.

The A-plasmatron was used to activate the SF₆ gas. The A-plasmatron has low erosion rate of electrodes ensuring purity of the generated plasma necessary for technologic applications. To reduce the recombination rate of the activated gas particles inside a plasmatron and let them preserve their activated state outside, the whole device was installed outside of the vacuum chamber for vacuum processing. The experiment was provided on the mono-crystalline silicon wafer. The etching was carried out with plasma consisting of SF₆ (50 sccm) as a reactive etching gas with O₂ (300 sccm) as a supporting gas and Argon (3000 sccm) as a cathode protecting gas. The sample was positioned in such a way that the plasma flow axis would coincide with the side facet of the silicon crystal.

An inert gas, argon, is supplied in a channel to protect the cathode. High-voltage, high-frequency AC is initially applied across the cathode and the anode to break the inter-electrode gap, and then a continuous DC voltage maintains the ignited arc. The technologic channel supplies the reactive gas to the argon-arc region, where it interacts with the plasma and activates. The plasma then flows through the exit cap orifice and forms a jet.

2.1 Experimental set-up

A advantage of the DC arc plasmator is possible to apply an atmospheric for etching process. In this experiment, we want to know that it is possible to etching at an atmospheric pressure. Figure 30 shows the etching system of a silicon wafer at an atmospheric pressure. The distance from the plasmatron to the substrate was

from 5 mm to 15 mm. The diameter of the clean silicon window was 14 mm, and the diameter of the cap was 32 mm.

Atmospheric pressure experiment, the substrate was laid at a distance of about 5 – 15 mm from the plasmatron exit; etching of mono-crystal silicon was carried out in SF₆ plasma and etch of the surface was measured. A TIG MICRO 350X rectifier pulse inverter was used as the DC power source operating in current mode for $I \leq 350A$. It is consolidated with a high frequency high voltage start-up Oscillator of HF. The start button of the oscillator is united with normal close contacts connected to a voltmeter that monitors the arc voltage. This way of connection is necessary to protect the voltmeter against breakdown with high voltage from the oscillator at this point of arc excitation (usually the oscillator voltage reaches ~11 kV).

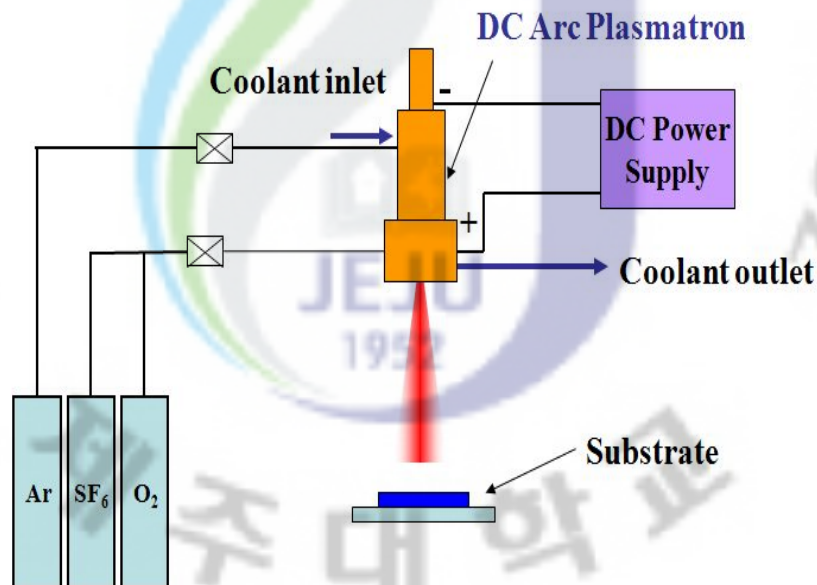


Fig. 74 Plasma etching and texturing system (atmospheric pressure).

2.2 Results and discussion

When a distance (from nozzle to substrate) is 5 mm, etch rate of maximum is about 500 $\mu\text{m}/\text{min}$. However, when a distance is 15 mm, etch rate of maximum is about 100 $\mu\text{m}/\text{min}$ but effective area is about 10 mm. This result means that plasmatron is possible to use a etching process, etching rate at an atmospheric pressure is higher than low pressure. Nevertheless, plasma mean-free-path is very short more than low pressure, the distance (from nozzle to substrate) is a very important parameter at atmospheric pressure process. To measure an etch rate and observe the textured silicon surface, field emission scanning electron microscope (FE-SEM) is used. The etch rate of the experiment was proportional to the distance.

Table 6 Experimental condition of the etching process at an atmospheric pressure.

Sample #	Ar (sccm)	SF ₆ (sccm)	O ₂ (sccm)	Distance (mm)	Current (A)
1	2,000	100	200	5	70
2		70			
3		50			
4		100		10	
5		50			
6		100			

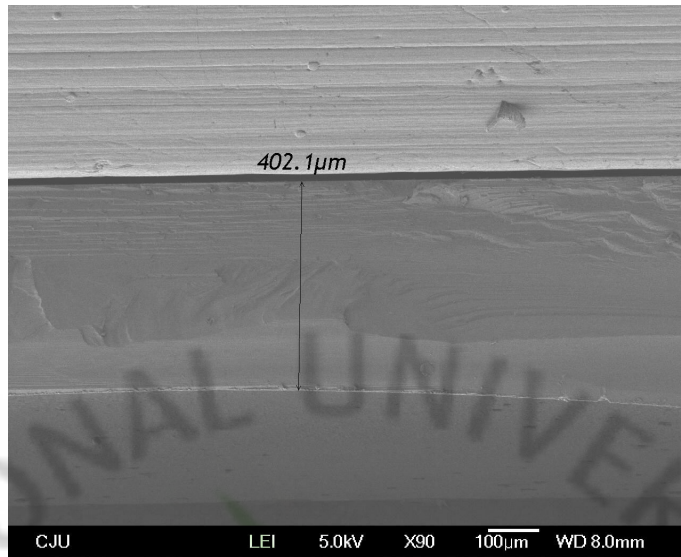


Fig. 75 A SEM image of atmospheric pressure etching (Ar: 2,000 sccm, SF₆: 100 sccm, O₂: 200 sccm, D: 5 mm, Current: 70A)

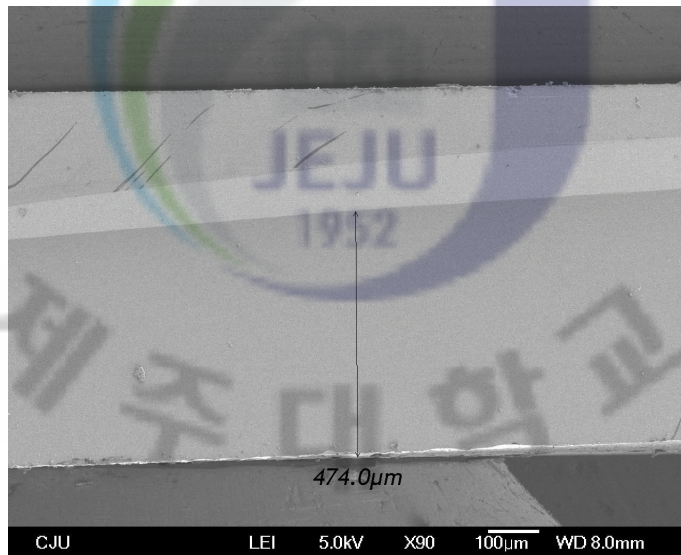


Fig. 76 A SEM image of atmospheric pressure etching (Ar: 2,000 sccm, SF₆: 70 sccm, O₂: 200 sccm, D: 5 mm, Current: 70A)

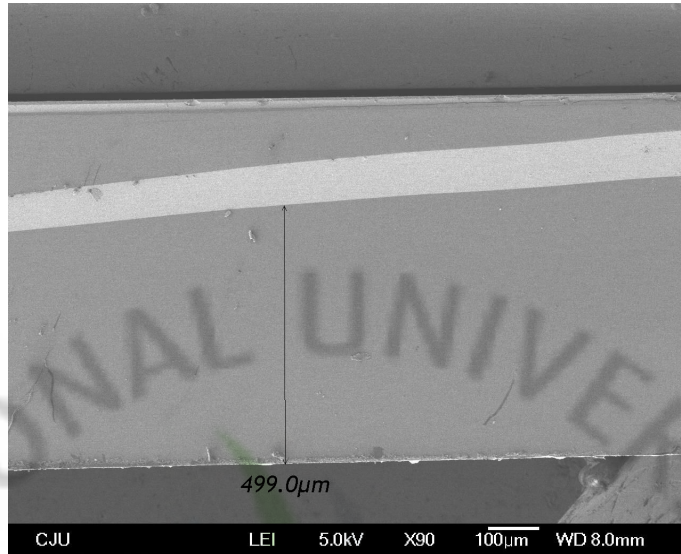


Fig. 77 A SEM image of atmospheric pressure etching (Ar: 2,000 sccm, SF₆: 50 sccm, O₂: 200 sccm, D: 5 mm, Current: 70A)



Fig. 78 A SEM image of atmospheric pressure etching (Ar: 2,000 sccm, SF₆: 100 sccm, O₂: 200 sccm, D: 10 mm, Current: 70A)



Fig. 79 A SEM image of atmospheric pressure etching (Ar: 2,000 sccm, SF₆: 50 sccm, O₂: 200 sccm, D: 10 mm, Current: 70A)

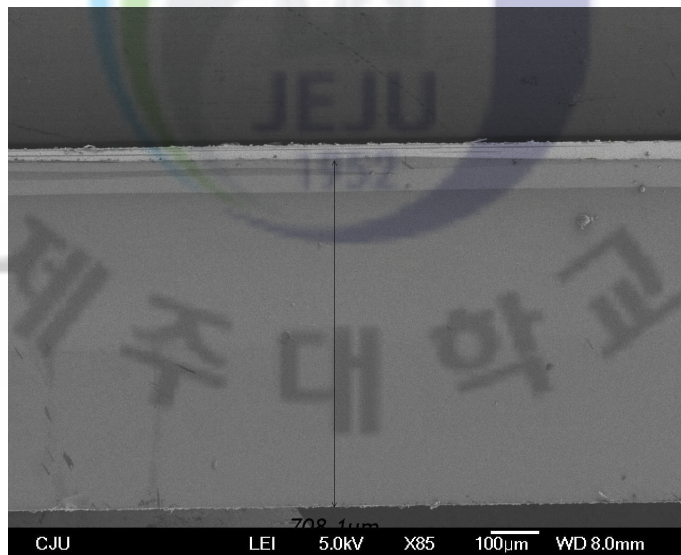


Fig. 80 A SEM image of atmospheric pressure etching (Ar: 2,000 sccm, SF₆: 100 sccm, O₂: 200 sccm, D: 15 mm, Current: 70A)

3. Plasma etching by DC-RF hybrid system

3.1 Experimental set-up

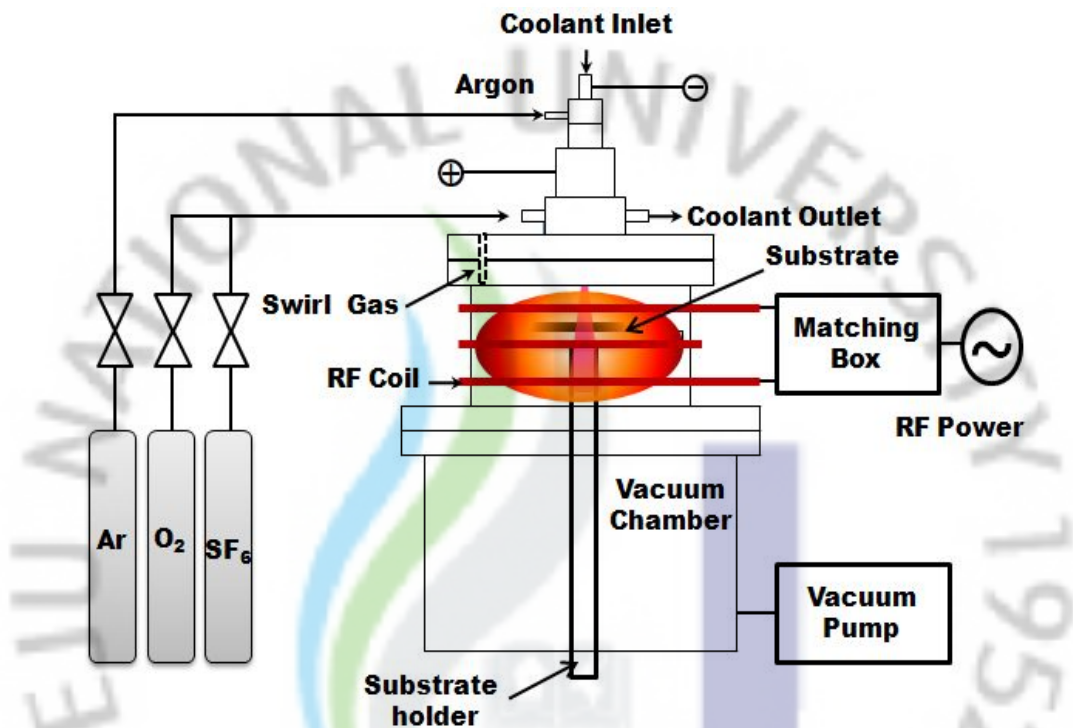


Fig. 81 RF-DC hybrid plasma experimental set-up.

3.2 Results

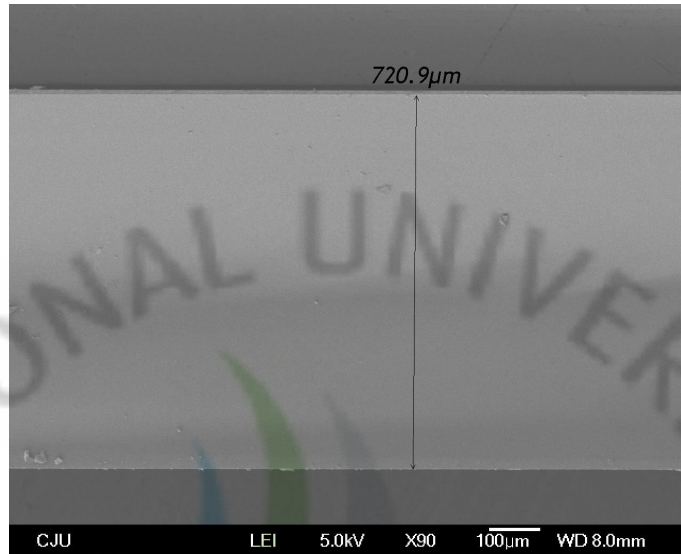


Fig. 82 A SEM image by the DC-RF hybrid plasma.

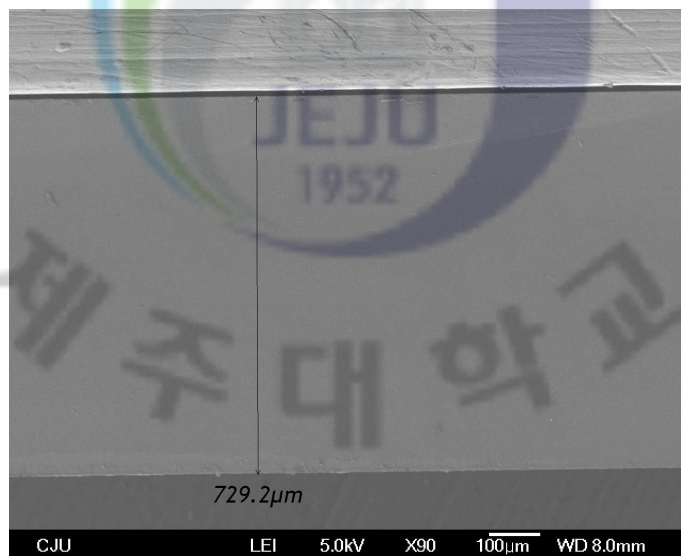


Fig. 83 A SEM image by the RF plasma.

VI. Plasma Texturing for the Solar Cell

Silicon appears to be almost the ideal PV material; it is abundant, non-toxic, and industrially effective. Although the use of amorphous silicon solar cells is growing rapidly, the crystalline silicon (c-Si) wafer is still the main trend of today's rapidly growing photovoltaic (PV) industry. Module sales have increased 30-40% per year over the last decade, with steadily increasing energy conversion efficiencies that now range from 14% to 20%. Texturing is used to reduce the light reflectance of the silicon surface, increase light trapping, and increase the short circuit current and the efficiency of solar cells. Random pyramid formation on the surface of (100) c-Si is an effective way of reducing the reflectivity at the front surface of c-Si solar cells [42]. Surface texturing reduces the reflection losses and causes oblique coupling of light into silicon. The reflection of the front surface needs to be minimized if the light collection and conversion efficiency of silicon solar cells is to be increased. This surface pattern can be created by different techniques: plasma and chemical etching. The PV industry is searching for new techniques to reduce the chemical consumption in industrial solar cell processing. The texturing of monocrystalline silicon is normally performed in alkaline solutions by using a wet etching method [43]. In microelectronics and photo-voltaic, the most widely used anisotropic etching solution is a low concentration (usually less than 5%) potassium hydroxide (KOH) solution in water with the addition of isopropyl alcohol (IPA) [44]. Recently, simple and low-cost techniques have been developed to solve the problems occurring during anisotropic texturing of a mc-Si wafer [45]. It is difficult to find a cheap way to texture the surface of such thin single-crystalline layers because pyramid pattern formation via an isotropic etch requires tens of microns of

material consumption. There are several successful works that have shown the capability of texturing the silicon with minimal material consumption and anti-reflection properties as good as those obtained from conventional texturing methods. Texturing (111) silicon surface with 1–5 nm thick material consumption was demonstrated [46].

The development of an effective and simple source of plasma for technological processing of surface treatments is an important issue, particularly in the electronics industry. Many techniques for silicon texturing have been examined. Some focused on the use of reactive ion etching (RIE), either in conjunction with a mask to achieve large, regular features or without a mask to produce a much smaller and more random texture [47, 48]. Other approaches have been based on isotropic wet acidic etching. These methods produce a lower reflectivity surface than the standard alkaline damage-removal etching currently used in the industry, but they have some disadvantages. For an example, the RIE system is very complex and expensive, and wet etching use toxic chemicals. On the other hand, the DC arc plasmatron is simple to use and the system price is inexpensive [49]. The use of DC arc plasmatrons in welding, soldering, and cutting of metals is well known. Among them, arc plasmatrons with cold thermochemical cathodes made from hafnium or zirconium and with cold nozzle anodes (normally made from copper) appear to be the most suitable and well-recognized devices. A high durability DC arc plasmatron was used to etch silicon monocrystalline wafers at low pressures or atmospheric pressures. Owing to the very low plasmatron anode erosion rate ($\sim 10^{-10}$ g/C), the plasma obtained is almost spectrally clean, which has potential applications in the electronics industry [50-53].

In this study, texturing experiments were performed with a DC arc plasmatron to decrease the reflectivity index of silicon substrates. High-efficiency etching of silicon

substrates is one of the main aims of the experiment. An etch rate of 30–0 $\mu\text{m}/\text{min}$ was achieved at a plasmatron powers from 1000 to 1500 W and pressures from 1 to 5 mbar. The addition of oxygen (5-15%) to the etching gas altered the plasma chemistry and increased the etch rate by approximately three times. Nevertheless, the total amount of the gas mixture supplied to the plasmatron play a role only at low flow rates whereas the etch rate remain of relatively constant in the range of 0.2–0 l/min .. One of the important tasks is to develop an inexpensive new-age silicon based solar cells.

1. Experimental Set-up

The A-type plasmatron (of axial type, Fig. 85) was used to activate the CF_4 and SF_6 gas. The A-plasmatron has a low erosion rate of the electrodes, ensuring the necessary purity of the plasma generated for technologic applications.

In the plasmatron, the arc is ignited in the space between the tungsten cathode and copper anode filled with argon. Most of the power is inputted in the gas in the argon part of the arc. After passing the anode orifice, argon is mixed with cool technologic gas.

A TIG MICRO 350X rectifier pulse inverter was used as the DC power source operating in current mode for $I \leq 350\text{A}$. It is consolidated with a high frequency high voltage startup oscillator of HF. The start button of the oscillator is united with the normal close contacts connected to a voltmeter that monitors the arc voltage. This way of connection is necessary to protect the voltmeter from breakdown with the high voltage from the oscillator at this point of arc excitation (usually the oscillator voltage reaches $\sim 11\text{ kV}$). Texturing with crystalline silicon in

CF₄ and SF₆ plasma was performed as an example of the plasma-chemical process. Field emission scanning electron microscopy (FE-SEM) was used to observe the textured silicon surface. A UV/VIS/NIR spectrophotometer (Shimadzu Corporation and its model no. is UV-3150) was used to measure the reflectance. The wavelength of the device ranged from 190 - 3200 nm, the photometric accuracy was +/- 0.002 Abs. and the resolution was < 0.1 nm.

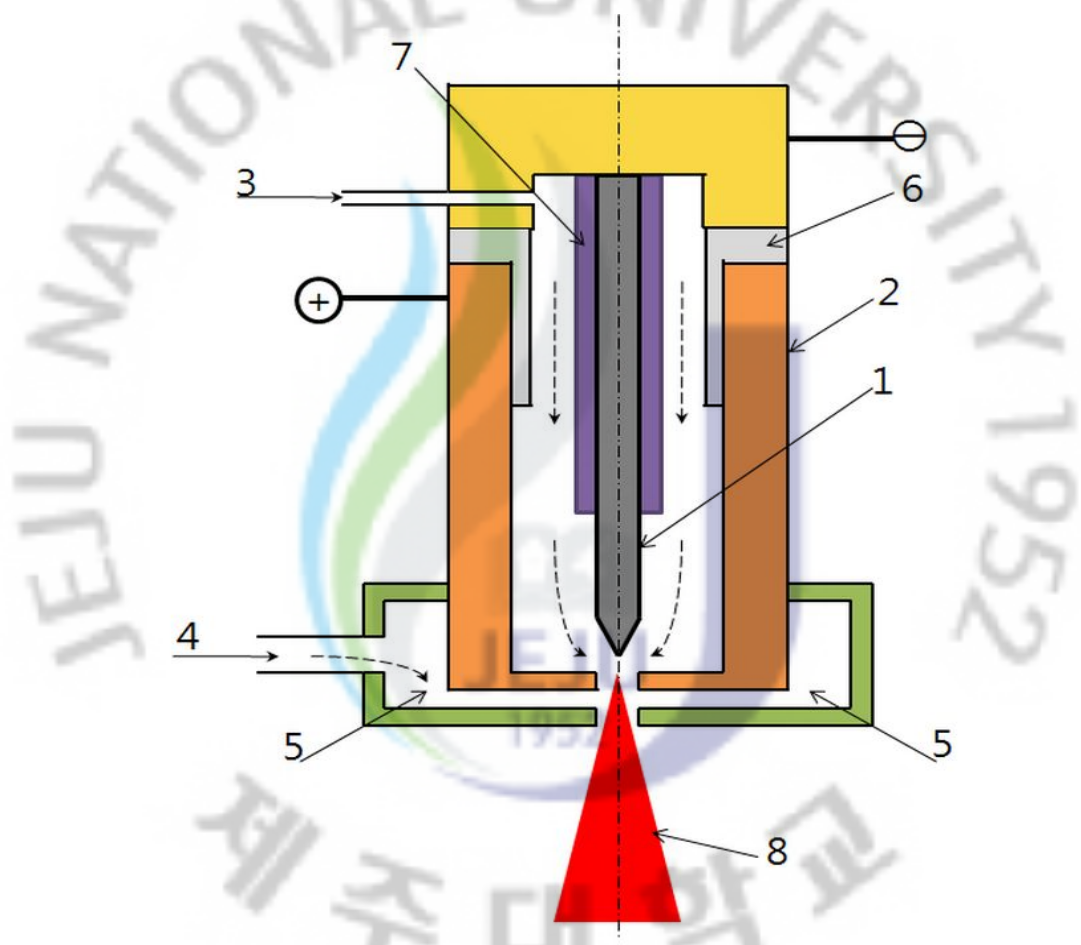


Fig. 84 A schematic diagram of the A-type plasmatron: (1) cathode, (2) anode, (3) argon supply, (4) technologic channel; (5) technologic gas supply, (6) electric insulator; (7) ceramic material; (8) resulting plasma flow.

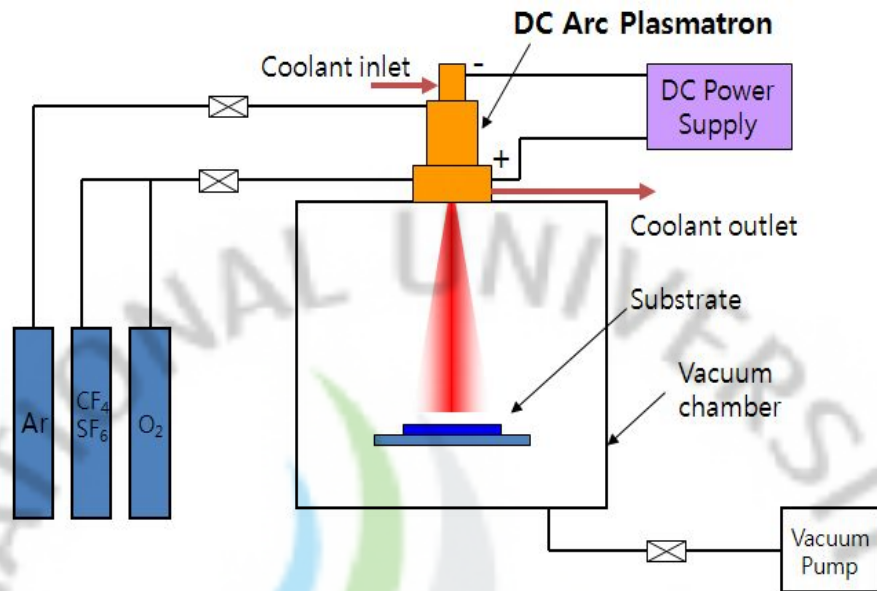
1.1 Plasma texturing at a low pressure (5 Torr)

Initially, in this vacuum experiment, the substrate was fixed at a distance of approximately 72 mm from the plasmatron exit. Texturing of mono-crystal silicon was carried out in CF_4 plasma and the surface texture was measured. Texturing is affected by the current (plasma power), CF_4 flow rate, O_2 flow rate, and pressure. Figure 86 shows a schematic diagram of the texturing experiment. The arc power was varied from 500 to 1500 W. In the vacuum state experiments, the entire device was installed with the vacuum chamber to reduce the recombination rate of activated gas particles inside the plasmatron and allow them to preserve their state outside.

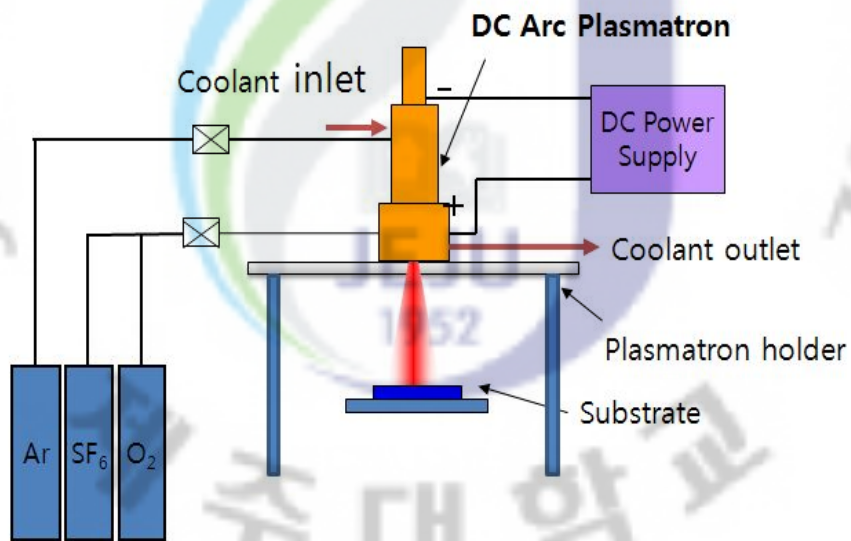
Texturing was carried out with plasma consisting of CF_4 (50-150 sccm) as the reactive etching gas with oxygen as the supporting gas at flow rates ranging from 300–500 sccm and argon (3000 sccm) as the cathode protecting gas. The system pressure was 5 Torr continuously. The sample was positioned in such a way that the plasma flow axis would coincide with the side facet of the silicon crystal. Figure 87 shows a picture of the operating DC arc plasmatron at low pressure.

1.2 Plasma texturing at an atmospheric pressure

The texturing experiment was performed on a single-crystalline silicon wafer and amorphous silicon. Texturing was carried out with plasma consisting of SF_6 (50-100 sccm) as the reactive etching gas with oxygen as a supporting gas at flow rates ranging from 300–500 sccm and argon (3000 sccm.) as the cathode protecting gas. The sample was positioned in a similar manner to the vacuum experiment. Figure 87 is shows a photograph of the DC arc plasmatron operating at an atmospheric pressure without vacuum chamber and vacuum pump.



(a)



(b)

Fig. 85 A diagram of the DC arc plasmatron processing system : (a) low pressure, (b) atmospheric pressure.

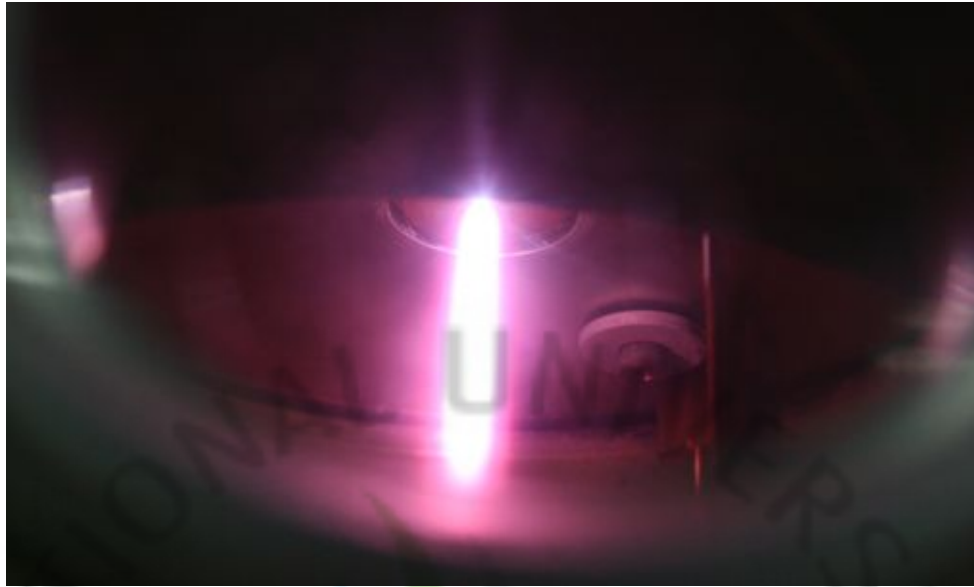


Fig. 86 A picture of the DC arc plasmatron operation at low pressure (3-5mbar).

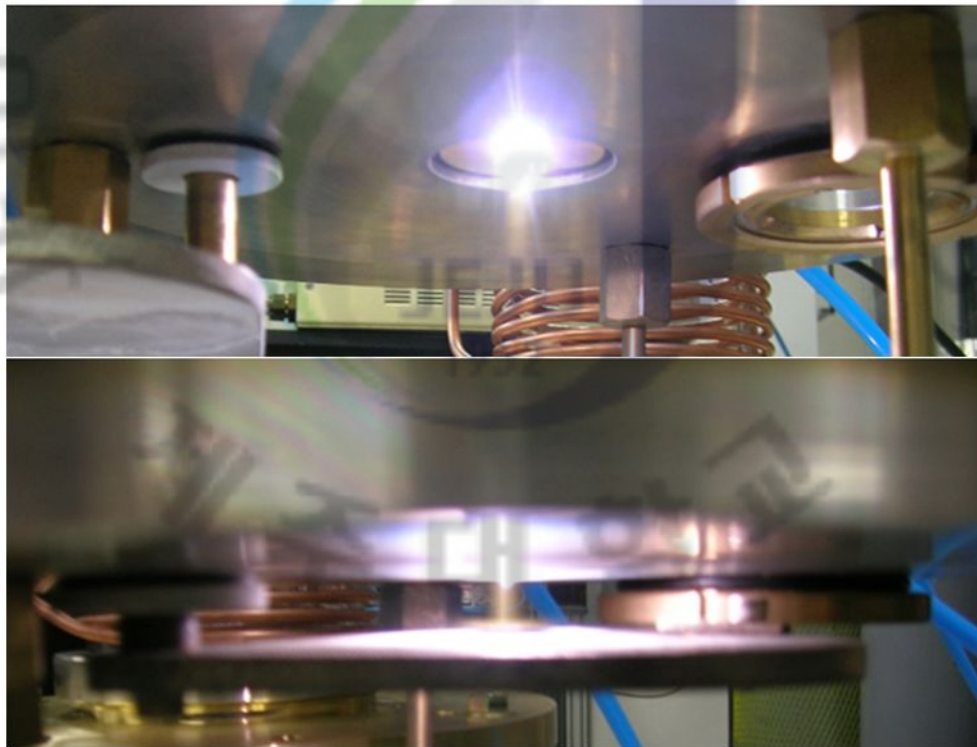


Fig. 87 Images of the DC arc plasmatron operating at atmospheric pressure.

2. Results and Discussion

2.1 Results

Figure 89 shows SEM images of the textured single crystalline silicon surface at a low pressure (5 Torr). A DC arc plasmatron current of 50 and 100 A was supplied at 3-5 mbar. When the supplied current was 50 A, the pyramid shape was sharper and the angle was lower than that observed at 100 A.

Surface texturing was more effective at a plasmatron current of the 70 A. The lower power allowed the formation of a sharper structure with considerable peaks (Fig. 89a). Increasing the plasmatron current to 100A led to disorder of the substrate structure (Fig. 89b) and decreased the surface reflectivity. Figure 90 shows results of the single crystalline silicon texturing surface by a plasmatron current with an oxygen (500 sccm), SF₆ (100 sccm) and argon (3000 sccm) at atmospheric pressure. These results show an effect of the operation current. When the operation current is 100 A, Si surface was textured with a distinct pyramid shape. Figure 91 shows the texturing results of the single crystalline silicon wafer surface according to the processing time. It is easy to understand a plasma texturing procedure of the DC arc plasmatron and find an optimal processing time. It was not until processing time was 30 second pyramid shape was textured perfectly. The optimal processing time was a 30 second in these results. The SEM image of the crystalline silicon surface textured with a oxygen concentration was shown in figure 92. Figure 93 shows the texturing results of amorphous silicon with a DC arc plasmatron at atmospheric pressure to investigate a texturing effect. As shown in figure 93, texturing effect was appeared to the amorphous silicon surface also.

Figure 94 shows the difference with the pyramid angle of the vacuum processing and atmospheric pressure processing. When a single-crystalline silicon surface was textured in a vacuum, the pyramid angle was approximately 50° to 60°, whereas it

ranged from 75° to 90° when textured at atmospheric pressure. A DC arc plasmatron has different characteristic between atmospheric pressure and low pressure (vacuum) on the mean free path. Plasma flume of a DC arc plasmatron is less than 20 mm at atmospheric pressure, but plasma flume of a DC arc plasmatron is over 100 mm at low pressure. Therefore, length of the pyramid shape is long and texturing angle is a small more than atmospheric pressure processing.

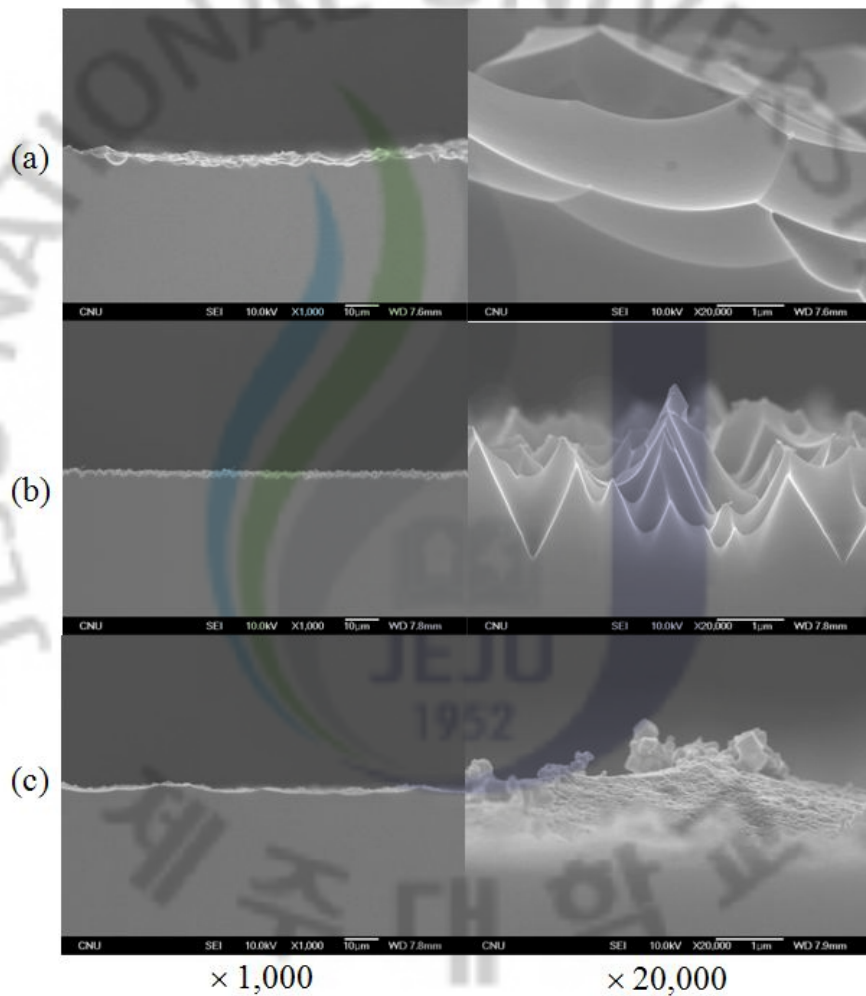
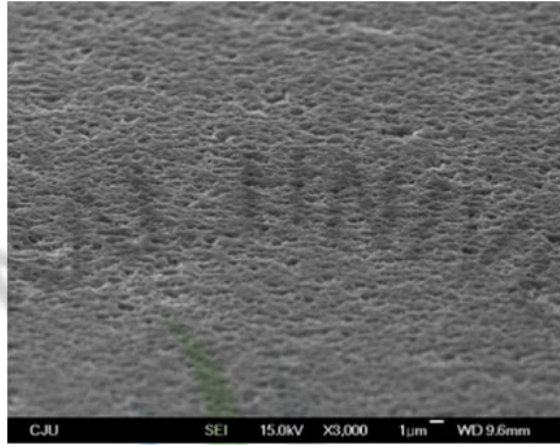
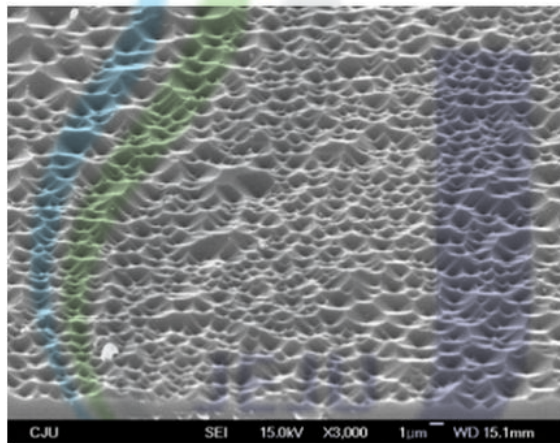


Fig. 88 SEM image of the single crystalline silicon surface textured at low pressure (3-5mbar, $V=14V$, $D=72mm$, $CF_4=100$ sccm, $Ar=2,000$ sccm, $O_2=500$ sccm, $V=14V$, $D=72mm$, $CF_4=100$ sccm, $Ar=2,000$ sccm, $O_2=500$ sccm): (a) $I=100$ A, (b) $I=70$ A, (c) 50 A.

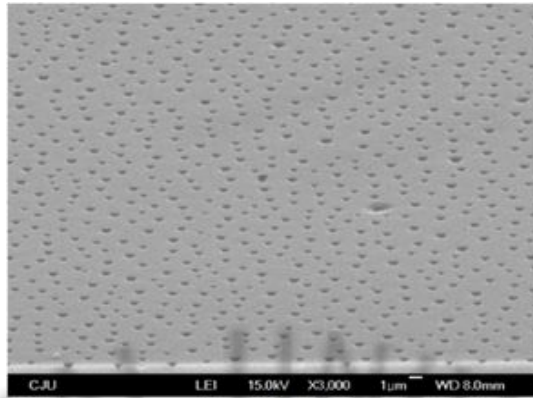


(a) 70 A

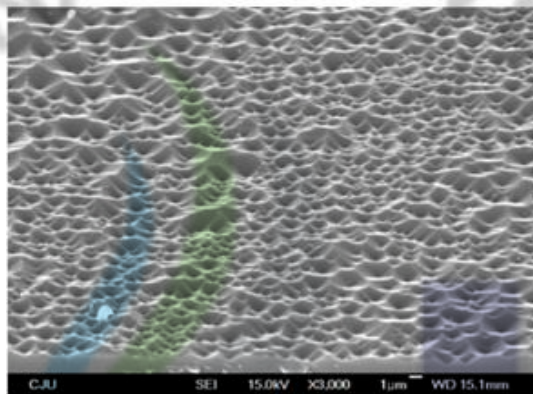


(b) 100 A

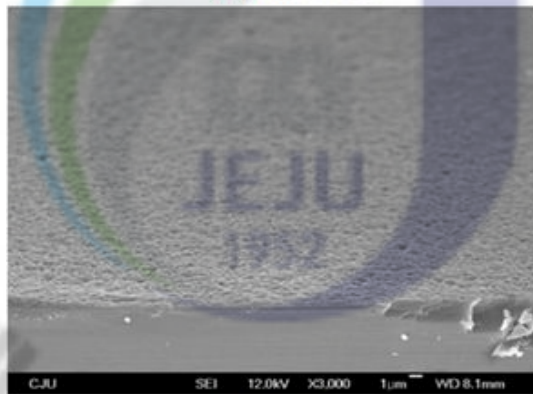
Fig. 89 SEM image of the single crystalline silicon surface textured with a dc arc plasmatron current (Ar: 3000 sccm, SF₆:100 sccm, O₂:500 sccm, Pressure: 760torr): (a) 70A, (b) 100A.



(a) 10 sec.

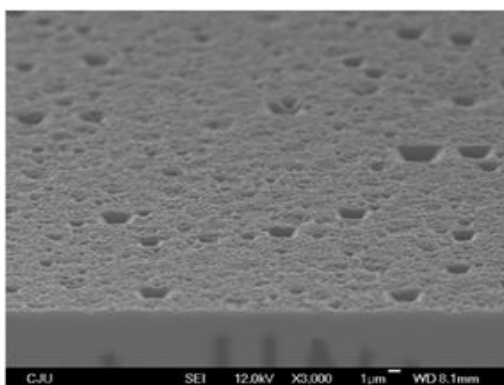


(b) 30 sec.

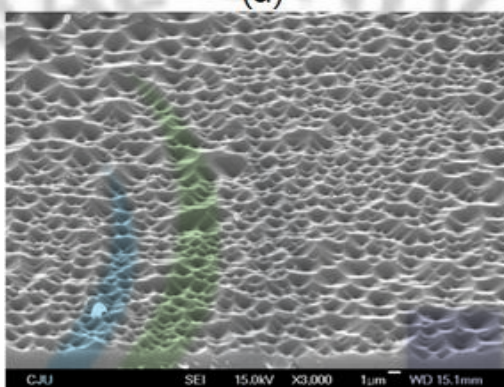


(c) 60 sec.

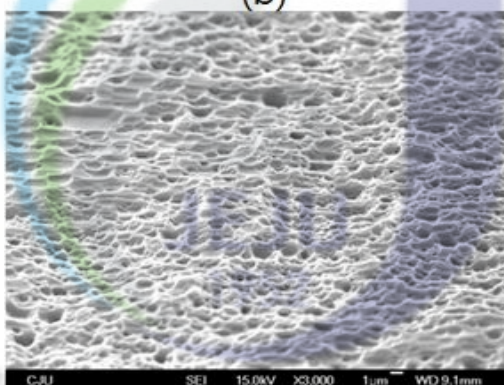
Fig. 90. SEM image of the mc-silicon surface textured at different processing times (Ar : 3000 sccm, SF6:100sccm, O2: 500sccm, Current: 100A, Pressure: 760torr): (a) 10 sec. (b) 30 sec. (c) 60 sec.



(a)

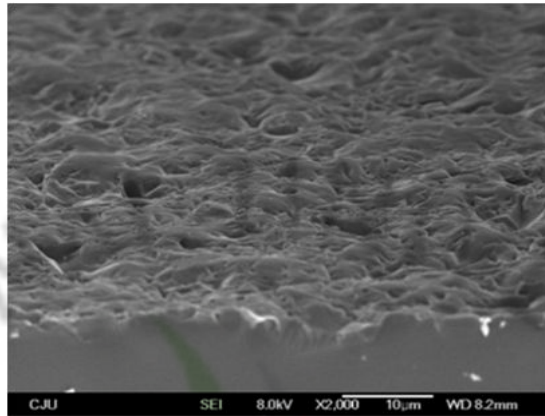


(b)

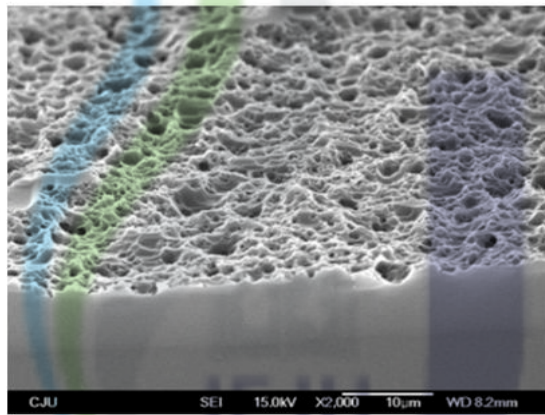


(c)

Fig. 91 SEM image of the single crystalline silicon surface textured with a oxygen concentrations (Ar : 3000 sccm, SF₆: 100 sccm, Current: 100A, Pressue: 760torr): (a) 5%, (b) 10%, (c) 15%.

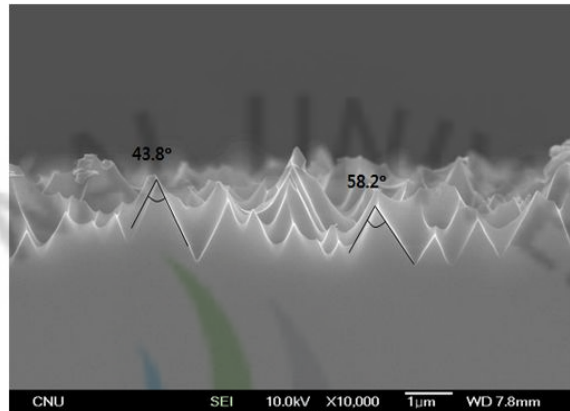


(a)

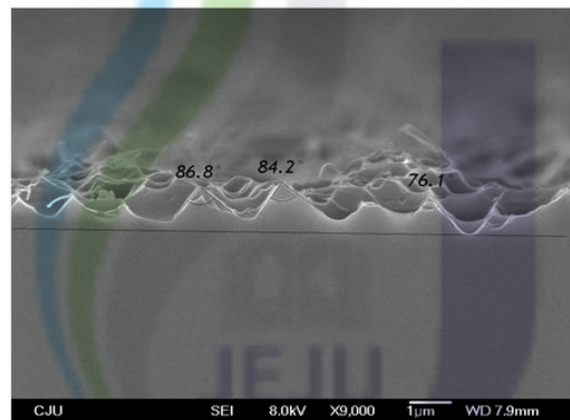


(b)

Fig. 92 SEM image of the textured amorphous silicon surface: (a) Bare silicon, (b) textured silicon by DC arc plasmatron (Ar: 3000 sccm, SF6: 100 sccm, O2: 500 sccm, Current: 100A, Pressue: 760 torr).



(a)



(b)

Fig. 93 SEM image of the pyramid angle to compare low and atmospheric pressure : (a) low pressure (5 torr), (b) atmospheric pressure (760 torr).

As shown in figures 95, 96 and 97, the pyramid angle is related to the reflectance. The reflectance also decreased with increasing pyramid angle. Figure 95 and 96 shows results of the reflectance textured silicon surface by the DC arc plasmatron at low pressure (5 Torr) and atmospheric pressure. The flow rate of the argon and oxygen were 3,000 and 500. When texturing experiments were performed at vacuum, we used etching gas of the CF_4 . A reflectance of the bare silicon surface was approximately 40-60%. The reflectance was approximately 3-5% and 5-10% when the treatment was performed at 5 Torr and atmospheric pressure, respectively.

Figure 97 shows the effect of the oxygen concentration in the gas. Increasing the oxygen concentration in the working gas resulted in the formation of a porous structure instead of a narrow shape. The reflectance was lower when the O_2 concentrations were 10 %.

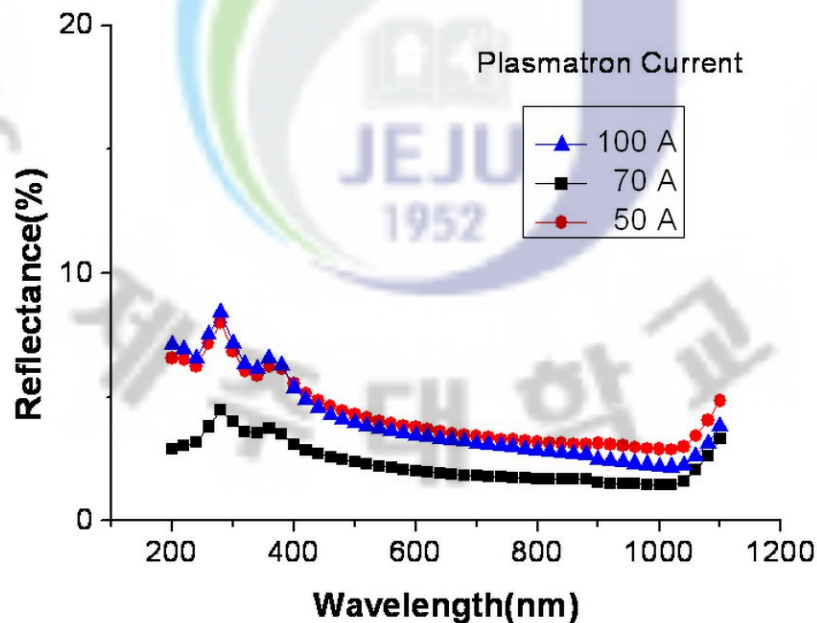


Fig. 94 Reflectance profile according to the plasmatron current: (t: 2min, P: 5 Torr, Ar: 3000 sccm, CF_4 : 90 sccm, O_2 : 500 sccm).

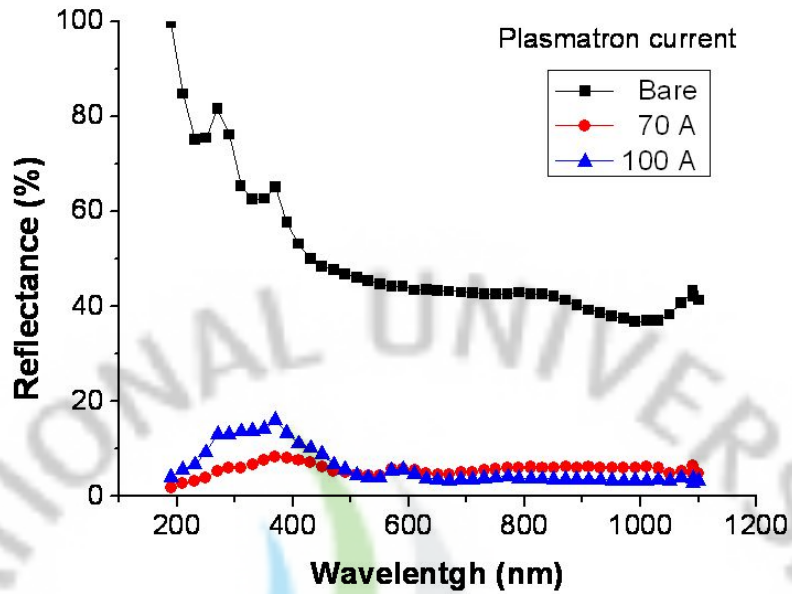


Fig. 95 Reflectance of the textured silicon surfaces according to the DC arc plasmatron current. (t: 30 sec., P: 760 Torr, Ar: 3000 sccm, SF₆: 100 sccm, O₂:500sccm).

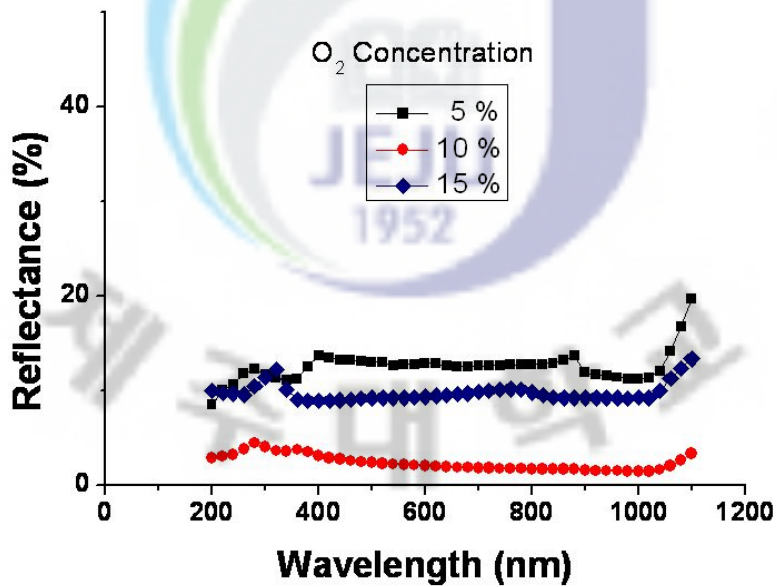


Fig. 96 Reflectance of the textured silicon surfaces according to the O₂ concentration (t: 30 sec., P: 760 Torr, Ar: 3000 sccm, SF₆: 100 sccm, Current: 100 A).

2.2 Discussion

An arc plasma source with a low anode erosion rate ($\sim 10^{-10}$ g/C) was applied to the etching of single-crystalline silicon wafers by using an activated plasma mixture of SF₆, CF₄ and O₂. Due to silicon etching investigations, we found the experimental conditions at which a rich surface morphology appears.

A texturing process was performed on a crystalline silicon (c-Si) wafer to increase the efficiency of a solar cell. A pyramid shape was etched on the wafer's surface by using a high durability DC arc plasma source at atmospheric pressure and low pressure. To survey the characteristics of the pyramid formation process, we performed plasma-texturing experiments with various working times. It is possible to find an optimal processing condition.

CF₄ and SF₆ were used as the reactive etching gases at flow rates < 100 sccm, with O₂ as the supporting gas in the range of the 5 – 15%. To survey the characteristics of the pyramid formation process, plasma texturing experiments were performed by varying the working time. The optimal operating conditions of the gas flow (Ar, O₂, CF₄, SF₆), plasmatron current and processing time were determined.

The pyramid angle was approximately 50° to 60° when a single-crystalline silicon surface was textured in a vacuum whereas it was approximately 75° to 90° when textured at atmospheric pressure. The pyramid angle is related to the reflectance. The reflectance decreases with decreasing pyramid angle. The reflectance of the bare silicon ranged from 40% to the 60% but that of the textured silicon was approximately 5% to 20%. This reflectance is quite low, approximately half that reported by other studies using wet and Reactive ion etching (RIE) texturing. These results confirm that this novel arc plasma source can be used to texture a Si surface for applications to photo-voltaic devices.

VII. Conclusions

Use of DC arc plasmatron in welding, soldering, and cutting of metals is well known. Among them, arc plasmatrons with cold thermo-chemical cathodes made of hafnium or zirconium and cold nozzle anodes (usually made of copper) seem to be the most suitable and well-recognized devices. A novel arc plasma source, which has a very low anode erosion rate, a nearly spectrally clean plasma flow, and a life time of $10^3 - 10^4$ hours, is proposed.

We modified a DC arc plasmatron to A-type for applying the plasma processing as etching and texturing. The A-plasmatron has a low erosion rate of electrodes ensuring the purity of the generated plasma necessary for technologic applications. To reduce the recombination rate of the activated gas particles inside a plasmatron and let them preserve their activated state outside, the whole device was installed outside of the vacuum chamber for vacuum processing. The experiment was provided on the mono-crystalline silicon wafer. The etching was carried out with plasma consisting of SF_6 (50 sccm) as a reactive etching gas with O_2 (300 sccm) as a supporting gas and Argon (2000 sccm) as a cathode protecting gas.

An inert gas, argon, is supplied in a channel to protect the cathode. High-voltage, high-frequency AC is initially applied across the cathode and the anode to break the inter-electrode gap, and then a continuous DC voltage maintains the ignited arc. The technologic channel supplies the reactive gas to the argon-arc region, where it interacts with the plasma and activates. The plasma then flows through the exit cap orifice and forms a jet.

A texturing process was performed on a crystalline silicon (c-Si) wafer to increase the efficiency of a solar cell. A pyramid shape was etched on the wafer's surface by using a high durability DC arc plasma source at atmospheric pressure and low pressure. To survey the characteristics of the pyramid formation process, we performed plasma-texturing experiments with various working times. It is

possible to find an optimal processing condition.

CF₄ and SF₆ were used as the reactive etching gases at flow rates < 100 sccm, with O₂ as the supporting gas in the range of the 5 – 15%. To survey the characteristics of the pyramid formation process, plasma texturing experiments were performed by varying the working time. The optimal operating conditions of the gas flow (Ar, O₂, CF₄, SF₆), plasmatron current and processing time were determined.

The pyramid angle was approximately 50° to 60° when a single-crystalline silicon surface was textured in a vacuum whereas it was approximately 75° to 90° when textured at atmospheric pressure. The pyramid angle is related to the reflectance. The reflectance decreases with decreasing pyramid angle. The reflectance of the bare silicon ranged from 40% to the 60% but that of the textured silicon was approximately 5% to 20%. This reflectance is quite low, approximately half that reported by other studies using wet and Reactive ion etching (RIE) texturing. These results confirm that this novel arc plasma source can be used to texture a Si surface for applications to photo-voltaic devices.

A DC arc plasmatron have many advantages of high chemical activity, spectrally clean plasma and large range about the pressure. However, it has a disadvantage that is difficult to apply a effectively large area. It is possible to apply the 20 mm diameter. To compensate the defect of the DC arc plasmatron, we suggested a DC-RF hybrid plasma system. This plasma system consists of 3-turn RF induction coil, DC arc plasmatron which is mounted on an RF system and quartz tube of 100 mm outside diameter. There are three gas injection modes to control a plasma flow. The argon gas is injected through the nozzle of the DC arc plasmatron. The argon gas is discharged to produce a DC arc plasmatron and protect a cathode. The swirl gas is injected to add centrifugal force.

we investigated the plasma characteristics with a Langmuir, IR camera and OES. In this results, a DC-RF hybrid plasma has a high temperature and chemical activity more than RF plasma. We performed a etching and cleaning process with a DC-RF hybrid plasma and we obtained a result of 10 μm/min etching rate.

REFERENCE

- [1] Claire Tendero, Christelle Tixier, Pascal Tristant, Jean Desmaison, Philippe Leprince, *Spectrochimica Acta, Part B* 61, 2, (2006)
- [2] A. L. Suris, "Plasma-Chemical Processes and Apparatus", Moscow: KHIMIYA, 304 (1989).
- [3] Physics, Technology and Applications of Low-Temperature Plasmas (Proceedings of the IVth All-Union Conference On Physics and Generators of Low-Temperature Plasmas).- Alma-Ata: Publ. by KAZAKH Polytechnic Institute, 1970.
- [4] J. E. Anderson. Arc Torch Chemical Reactors. US Patent No. 3051639, 204 Class, 28. 08. 62.
- [5] Yu. P. Raizer. Physics of Gas Discharges: a Study Guide, Moscow: NAUKA, 1987.
- [6] D. G. Bykhovsky, A. Ya. Medvedev, "A Device for Plasma Processing of Metals", Soviet Inventor's Certificate No. 287214, B23K 10/00 Class, 15. 11. 1968.
- [7] Air Plasma Flow Systems developed by Machine & Vision Ltd. Company of Matsushita Electric Works Ltd. Corporation under the brand name of NAIS/Aiplasma: www.aiplasma.com.
- [8] A. I. Apunevich, E. I. Titarenko, "Electric Arc Plasma Torch", RF Patent RU2112635 C1, class B23K 10/01, 1997; JSC MULTIPLAZ booklets; web site: www.multiplaz.ru.
- [9] A. V. Brichkin, I. M. Efremov, L. A. Brichkin, "Electric Arc Torch". Soviet Inventor's Certificate No. 224716, H05H 1/40 Class, 12.07.66.
- [10] A. S. Koroteev, V. M. Mironov, Yu. S. Svirchuk, PLASMATRON: Designs, Characteristics, Calculations, MASHINOSTROENIE, Moscow, 1993.
- [11] Claire Tendero, Christelle Tixier, Pascal Tristant, Jean Desmaison and Philippe

- Leprince, *Spectrochimica Acta Part B*, **61**, 2 (2006).
- [12] Claire Tendero, Christelle Tixier, Pascal Tristant, Jean Desmaison and Philippe Leprince, *Spectrochimica Acta Part B*, **61**, 2 (2006).
- [13] M. Moreno, D. Daineka, P. Rocai Cabarrocas, *Solar Energy Materials & Solar Cells*, **94**, 733 (2010).
- [14] D. Iencinella, E. Centruioni, R. Rizzoli, F. Zignani, *Solar Energy Materials & Solar Cell*, **87**, 725 (2005).
- [15] S. W. Park and J. Kim, *J. Korean Phys. Soc.* **43**, 423 (2003).
- [16] Jeehwan Kim, Daniel Inns, Keith Fogel, Devendra K. Sadana, *Solar Energy Materials & Solar Cells*, in press (2010).
- [17] D.S. Ruby, S.H. Zaidi, S. Narayanan, B.M. Damiani, A. Rohatgi, *Solar Energy materials & Solar Cell*, **74**, 133 (2002).
- [18] P. Fauchais, Plasmas thermiques: production et applications. Techniques de l'Ingenieur, Traite' Ge'nie e'lectrique. D2 820.
- [19] <http://www.praxairthermalspray.com>.
- [20] <http://www.sulzermetco.com/eprise/SulzerMetco/Sites/News/OTS/ots07e.htm>
- [21] P. Fauchais, A. Vardelle, Les applications innovantes des plasmasthermiques dans l'industrie, Les guides de l'innovation NOVELECT/EDF R&D. NOV001E2003 (2003).
- [22] B. Paya, Ph. Fache, Le plasma inductif de forte puissance. Cahiers de l'Ingenierie, Mars (1997).
- [23] J. Salge, Plasma-assisted deposition at atmospheric pressure, *Surf. Coat. Technol.* **80** (1996).
- [24] J. L. Delacroix, A. Bers, Physique des plasmas. Paris: Inter Editions/CNRS Editions (1993).
- [25] I. G. Kesaev, Cathode Processes of the Electric Arc, NAUKA, Moscow (1968).
- [26] V. A. Shadov, thesis of candidate dissertation, Moscow Aviation Institute (1967).
- [27] V. A. Riaby, V. Yu. Plaksin, J. H. Kim, Y. S. Mok, H. J. Lee, C. K. Choi, *J. Korean Phys. Soc.* **48**, 1696 (2006).

- [28] H. J. Lee, V. Yu. Plaksin, V. A. Riaby, *Thin Solid Films*, 515, 5197 (2007).
- [29] J.D. Chase, *J. Appl. Phys.* 40, 318 (1968).
- [30] M.I. Boulos, *IEEE Trans. Plasma Sci.* 4, 28 (1976).
- [31] P. Proulx, J. Mostachimi, M.I. Boulos, *Int. J. Heat Mass Transfer* 28, 1327 (1985).
- [32] M. El-Hage, J. Mostahimi, M.I. Boulos, *J. Appl. Phys.* 65, 4178 (1989).
- [33] T. Yoshida, T. Tani, H. Nishimura, K. Akashi, *J. Appl. Phys.* 54, 640 (1983).
- [34] J.W. Mckelliget, N. El-kaddah, *Metall. Trans. B* 21, 589 (1990).
- [35] S.W. Nam, H. Nishiyama, S. Kamiyama, *JSME Int. J.*, B 39, 134 (1996).
- [36] K. Kawajiri, T. Sato, H. Nishiyama, *Surf. Coat. Technol.* 171, 134 (2003).
- [37] K. Kawajiri, K. Ramachandran, H. Nishiyama, *Int. J. Heat Mass Transfer* 48, 183 (2005).
- [38] J.L. Genna, R.M. Barnes, Ch.D. Allemand, *Anal. Chem.* 49, 1450 (1997).
- [39] J.D. Chase, *J. Appl. Phys.* 42, 4870 (1971).
- [40] L. Christov, M. Christova, V. Gagov, I. Koleva, A. Shivarova, *J. Tech. Phys.* (Warsaw), 40, 411 (1999).
- [41] W. Lochte-Holtgreven (Ed.), *Plasma Diagnostics*, North Holland Publishing Company (1968).
- [42] Claire Tendero, Christelle Tixier, Pascal Tristant, Jean Desmaison and Philippe Leprince, *Spectrochimica Acta Part B* 61, 2 (2006).
- [43] M. Moreno, D. Daineka and P. Rocai Cabarrocas, *Solar Energy Materials & Solar Cells* 94, 733 (2010).
- [44] D. Iencinella, E. Centruioni, R. Rizzoli and F. Zignani, *Solar Energy Materials & Solar Cell* 87, 725 (2005).
- [45] S. W. Park and J. Kim, *J. Korean Phys. Soc.* 43, 423 (2003).
- [46] Jeehwan Kim, Daniel Inns, Keith Fogel and Devendra K. Sadana, *Solar Energy Materials & Solar Cells*, in press (2010).
- [47] D. S. Ruby, S. H. Zaidi, S. Narayanan, B. M. Damiani and A. Rohatgi, *Solar Energy Materials & Solar Cell* 74, 133 (2002).

- [48] C. H. Yi, Y. H. Lee and G. Y. Yeom, *Surface and Coating Technology* **171**, 237 (2003).
- [49] W. A. Nositschka, O. Voigt, P. Manshanden and H. Kurtz, *Solar Energy Materials & Solar Cells* **43**, 227 (2003).
- [50] J. H. Kim, Y. S. Mok, C. K. Choi, V. Yu. Plaksin, V. A. Riaby and H. J. Lee, *27th International Symposium on Dry Process* (The Institute of Electrical Engineers of Japan, 2005), 359.
- [51] V. A. Riaby, V. Yu. Plaksin, J. H. Kim, Y. S. Mok, H. J. Lee and C. K. Choi, *J. Korean Phys. Soc.* **48**, 1696 (2006).
- [52] I. I. Aksenov, V. V. Vasilyev, B. Druz, A. A. Luchaninov, A. O. Omarov and V. E. Strel'nitskij, *Surface & Coatings Technology* **201**, 6084 (2007).
- [53] V. Yu. Plaksin, S. B. Joa, H. J. Lee and C. K. Choi, *J. Korean Phys. Soc.* **50**, 723 (2007).

국문초록(Abstract)

플라즈마는 낮은 압력에서 디스플레이 및 반도체 공정에서 건식 식각, 박막 증착, 표면 처리 이용되고 있다. 그러나 낮은 압력에서의 공정은 진공 장비 및 구성요소를 사용해야 하는 단점이 있어 경제적이지 못하다. 습식공정은 많은 화학약품을 사용해야하는 단점 있다. 만약에 안정된 대기압 플라즈마를 사용하게 되면 공정비용의 절감뿐만 아니라 생산성 향상에 도움이 될 것이다.

높은 온도를 갖는 음극과 낮은 온도를 갖는 양극으로 구성된 새로운 직류 아크 플라즈마트론을 개발하였고, 직류 아크플라즈마트론의 전압-전류 특성을 조사하였다. 전류-전압 특성은 플라즈마트론의 안정적 동작을 확인하는데 중요한 변수다. 양극의 전 영역에 분포되어있는 양극점은 직류 아크 플라즈마트론을 안정적으로 동작하게 하고 플라즈마 공정에 적용 가능하게 해준다. 그리고 측정된 직류 아크 플라즈마트론의 양극 침식율은 $\gg 3.6 \times 10^{-10}$ g/C 으로, 텅스텐으로 만들어진 열전자 방출 음극 플라즈마토치의 침식율인 $\sim 10^{-9}$ g/C에 비해 매우 낮다. 양극 침식율은 플라즈마 트론의 수명과 관련이 있고, 약 10^3 h의 수명을 보임을 알 수 있다. 그리고 침식되는 양극의 양이 줄어들어 보다 더 깨끗한 플라즈마를 얻을 수 있는 장점이 있는 것을 확인하였다. 이런 직류 아크 플라즈마트론 특성은 식각, 증착, 화학적 반응 등의 기술적인 응용에 적용하기에 흥미로운 플라즈마 소스임을 보여준다.

직류 아크 플라즈마트론을 플라즈마 공정에 적용하기 위해 T-형 플라즈마트론을 A-형으로 수정 개발하였다. A-형 직류 아크 플라즈마트론을 사용하여 식각 실험을 수행하였고, 사용된 식각 가스는 CF_4 , SF_6 를 사용하였고, 저진공 및 대기압에서 식각공정을 하였다. 진공실험에서 활성화된 가스 입자의 재결합을 줄이기 위해 플라즈마트론을 진공 챔버와 결합을 하여 구성하였다. 식각 실험에 사용한 실리콘 웨이퍼는 단결정 실리콘으로 구성된 기판이다. 플라즈마 가스는 식각 가스로 $SF_6(50 \text{ sccm})$, 식각 가스를 보조하는 가스로 $O_2(300 \text{ sccm})$, 플라즈

마 방전 및 음극 보고 가스로 아르곤(2000 ~ 3000 sccm)을 사용하였다. 진공(3-5 torr)에서 증착 실험한 결과, 최고 증착률은 60 $\mu\text{m}/\text{min}$ 로 매우 높은 증착률을 보였다. 대기압에서 실험을 하기 위해, 진공 챔버 및 펌프 등의 요소들을 제거 하여 식각 실험을 하였다. 사용된 식각 가스는 CF_4 로, 산소와 아르곤은 진공에서와 동일한 조건으로 사용하였다. 대기압 식각 결과, 최고 증착률은 300 $\mu\text{m}/\text{min}$ 이상으로 진공에서의 결과보다 약 5배 정도 높은 결과를 얻었으며, 그 이유는 플라즈마 밀도가 진공에서 보다 대기압에서 높기 때문일 것이다.

식각 공정과 같은 시스템에서 직류 아크 플라즈마 트론을 이용하여 Texturing 공정을 수행하였다. Texturing 공정은 태양전지에서 광의 반사율을 줄여 효율을 높이기 위해 표면을 처리하는 기술이다. Texturing 공정도 진공 및 대기압에서 수행을 하였고, 식각 가스 또한 식각 공정과 같은 CF_4 , SF_6 를 사용하였다. 이 공정에서 변수를 각 가스의 조성 및 유량, 공정 시간, 플라즈마 트론의 작동 전류 등을 다르게 하여, 최적의 공정조건을 찾았다. Texturing된 표면의 피라미드 각도는 대기압 공정에서는 약 75° - 90°, 진공 공정에서는 50° - 60°이다. 이런 차이는 진공과 대기압에서의 플라즈마 평균자유비경의 차이에서 기인한 것으로 여겨진다. 반사율은 피라미드 각도가 작아질수록 낮아졌다. Texturing 하지 않은 실리콘은 반사율은 각 파장 별 약 40%에서 60%사이 이다. 그러나 Texturing된 실리콘 표면의 반사율은 최저 5%에서 최대 20%까지 줄어들었다. 이 결과는 다른 습식 공정 및 RIE 공정에 비해서도 매우 낮은 반사율이다.

직류 아크 플라즈마 트론의 이런 매우 많은 장점에도 불구하고, 직류 아크 플라즈마 트론은 적용 면적이 작아 산업에 적용하기가 어렵다. 이를 극복하여 적용 면적을 넓히기 위해 직류-고주파 복합 플라즈마 소스를 제안하였고, 설계·제작하였다. 직류-고주파 복합 플라즈마 시스템은 직류 아크 플라즈마 트론, 고주파 파트, 가스 제어 시스템, 진공 시스템 등으로 구성하였다. 직류-고주파 복합 플라즈마 시스템의 특성을 알아보기 위하여 랭뮤어 프로브 진단, OES 분광분석, 적외선 카메라를 이용하여 석영유리관으로 제작된 반응챔버 온도 등을 측정하였다. 고주파 임피던스 매칭을 위해 PSIM 소프트웨어를 이용하여 임피던스 코일 내의 전류를 계산하여 매칭할 때, 최적의 캐패시터 값을 얻었다. 랭뮤어 프로브 진단 결과, 고주파 플라즈마와 직류-고주파 복합 플라즈마를 비교 분석하

였다. 직류-고주파 복합 플라즈마의 경우 수평으로 균일한 플라즈마 밀도 (1×10^{10} #/cm³), 온도 (1-4 eV)를 보였다. 제작된 직류-아크 플라즈마를 이용하여 식각 실험을 하였다. 그 결과, 전 영역에 대하여 10 μ m/min의 균일한 식각률을 보였고, 반응 챔버 넓이만큼의 균일한 플라즈마를 얻었다.



CURRICULUM VITA

◎ Personal Information

- Name : Ji Hun Kim
- Date of Birth : April 14, 1975
- Place of Birth : Jeju, Republic of Korea

◎ Education

- B. S. in Department of Nuclear & Energy Engineering(1994-2001) Jeju National University, Jeju, Korea

- M. S. in Department of Nuclear & Energy Engineering(2001-2003) Jeju National University, Jeju, Korea

"Study on the Characteristics and Fabrication of Solid-State Dye Laser for LIF Plasma Diagnostics"

Supervisor : Prof. Heon Ju Lee

- Ph. D. in Department of Nuclear & Energy Engineering(2003-2011) Jeju National University, Jeju, Korea

"Development of the DC-RF Hybrid Plasma Source and the Application to the Etching and Texturing of the Silicon Surface"

Supervisor : Prof. Heon Ju Lee

◎ Project Research Activities

- "Development of nuclear infrastructure and key element technology" 2010. 09 - , Korea Research Foundation

- "Development of the Thomson Scattering Diagnostic System" 2009. 09 - , Korea Research Foundation
- "The Development of Multi-channel Neutral Particle Analyzer Applied" 2009. 09 - , Korea Research Foundation
- "The Protective Film Development of GPS Glass Surface" 2010. 03 - 10, HBI Group Company
- "Development Diesel Particulate Filter Technology in Diesel engine exhaust gas for catalyst simultaneously removal using low temperature plasma and denitrification occlusion catalyst simultaneously removal" 2006. 08 - 2009. 07, Ministry of Knowledge Economy, Korea
- "Development of emission reduction technology from diesel engine by plasmatron" 2004. 04 - 2007. 03, Ministry of Knowledge Economy, Korea
- "Development of Laser Induced Fluorescence Spectroscopy" 2005. 04 - 2007. 03, Korea Research Foundation
- "Study on the Plasma Spectroscopy using a Solid-State Dye Laser" 2003. 01 - 2004. 11, Korea Basic Science Institute
- "Characteristics Analysis of vapor of Low Dielectric Film" 2002. 07 - 2003. 05, Korea Basic Science Institute

◎ **Publication Lists**

1. Valentin A. Riaby, Vadim Yu. Plaksin, Ji Hun Kim, Young Sun Mok and Heon-Ju Lee, "Application of a High-Durability DC Arc Plasmatron to Plasma-Chemical Processing of Silicon Substrates", Journal of the Korean Physical Society, Vol. 48, No. 6, 1696, 2006 (SCI)
2. Ji Hun Kim and Heon-Ju Lee, "Plasma Diagnostics of Hydrogen Plasma with Laser Induced Fluorescence Measurement and Collisional Radiative Model", Journal of the Korean Physical Society, Vol. 49, S184, 2006 (SCI)
3. Ji Hun Kim, Chan-Joo Yim and Heon-Ju Lee, "Lifetime Improvement of a LDS698 Solid Dye Laser by Doping with PETA", Journal of the Korean Physical Society, Vol. 51, No. 6, 1909, 2007 (SCI)
4. Vadim Yu. Plaksin, Heon-Ju Lee, Valentin A. Riaby, Young Sun Mok, Sang Hoon Lim and Ji Hun Kim, "Reduction of NO_x in diesel engine emissions by using a plasmatron fuel reformer", Korean J. Chem. Eng, Vol. 25, No.1 84, 2008 (SCIE)
5. Oleksiy V. Penkov, Heon-Ju Lee, Vadim Y. Plaksin, Rakib Mansur, Ji Hun Kim, "Deposition of the ZnO transparent electrodes at atmospheric pressure using a DC Arc Plasmatron", Thin Solid Films, Vol. 518, 6160, 2010 (SCI)
6. Min Kook Ko, Vadim Yu. Plaksin, Ji Hun Kim, Rakib M. Mansur, Eun Young Yun, Young Son Mok and Heon Ju Lee, "Self-sustained reformation of diesel fuel using a SiC block with penetrating walls", INTERNATIONAL JOURNAL OF ENERGY RESEARCH, Vol. 34, 84, 2010 (SCIE)

7. Ji-Hun Kim, Se-Min Chun and Heon-Ju Lee, "Study on the Plasma Texturing for Increasing the Conversion Efficiency of a Solar Cell with a DC Arc Plasmatron", Journal of the Korean Physical Society, Vol. 57, No. 5, 1218, 2010 (SCI)



감사의 글(Acknowledgement)

지난 대학원 생활을 지내고 보니 참으로 많은 것을 배우고 느낀, 뜻 깊은 시간이었습니다. 먼저 학부 때부터 학위논문을 무사히 마치도록 많은 채찍과 격려를 해주신 이현주 교수님께 감사를 드립니다. 교수님께서 연구자의 기본 자세를 저에게 일깨워 주셨습니다. 교수님 가르침 잊지 않고 앞으로도 정진하겠습니다. 또한 학위논문 심사위원이신 최치규 교수님, 이윤준 교수님, 한국연구재단 국책연구본부장이신 단국대학교 노승정 교수님, 국가핵융합연구소 플라즈마융합연구센터장이신 유석재 박사님께 감사드립니다. 저에게 많은 조언과 격려를 하여 주셔서 논문을 마무리 할 수 있었습니다. 그리고 학부 때부터 많은 가르침을 주신 에너지공학과 박재우 교수님, 천원기 교수님, 김신 교수님, 정범진 교수님, 김남진 교수님께 감사드립니다.

제가 졸업하기까지는 주위의 많은 분들의 도움이 있었으며, 그분들께 이 글을 통하여 감사를 드립니다. 어렵고 힘들 때 힘이 되어준 “핵융합 및 플라즈마 응용연구실” 후배 좌상범, 임찬주, 고민국, 천세민, 강인제, 강은정, 양종근, 박선민과 물리학과 김창영에게 감사의 말을 전합니다. 못난 선배 밑에서 고생도 많이 하고, 저에게 많은 도움을 줬습니다. 또한 에너지공학과 대학원 현준호 선배, 오승진, 김영민, 오원종을 비롯한 여러 대학원 후배들 덕분에 대학원 생활을 마무리할 수 있게 되었습니다. 또한 저에게 행정적 지원을 아끼지 않은 학과사무실 박형훈, 김우용 조교선생님께도 감사의 말을 전합니다.

본 학위논문을 완성할 수 있도록 저를 이공계 국가연구장학생으로 선발해주신 한국장학재단 관계자 여러분께도 감사를 드립니다.

그리고 누구보다 기뻐할 부모님, 장모님 감사합니다. 제가 여기까지 올 수 있었던 원동력이었습니다. 그리고 큰형님 내외, 작은 형님 내외, 큰누님 내외, 작은 누님 내외, 처제 내외, 처남 등 가족들에게 이 기쁨과 보람을 함께 보냅니다. 아빠라고 많이 놀아주지도 못하고 시간을 많이 보내주지 못했는데도, 아빠를 찾고, 많이 좋아하는 두 딸 령은, 태연!! “아빠가 정말 사랑해!!”. 대학원생인 남편을 만나 힘든 시간 함께 버텨준 나의 아내 고은해에게 사랑한다 말을 전하며, 이 논문은 아내의 눈물이자 기쁨입니다. 이 논문은 제가 이 세상에서 가장 사랑하는 아내에게 바칩니다.